HYDRODYNAMIC PERFORMANCE AND SEAKEEPING ANALYSIS OF A CATAMARAN IN TRANSFORMING NEAR-SHORE HEAD AND FOLLOWING SEAS

by

Kayhan Ulgen

A Dissertation Submitted to the Faculty of

The College of Computer Science and Engineering

in Partial Fulfillment of the Requirements for the Degree of

Doctor of Philosophy

Florida Atlantic University

Boca Raton, FL

May 2022

HYDRODYNAMIC PERFORMANCE AND SEA-KEEPING ANALYSIS OF A CATAMARAN IN TRANSFORMING NEAR-SHORE HEAD AND FOLLOWING SEAS

by

Kayhan Ulgen

This dissertation was prepared under the direction of the candidate's dissertation advisor, Dr. Manhar R. Dhanak, Department of Ocean and Mechanical Engineering, and has been approved by the members of his supervisory committee. It was submitted to the faculty of the College of Computer Science and Engineering and was accepted in partial fulfillment of the requirements for the degree of Doctor of Philosophy.

SUPERVISORY COMMITTEE:

Manhar R. Dhanak, Ph.D.
Dissertation Advisor

Tsung-Chow Su, Eng.Sc.D.

Pierre Philippe Beaujean, Ph.D.

Oscar M. Curet, Ph.D.

Pierre Philippe Beaujean, Ph.D.
Chair, Department of Ocean and Mechanical Engineering

Stella Batalama, Ph.D.
Dean, The College of Computer Science and Engineering

Robert W. Stackman Jr., Ph.D.
Dean, Graduate College

April 28, 2022

Date

ACKNOWLEDGEMENTS

I would like to thank Dr. Betsy Seiffert for allowing me to continue my career in the USA. I would like to thank Dr. Tsung-Chow Su, Dr. Philippe-Pierre Beaujean and Dr. Oscar Curet for their support, suggestions and recommendations in this study. I really would like to thank Rhian Resnick, Skyler Paulus and James Mauser for their technical support. I want to thank Barbara Steinberg and Anastasia Calnick for their support and guidance.

Above all, I would like to thank Dr. Manhar Dhanak, for being a great advisor allowing me to become a better researcher, developer and instructor. I have been his student for two years, and he always pushed me to produce a quality work. I honestly appreciate all the help he provided during my PhD experience. Moving forward, I plan to learn from his experiences to make a great contribution to the field of ocean engineering.

ABSTRACT

Author:	Kayhan Ulgen
Title:	Hydrodynamic performance and seakeeping analysis of a catamaran in transforming near-shore Head and Following Seas
Institution:	Florida Atlantic University
Dissertation Advisor:	Dr. Manhar R. Dhanak
Degree:	Doctor of Philosophy
Year:	2022

A computational investigation of the hydrodynamic and seakeeping performance of a catamaran in calm, and in the presence of transforming head and following seas in waters of constant and varying depths is described. Parametric studies were conducted for a selected WAM-V 16 catamaran geometry using OpenFOAM® to uncover the physical phenomena. In the process a methodology has been developed for simulating the interactions between the vehicle and the shallow water environment akin to that in the coastal environment. The multiphase flow around the catamaran, including the six degrees-of-freedom motion of the vehicle, was modeled using a Volume of Fluid (VoF) method and solved using a dynamic mesh. The numerical approach was validated through computing benchmark cases and comparing the results with previous work. It is found that in a calm shallow water environment the total resistance, dynamic trim and sinkage of a catamaran in motion can be significantly impacted by the local water depth. The variations of the impact with depth and length-based Froude numbers are characterized. The impact varies as the vehicle moves from shallow waters to deep water or vice versa. In the presence of head and

following small-amplitude seas, interesting interactions between incident waves and those generated by the vehicle are observed and are characterized for their variation with Froude number and water depth.

To my parents, Burhan Ulgen and Zerrin Ulgen, my best friend Carlos Arturo Murgueytio, for their love and support.

HYDRODYNAMIC PERFORMANCE AND SEAKEEPING ANALYSIS OF A CATAMARAN IN TRANSFORMING NEAR-SHORE HEAD AND FOLLOWING SEAS

LIST OF TABLES

LIST OF FIGURES

CHAPTER 1
INTRODUCTION

1.1 OVERVIEW

Ocean waves are formed by complex actions of resonance and shearing effects, in which the waves travel in various directions with different lengths, amplitudes, and periods. When the ocean waves form, they can travel vast distances, spreading in different directions by reducing their amplitude but preserving the wavelength and frequency. As the ocean waves approach the shoreline, the wave amplitude and wavelength begin altering due to the refraction and shoaling before the breaking phenomena. When the waves break, they travel through the surf zone. In the surf zone, complex transformation and attenuation processes occur, including the cross and long-shore current generation and the mean water level change. When a ship operates through the shoreline, the hull begins interacting with the waves that can lead to unknown motions. The physical phenomenon of wave transformation through shallow water zone and the effect of wave-hull interaction on hydrodynamic performance is a complicated problem. This study aims to distinguish a catamaran's hydrodynamic and seakeeping performance in a limited water depth environment through parametric numerical computations to uncover this physical phenomena.

The aim of this study is to build a methodology for simulating an ocean wave environment and interactions with the catamaran by using the method of computational fluid dynamics (CFD). CFD is one such branch, that is integrating the fundamentals of fluid dynamics with mathematics and computer science. The physical characteristics of fluid motion are described by mathematical equations, particularly in partial

differential form, that are called governing equations. To solve the problems of fluid motion numerically, high-level computer programming languages are increasingly used to transform partial differential equations to algebraic systems. Numerical simulations and analyses are widely performed in many engineering applications that include aerospace engineering(airplanes, jets, rockets, nozzles), ocean engineering (ships, offshore structures, mangroves, etc.), automotive engineering (efficient design, air intake in engines, etc.), chemical engineering (pumps, pipes, etc.), power engineering (wind farms, performance prediction, etc.), biomedical engineering (blood flow in hearts and vanes, breathing, sneezing, etc.) [3].

In ship hydrodynamics, the aptitudes of CFD is beneficial in design and optimization procedure. Model testing is an experimental method that provides quantitative and qualitative information to determine a full-scale prototype's hydrodynamic performance. Model testing is based on Froude's law of similarity that a small scale of the prototype is used to determine the ship's power requirements, and the model scale results are extrapolated to a full-scale prototype. The model tests should be performed at a large enough scale to minimize viscosity scale effects. However, the model scale cannot be too large due to the towing tank's restricting size [4]. The dilemma in model testing can be overcome by using the method of CFD that has extensive capabilities including, but not limited to, dynamic mesh motion, interface tracking /capturing, rigid body motion, six degrees of freedom motion, cavitation modeling, adaptive grid refinement, overset (Chimera) grids, turbulence modeling, wave modeling and parallel computing [5]. The ship's resistance, ship wave pattern and the nominal wake on the propeller plane are the main objectives of the design process, which provide practical information for the efficient ship design. A vessel's motion through water requires enough power to overcome the resistance, that is, the total force acting against the motion. The resistance of the full-scale ship cannot be measured. Therefore, the information regarding the ship's resistance can be obtained

via either model tests or CFD simulations.

1.2 PROBLEM STATEMENT

The performance of a ship differs when it operates in limited depth waters, where the pressure distribution along the water column has a remarkable effect on the rigid body motion. In inland waters, the shallow water effect can affect the performance based on two distinct conditions: shallow water channel, in which only the limited water depth affects the performance, and restricted channel, in which limited depth and limited width of the channel have an extraordinary impact on the operational conditions.

Fundamentally, the effects of limited water depth on the hydrodynamic performance of a ship can be categorized into three interrelated aspects: the change in dynamic position (trim and sinkage), the elevation in total resistance (increased wetted surface area), and reduced maneuvering capabilities.

The limited depth has a critical value for conventional ships, that assists in safety of operation in inland waters by avoiding grounding and squatting. Furthermore, the rise in resistance leads to extensive power requirements, that affects the ship resistance and propulsion in shallow waters. Therefore, an accurate prediction of hydrodynamic performance and motion characteristics in limited depth waters is significant.

1.3 OBJECTIVES

In this section, the objectives of the current study are presented. The first objective is based upon the application of the numerical approach on a benchmark case by using OpenFOAM®. Validation and verification study of the current method is crucial for modeling the dynamic motion of ships in shallow waters.

The second objective is to determine the hydrodynamic performance of a catamaran of interest. In this case, the total resistance, trim, sinkage, and wave elevation

data are compared, and the phenomena occurred explained physically.

The third objective is to develop an approach to model the dynamic motion of the vessel through transforming near-shore head and following waves. In this case, the wave-ship interactions and the change in seakeeping performance due to different water depths are explained in physical manner.

1.4 APPROACH

The following approaches are considered in this study:

1. To validate our methodology, a benchmark case for calm-water resistance and seakeeping performance under various wave conditions are selected. Korean Container Ship (KCS) hull is a widely used as a benchmark case for resistance and seakeeping simulations. The resistance, trim and sinkage values are compared with the experimental data [6].

2. To ensure the accuracy of the results, grid dependency studies are carried for calm-water resistance simulations of KCS hull geometry.

3. After the validations are completed successfully, the catamaran model of interest is selected, and the geometry is simplified to generate a computational flow domain around the rigid model for numerical computations.

4. A similar grid dependency study is applied on the catamaran of interest in deep water conditions. To determine the effect of limited water depth, numerical simulations are conducted at four different depths and nine advance speeds. The results are analyzed in terms of Froude number (Fr_H) and corresponding water depths.

5. To determine the seakeeping performance of the catamaran in transforming head and following seas, a computational domain is constructed in which the

water depth decreases linearly as the waves approach to the shoreline.

6. To model surge, heave and pitch motions of the catamaran, an overset (Chimera) mesh generated around the flow domain, avoiding excessive computational time. An open-source wave generation toolbox waves2Foam® and OpenFOAM® is compiled to generate stream function waves, during the motion of the hull.

1.5 SIGNIFICANCE

Ships are designed to operate in transforming waters; whenever it puts forth or approaches the port, it will encounter permeable wall effects due to the change in water depth. The water depth has a significant impact on viscous and wave resistance, trim, sinkage and hull efficiency. Previous researches showed that the fluid velocity decreases since the distance between the hull and seabed lessens. Moreover, the buoyancy force acting on the hull decreases as the pressure affecting the bottom of the hull reduces [7, 8, 9]. Therefore, the total resistance, trim and sinkage values increase and become greater than those in deep water.

A vessel moving through the water produces transverse and divergent wave patterns [10]. These patterns vary depending on the depth Froude number (Fr_H) [11]. The surface generated waves are dominated by the bow generated waves due to interference. The bow-generated waves are the main reason for the transition from laminar to turbulent flow due to vorticity generation near the free surface [4, 7]. The nominal wake is the wake region where the velocity components are measured at the propeller plane in the absence of the propeller effecting the flow at the stern. The wake distribution directly affects the propeller selection in terms of efficiency due to the pressure reduction at the stern, which causes cavitation [12]. For these reasons, not only the performance of a ship but also the overall system is deeply affected by the limited water depth conditions.

CHAPTER 2
LITERATURE REVIEW

The first computational techniques to discretize the free-surface flow around the hull and wave-hull responses are based on the potential theory, which uses boundary element methods developed by Hess and Smith et al. (1967)[13]. In this method, the Laplace equation is solved in the fluid domain, where appropriate boundary conditions are applied. The arbitrary body is divided into infinite number quadrilateral panels, where constant source distribution is applied. The first steady free surface flows around the ships are applied by Gadd and Dawson [14, 15]. Dawson developed a radiation condition using a finite difference operator that is still widely used in potential flow applications. There are several methods developed for this non-linear problem where wave resistance were simulated [16, 17, 18, 19]. Moreover, frequency and time-domain methods, strip theory and three-dimensional panel methods, Green functions or Rankine sources are widely used methods in seakeeping applications for the prediction of wave-hull interactions and loads in waves [20, 21]. Even though potential methods are robust for wave-hull interactions, viscous effects, breaking waves, and turbulence effects are neglected that have dominance at High-Reynolds number flows [22].

In physics, the fluid motion is described by a set of partial differential equations, called Navier-Stokes equations. Navier-Stokes equations mathematically describe the governing equations of fluid flow: mass, momentum, and energy conservation. The methods of computational fluid dynamics are widely used to solve Navier-Stokes equations numerically. Computational fluid dynamics (CFD) is based on solving the governing equation of fluid motion in a set of algebraic equations using appropriate

discretization methods such as finite difference, finite element, and finite volume methods. Reynolds Averaged Navier Stokes equations are one of the approaches to solve Navier-Stokes equations for internal and external problems with or without turbulence and free-surface effects [23]. The free-surface modeling with Reynolds-Averaged Navier Stokes equations is widely used in ship resistance applications, maneuvering and seakeeping, propeller performance and cavitation modeling, wave impacts on offshore structures, and wave-hull interactions.

Previous researches in the field of computational ship hydrodynamics showed successful approaches regarding performance predictions. Tahara et al. modeled free surface flow via a single-phase level set method for unsteady viscous flows, in which the fluid properties remained uniform and the sharp air-water surface was achieved [24]. Carrica et al. generated regular and small amplitude head waves for the heaving and pitching responses of DTMB (David Taylor Model Basin) 5512 model by using a single-phase level set method [25]. Wilson et al. simulated auto-piloted ONR Tumblehome model 5613 by using Unsteady Reynolds-Averaged Navier Stokes (URANS) approach in both regular and irregular waves. The overset (Chimera) grid technique was used with six degrees of freedom motion solver that allows large amplitudes of seakeeping and maneuvering, as well as simultaneous motion of propellers and rudder [26]. Paik et al. studied wave-induced forces of S175 container ship by modeling heave and pitch motions under regular waves, and applying a blended $k-\epsilon/k-\omega$ turbulence model [27]. Banks et al. developed a numerical methodology to predict the components of total resistance by using two different turbulence models for KCS hull [28]. Carrica et al. applied dynamic overset grid approach with six-degrees of freedom motions on fully appended DTMB 5415 model for steady turn and zigzag maneuvering simulations [29]. Sadat-Hosseini et al. performed free and fixed surge motions of KVLCC2 model in short and long head waves [30]. Simonsen et al. performed heaving and pitching motions and added resistance of KCS in both calm water

and regular waves and compared with experimental results [31]. Shen et al. predicted heave and pitch motions of Wigley Hull and DTMB 5512 model in head waves by using mesh deformation techniques in OpenFOAM [32].

Moreover, Bhushan et al. performed resistance, propulsion, and seakeeping computations of Athena R/V and maneuvering simulations of fully appended DTMB 5415 model by using smooth and rough wall functions [33]. Shen et al. implemented and overset grid capability for OpenFOAM and validated steady-state viscous flow around DTMB 5512 benchmark case [34]. Tezdogan et al. performed fully non-linear URANS simulations on full-scale Kriso Container Ship (KCS) hull to estimate the effective power and fuel consumption to operate in head seas, where the Volume of Fluid (VoF) method was applied for free surface capturing/tracking, and its advantages on numerical efficiency were discussed [35]. Carrica et al. performed zigzag maneuvering simulations of fully appended KCS in swallow water by using fully-implicit dynamic overset (Chimera) grids with Direct Numerical Simulation [36]. Sadat-Hosseini et al. demonstrated six degrees of freedom motions of a damaged passenger ship SSRC including flooding and roll decay in calm water and regular beam waves for several wavelengths at zero advance speed compared with experimental data [37]. Tezdogan et al. studied the have and pitch motions of full-scale KCS in head-seas at several water depths, including shallow water effects on trim and sinkage of the hull [38]. Castiglione et al. examined the resistance and response of Delft 372 catamaran in head waves for various advance speeds and pointed a peak for heave and pitch motions at the resonant frequency at various Froude numbers [39]. The seakeeping characteristics of high speed Delft catamaran, in head and oblique waves are analyzed [40]. The wave interference effects high speed Delft catamaran in shallow water at various advance speeds are investigated [41].

CHAPTER 3

NUMERICAL APPROACH AND PROBLEM FORMULATION

3.1 GOVERNING EQUATIONS OF FLUID FLOW

The computational fluid dynamics method is based on solving partial differential equations of fluid dynamics using several numerical methods in a computational domain with appropriate physical boundary conditions. These equations are called Navier-Stokes equations, representing the mathematical description of the conservation laws of physics and can be applied to model external and internal fluid flow problems [42, 43].

Fluids are materials that do not change their physical form permanently under a large force. On the other hand, solids resist the applied force and change their shape by deforming. Solids have definite shapes, while fluids take the shape of the domain in which fill the volume. Despite the fact that gases completely fill the domain, liquids have a free surface under the influence of a gravitational field [44].

In continuum mechanics, physical properties of the fluid flow are defined at each point in space. Therefore, fluid flows can be classified as Newtonian or non-Newtonian, depending on the correlation between shear stress and the rate of shear. Although there is a linear correlation between shear stress and shear rate in Newtonian fluids, this relation is characterized by a non-linear function for non-Newtonian fluids. Besides, the flows can be described as steady or unsteady, incompressible or compressible, viscous or inviscid, laminar or turbulent, mono-phase or multiphase, among others. The reason of such classification is to simplify the problems of fluid mechanics to model and analyze the fluid flow.

3.1.1 Eulerian and Lagrangian Approaches

The fundamental principle of conservation establishes that certain physical quantities are conserved for a region in space of interest. This principle is also called conservation law, which is an axiom that can be presented mathematically.

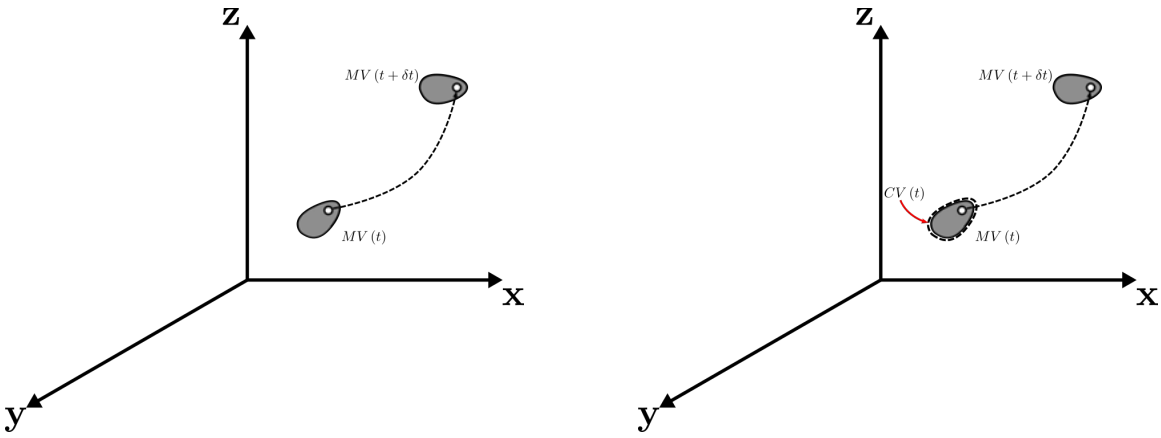

(a) Eulerian approach

(b) Lagrangian approach

Figure 3.1: Description of the fluid flow.

The conservation laws of physics related to kinematic description of fluid flow that can be expressed in terms of Eulerian or Lagrangian approaches.To describe body motion of a rigid body, three spatial coordinates of the center of gravity, three angular coordinates of the center of gravity and angular orientation of the rigid body at each time are used. If these coordinates are known as a function of time, it is straightforward to find the derivatives with respect to time and describe the velocity components and angular velocity of the center of gravity. Furthermore, the linear and angular accelerations of the rigid body can be found. This description is called Lagrangian approach, where the fluid is subdivided into small elements and the location of each element is described by time-dependent vector field. Therefore, this description becomes over-complicated to state the motion of infinite number of fluid particles [45]. To overcome this dilemma, Eulerian approach is used, that focuses on the velocity vector **U** of the fluid particle as a function of the location in space **r** and

in time t.

$$\mathbf{U} = \mathbf{U}(\mathbf{r}, t) \tag{3.1}$$

In Eulerian approach, the acceleration and displacement of the fluid particle at any location $\mathbf{r}$ and in time t can be calculated. Any physical property of the fluid flow is described by the functions of location $\mathbf{r}$ and time t. Therefore, pressure, velocity, density et al. terms are considered as the dependent variables of the fluid flow while they are described as the functions of independent variables $\mathbf{r}$ and t. In Cartesian coordinates, the location vector $\mathbf{r}$ is:

$$\mathbf{r} = x\hat{i} + y\hat{j} + z\hat{k} \tag{3.2}$$

3.1.2 Material Derivative

Eulerian derivative $\left(\frac{\partial \phi}{\partial t}\right)$ can be described as the rate of change of any physical property $\phi(\mathbf{r}, t)$ with respect to a fixed location in space. Lagrangian, material or substantial derivative $\left(\frac{\mathrm{D}\phi}{\mathrm{D}t}\right)$ is defined as the rate of change of any physical property $\phi(\mathbf{r}, t)$ following a moving fluid particle. The material derivative of a physical property ϕ can be determined by using chain rule considering all the changes due to independent variables along the path line:

$$\begin{aligned} \frac{\mathrm{D}\phi}{\mathrm{D}t} &= \frac{\partial \phi}{\partial t}\frac{\mathrm{d}t}{\mathrm{d}t} + \frac{\partial \phi}{\partial x}\frac{\mathrm{d}x}{\mathrm{d}t} + \frac{\partial \phi}{\partial y}\frac{\mathrm{d}y}{\mathrm{d}t} + \frac{\partial \phi}{\partial z}\frac{\mathrm{d}z}{\mathrm{d}t} \\ &= \frac{\partial \phi}{\partial t} + u\frac{\partial \phi}{\partial x} + v\frac{\partial \phi}{\partial y} + w\frac{\partial \phi}{\partial z} \\ &= \frac{\partial \phi}{\partial t} + \mathbf{U} \cdot \nabla \phi \end{aligned} \tag{3.3}$$

where $\left(\frac{\partial \phi}{\partial t}\right)$ represents the local rate of change and $(\mathbf{U} \cdot \nabla \phi)$ denotes the convective rate of change. Equation 3.3 states that the rate of change of the physical property ϕ of a particle that moves through a flow field is equivalent to the sum of local and convective components.

3.1.3 Reynolds Transport Theorem

The conservation laws are generally applied to moving control volumes of fluid. Reynolds transport theorem assists us to determine the equivalent of the conservation laws in Eulerian approach to express these laws for fixed control volumes. The formulations of conservation laws vary slightly whether the control volume is moving or not. In order to formulate the Eulerian formulation of conservation laws, we need to define a physical property of the fluid (mass, momentum, energy, temperature, etc.) with (Φ) which has an intensive value of $\left(\phi = \frac{\mathrm{d}\Phi}{\mathrm{d}m}\right)$ in a finite small element of the fluid [46].

Considering a moving and deformable finite control volume in space, the instantaneous total rate of change of a physical property (Φ) consists of sum of the instantaneous local rate of change of (Φ) in the control volume and the net flux of (Φ) through the control surface. The net flux through an infinitesimal surface element $\mathrm{d}S$ in an infinitesimal time $\mathrm{d}t$ can be computed by $(\rho \mathbf{U_r} \cdot \mathbf{n}\mathrm{d}S\mathrm{d}t)$, where ρ is fluid density, $\mathbf{U}(\mathbf{r}, t)$ is the fluid velocity, $\mathbf{U_s}(\mathbf{r}, t)$ is the velocity of the deformed control surface, $(\mathbf{U_r}(\mathbf{r}, t) = \mathbf{U}(\mathbf{r}, t) - \mathbf{U_s}(\mathbf{r}, t))$ is the relative velocity of the flux and n is the surface normal. Reynolds transport theorem gives:

$$\left(\frac{\mathrm{d}\Phi}{\mathrm{d}t}\right)_{MV} = \frac{\mathrm{d}}{\mathrm{d}t}\left(\int_{V(t)} \phi\rho \mathrm{d}V\right) + \int_{S(t)} \phi\rho \mathbf{U_r} \cdot \mathbf{n}\mathrm{d}S \tag{3.4}$$

Considering a fixed control volume in space, the deformation component of the velocity is set to zero $(\mathbf{U_s}(\mathbf{r}, t) = 0)$. For this reason, the RHS of the equation 3.4 can be rewritten as:

$$\frac{\mathrm{d}}{\mathrm{d}t}\left(\int_{V(t)} \phi\rho \mathrm{d}V\right) = \int_V \frac{\partial}{\partial t}(\phi\rho)\,\mathrm{d}V \tag{3.5}$$

Therefore, equation 3.4 can be simplified to:

$$\left(\frac{\mathrm{d}\Phi}{\mathrm{d}t}\right)_{MV} = \int_V \frac{\partial}{\partial t}(\phi\rho)\,\mathrm{d}V + \int_S \phi\rho \mathbf{U} \cdot \mathbf{n}\mathrm{d}S \tag{3.6}$$

Applying Gauss' Divergence theorem to convert surface integral to volume integral gives:

$$\left(\frac{\mathrm{d}\Phi}{\mathrm{d}t}\right)_{MV} = \int_V \left[\frac{\partial \phi}{\partial t} + \nabla \cdot (\rho \mathbf{U} \phi)\right] \mathrm{d}V \tag{3.7}$$

By using the definition of material derivative,

$$\left(\frac{\mathrm{d}\Phi}{\mathrm{d}t}\right)_{MV} = \int_V \left[\frac{\mathrm{D}}{\mathrm{D}t}(\rho\phi) + \rho\phi \nabla \cdot \mathbf{U}\right] \mathrm{d}V \tag{3.8}$$

3.1.4 Conservation of Mass

The conservation of mass states that the matter may neither be created nor destroyed.

Considering a material volume of fluid flow of density ρ, mass m and velocity $\mathbf{U}$, Lagrangian description of mass conservation yields to:

$$\left(\frac{\mathrm{d}m}{\mathrm{d}t}\right)_{MV} = 0 \tag{3.9}$$

The conservation of mass can be rewritten in terms of Eulerian approach by using Reynolds Transport theorem:

$$\int_V \left[\frac{\mathrm{D}\rho}{\mathrm{D}t} + \rho \nabla \cdot \mathbf{U}\right] \mathrm{d}V = 0 \tag{3.10}$$

Since this integral is true for any control volume chosen in the fluid flow, the integrand is equivalent to zero. Therefore, the differential form of mass conservation equation known as continuity equation can be represented by:

$$\frac{\mathrm{D}\rho}{\mathrm{D}t} + \rho \nabla \cdot \mathbf{U} = 0 \tag{3.11}$$

The conservative form of the continuity equation can be represented by Reynolds Transport theorem as follows,

$$\int_V \left[\frac{\partial \rho}{\partial t} + \nabla \cdot (\rho \mathbf{U})\right] \mathrm{d}V = 0 \tag{3.12}$$

The integral is equivalent to zero for any control volume in the fluid flow. Therefore, the conservative form of continuity equation can be expressed as follows,

$$\frac{\partial \rho}{\partial t} + \nabla \cdot (\rho \mathbf{U}) = 0 \tag{3.13}$$

where ρ represents the fluid density and $\mathbf{U} = u\hat{i} + v\hat{j} + w\hat{k}$ denotes the velocity vector of the fluid at the location (x, y, z) at time t. In many applications, the density of the fluid (ρ) is considered constant. This assumption is valid for liquids of which the compressibility is negligible in most applications and gases of which the Mach number is below 0.3. This kind of flow is called to be incompressible. Therefore, $\mathrm{D}\rho/\mathrm{D}t = 0$ is applicable for incompressible flows. Despite this hypothesis, the effect of compressibility still needs to be considered under specific conditions based on high-pressure atmospheric flows and deep ocean environments. Since the density remains constant for incompressible flows, the continuity equation can be simplified to

$$\nabla \cdot \mathbf{U} = 0 \tag{3.14}$$

3.1.5 Conservation of Momentum

Conservation of momentum is fundamentally based on Newton's second law of motion, which states the sum of forces acting on the fluid in the control volume is equivalent to the rate of change of the momentum. These forces can be distinguished into two types; surface forces (pressure forces, normal and shear stresses, surface tension, etc.) and body forces (gravity, centrifugal and Coriolis forces, electromagnetic forces, etc.).

Newton's second law of motion:

$$\frac{\mathrm{d}\left(m\mathbf{U}\right)}{\mathrm{d}t} = \int_V \mathbf{F}\mathrm{d}V \tag{3.15}$$

where $\mathbf{F}$ is the total external forces acting on the control volume and $\mathbf{U}$ is the velocity of the particles in that control volume. Applying Reynolds Transport theorem on Newton's second law of motion leads to

$$\int_V \left[\frac{\mathrm{D}}{\mathrm{D}t}\left(\rho\mathbf{U}\right) + \left(\rho\mathbf{U}\right)\nabla \cdot \mathbf{U} - \mathbf{F}\right]\mathrm{d}V = 0 \tag{3.16}$$

The integrand should be zero, since the integral is zero.

$$\frac{\mathrm{D}}{\mathrm{D}t}\left(\rho\mathbf{U}\right) + \left(\rho\mathbf{U}\right)\nabla \cdot \mathbf{U} = \mathbf{F} \tag{3.17}$$

The non-conservative form of the momentum equation can be derived by expanding the material derivative of the momentum term;

$$\rho \frac{\mathrm{D}\mathbf{U}}{\mathrm{D}t} + \mathbf{U}\left(\frac{\mathrm{D}\rho}{\mathrm{D}t} + \rho \nabla \cdot \mathbf{U}\right) = \mathbf{F} \tag{3.18}$$

Applying the conservation of mass and expanding the material derivative, non-conservative form of the momentum equation can be simplified to

$$\rho\left[\frac{\partial \mathbf{U}}{\partial t} + (\mathbf{U} \cdot \nabla)\,\mathbf{U}\right] = \mathbf{F} \tag{3.19}$$

The conservative form of the momentum equation can be rewritten as

$$\int_V \left[\frac{\partial}{\partial t}(\rho \mathbf{U}) + \nabla \cdot (\rho \mathbf{U}\mathbf{U} - \mathbf{F})\right] \mathrm{d}V = 0 \tag{3.20}$$

Since the integral is equivalent to zero, the integrand for any control volume should be zero, as well.

$$\frac{\partial}{\partial t}(\rho \mathbf{U}) + \nabla \cdot (\rho \mathbf{U}\mathbf{U} - \mathbf{F}) = 0 \tag{3.21}$$

The RHS of the momentum equation represents the sum of total forces acting on the control surface. The forces acting on the control surface due to pressure and viscous stresses can be expressed as a total stress term σ. In Cartesian coordinates, total stress term (σ) consists of nine stress components given by

$$\sigma = \begin{pmatrix} \sigma_{xx} & \sigma_{xy} & \sigma_{xz} \\ \sigma_{yx} & \sigma_{yy} & \sigma_{yx} \\ \sigma_{zx} & \sigma_{zy} & \sigma_{zz} \end{pmatrix} \tag{3.22}$$

where the diagonal terms represent the normal stresses, the upper and lower terms represent the shear stresses. Practically, the stress tensor (σ) can be split into two distinct matrices such that

$$\sigma = \begin{pmatrix} p & 0 & 0 \\ 0 & p & 0 \\ 0 & 0 & p \end{pmatrix} + \begin{pmatrix} \tau_{xx} & \tau_{xy} & \tau_{xz} \\ \tau_{yx} & \tau_{yy} & \tau_{yx} \\ \tau_{zx} & \tau_{zy} & \tau_{zz} \end{pmatrix} = p\mathbf{I} + \tau \tag{3.23}$$

where $\mathbf{I}$ is the identity matrix and τ is the viscous stress tensor. Here, pressure forces are computed as the negative mean of three normal stress components:

$$p = -\frac{1}{3}\left(\sigma_{xx} + \sigma_{yy} + \sigma_{zz}\right) \tag{3.24}$$

Sum of the surface forces acting on the control volume can be computed by applying the divergence theorem;

$$\int_V \mathbf{F_S} \mathrm{d}V = \int_S \sigma \cdot \mathbf{n} \mathrm{d}S = \int_V \nabla \cdot \sigma \mathrm{d}V \tag{3.25}$$

The viscosity remains constant in the control volume for Newtonian flows. Therefore, the RHS of the momentum equations can be further simplified.

$$\frac{\partial}{\partial t}\left(\rho \mathbf{U}\right) + \nabla \cdot \left(\rho \mathbf{U}\mathbf{U}\right) = -\nabla p + \mu \nabla^2 \mathbf{U} + \mathbf{F_B} \tag{3.26}$$

Body forces can arise due to several effects such as gravitational forces, rotational motion, magnetic and electric forces, etc. The force acting due to the weight of the control volume is called gravitational force and represented by

$$\mathbf{F_B} = \rho \mathbf{g} \tag{3.27}$$

where the gravitational acceleration is denoted by $\mathbf{g}$.

Moreover, the fluid flow problem might contain arising body forces due to rigid body motion. These forces can be computed with the sum of Coriolis and centrifugal forces given below:

$$\mathbf{F_B} = \underbrace{-2\rho\left(\boldsymbol{\omega} \times \mathbf{U}\right)}_{\text{Coriolis forces}} - \underbrace{\rho\left(\boldsymbol{\omega} \times \left(\boldsymbol{\omega} \times \mathbf{R}\right)\right)}_{\text{Centrifugal forces}} \tag{3.28}$$

where $\boldsymbol{\omega}$ represents the angular velocity and $\mathbf{R}$ is the position vector. Due to the fact that gravitational and centrifugal forces are based on the position, they can be defined as a separate variable and absorbed into modified pressure and can be ignored based on the given boundary conditions. Contrary to this, Coriolis forces should be computed explicitly [44].

3.2 FINITE VOLUME METHOD

The transport equations governing the fluid flow and the integration over a control volume is discussed in Section 3.1. In this section, the discretization process of this integration is represented by finite volume (control volume) method.

The general expression of the transport equation is given by,

$$\frac{\partial \rho\phi}{\partial t} + \nabla \cdot \left(\rho \mathbf{U} \phi\right) - \nabla \cdot \left(\rho \Gamma_\phi \nabla_\phi\right) = S_\phi\left(\phi\right) \tag{3.29}$$

where, ρ is the fluid density, ϕ is the transported quantity, $\mathbf{U}$ is the fluid velocity, Γ_ϕ is the diffusion coefficient and S_ϕ is the source term, respectively. Equation 3.29 is a second order partial differential equation that provides a good accuracy for the discretization. In Navier-Stokes equations, ϕ is set for 1.0 for conservation of mass, while ϕ is assigned as $\mathbf{U}$ for the conservation of momentum. In momentum equation, the pressure term is included in the source term S_ϕ, while the source term is 0 for conservation of mass. Integrating the Equation 3.29 over an infinite time period and the control volume V_P gives;

$$\int_t^{t+\delta t} \left[\int_{V_\mathrm{P}} \frac{\partial \rho\phi}{\partial t} + \int_{V_\mathrm{P}} \nabla \cdot \left(\rho \mathbf{U} \phi\right) \mathrm{d}V - \int_{V_\mathrm{P}} \nabla \cdot \left(\rho \Gamma_\phi \nabla \phi\right) \mathrm{d}V\right] \mathrm{d}t = \int_t^{t+\delta t} \left[\int_{V_\mathrm{P}} S_\phi\left(\phi\right) \mathrm{d}V\right] \mathrm{d}t \tag{3.30}$$

Next, the discretization of general transport equation will be assumed as second order both in time and space. Therefore, all dependent variables are assumed to differ linearly around at cell center P,

$$\begin{gathered} \phi(\mathbf{x}) = \phi_{\mathrm{P}} + (\mathbf{x} - \mathbf{x}_{\mathrm{P}}) \cdot (\nabla\phi)_{\mathrm{P}}, \quad \phi = \phi(\mathbf{x}_{\mathrm{P}}) \\ \phi(t + \delta t) = \phi^t + \delta t \left(\frac{\partial\phi}{\partial t}\right) \end{gathered} \tag{3.31}$$

where, ϕ_{P} is the value of transported variable at cell center P, and ϕ^t is the value of $\phi(x)$ at time t.

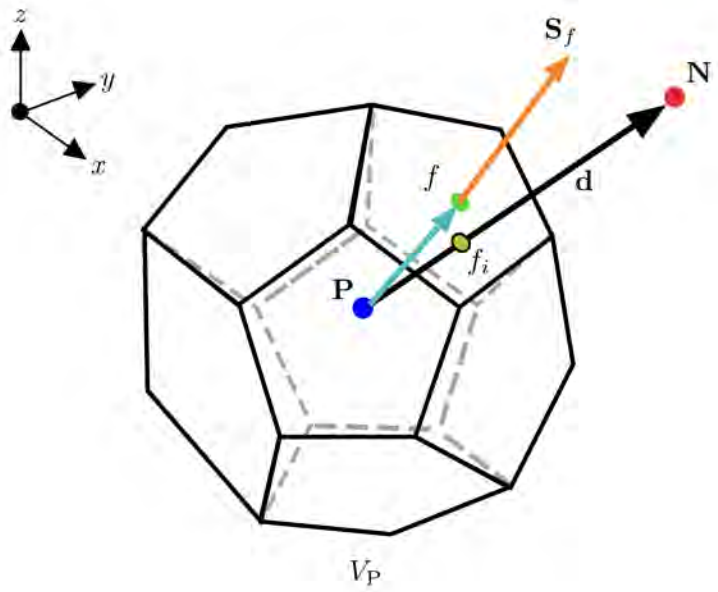

Figure 3.2: Finite volume cell [1].

The first step in finite volume method is to express the physical domain via computational domain by dividing into finite number of control volumes. In the finite volume method, the domain information can be simplified by using the following notations for each cell, shown in Figure 3.2. Here, V_{P} represents the control volume around the cell center P, $\mathbf{d}$ denotes the vector from the center of the primary cell P

to the center of the neighbor cell N, f represents the surface centers of the control volume, f_i indicates the intersection of the vector $\mathbf{d}$ and $\mathbf{S}_f$ expresses the face area vector pointing out from the control volume that is located at the face center and has a magnitude of face area.

In Figure 3.2, the center of primary cell (P) is given by,

$$\int_{V_\mathrm{P}} (\mathbf{x} - \mathbf{x}_\mathrm{P})\, \mathrm{d}V = 0 \tag{3.32}$$

and the face center (f)

$$\int_{\mathbf{S}_\mathrm{f}} (\mathbf{x} - \mathbf{x}_\mathrm{P})\, \mathrm{d}S = 0 \tag{3.33}$$

It is considered that all variables are calculated at center of the control volume that are denoted by,

$$\phi_p = \bar{\phi} = \frac{1}{V_\mathrm{P}} \int_{V_\mathrm{P}} \phi\,(\mathbf{x})\, \mathrm{d}V \tag{3.34}$$

Spatial derivative expressions can be converted to integrals over the cell faces by using Divergence theorem,

$$\int_V \nabla \cdot \phi \mathrm{d}V = \oint_{\partial V} \mathrm{d}\mathbf{S} \cdot \phi \tag{3.35}$$

where ϕ represents any tensor field and $\mathbf{S}$ is surface area vector, ∂V_P is a closed surface defining the control volume. The Divergence theorem states that the net flux of a vector field through a closed surface is equivalent to the volume integral of its divergence over the region inside the surface [44]. At this point, applying Divergence theorem on the general transport equation assists reducing to interpolated values of the cell centered values to the face centers.

$$\frac{\partial}{\partial t} \int_{V_\mathrm{P}} \rho\phi \mathrm{d}V + \oint_{\partial V_\mathrm{P}} \mathrm{d}\mathbf{S} \cdot (\rho \mathbf{U} \phi) - \oint_{\partial V_\mathrm{P}} \mathrm{d}\mathbf{S} \cdot (\rho \Gamma_\phi \nabla \phi) = \int_{V_\mathrm{P}} S_\phi\,(\phi)\, \mathrm{d}V \tag{3.36}$$

The convective, diffusive, gradient and source terms can be derived by using Gauss Divergence theorem, respectively.

$$
\begin{aligned}
\oint_{\partial V_{\mathrm{P}}} \mathrm{d}\mathbf{S} \cdot (\rho \mathbf{U} \phi) &= \sum_f \int_f \mathrm{d}\mathbf{S} \cdot (\rho \mathbf{U} \phi)_f \approx \sum_f \int_f \mathbf{S}_f \cdot \left(\overline{\rho \mathbf{U} \phi}\right)_f \\
&= \sum_f \int_f \mathbf{S}_f \cdot (\rho \mathbf{U} \phi)_f \\
\oint_{\partial V_{\mathrm{P}}} \mathrm{d}\mathbf{S} \cdot (\rho \Gamma_\phi \nabla \phi) &= \sum_f \int_f \mathrm{d}\mathbf{S} \cdot (\rho \Gamma_\phi \nabla \phi)_f \approx \sum_f \int_f \mathbf{S}_f \cdot \left(\overline{\rho \Gamma_\phi \nabla \phi}\right)_f \\
&= \sum_f \int_f \mathbf{S}_f \cdot (\rho \Gamma_\phi \nabla \phi)_f \\
(\nabla \phi)_{\mathrm{P}} &= \frac{1}{V_{\mathrm{P}}} \sum_f (\mathbf{S}_f \phi_f) \\
\int_{V_{\mathrm{P}}} S_\phi(\phi)\, \mathrm{d}V &= S_c V_{\mathrm{P}} + S_p V_{\mathrm{P}} \phi_{\mathrm{P}}
\end{aligned}
\tag{3.37}
$$

The semi-discrete form of the general transport equation can be derived by using Equation 3.37.

$$
\frac{\partial}{\partial t} \int_{V_{\mathrm{P}}} \rho \phi \mathrm{d}V + \sum_f \int_f \mathbf{S}_f \cdot (\rho \mathbf{U} \phi)_f - \sum_f \int_f \mathbf{S}_f \cdot (\rho \Gamma_\phi \nabla \phi)_f = S_c V_{\mathrm{P}} + S_p V_{\mathrm{P}} \phi_{\mathrm{P}} \tag{3.38}
$$

where the convective $\left(F^C\right)$ and diffusive fluxes $\left(F^D\right)$ are computed by interpolation schemes.

$$
\begin{aligned}
F^C &= \mathbf{S}_f \cdot (\rho \mathbf{U} \phi) \\
F^D &= \mathbf{S}_f \cdot (\rho \Gamma_\phi \nabla \phi)
\end{aligned}
\tag{3.39}
$$

3.2.1 Spatial Discretization

The convection term is complicated to solve numerically, and therefore there are several methods developed. The biggest handicap of the convective term is that low-order schemes cause numerical diffusion, while high order schemes result in numerical

dispersion error. The first method is the linear interpolation or central differencing scheme to compute the flux term between two neighboring cells. Central differencing scheme is second-order and unbounded. Therefore, second order derivatives and higher order terms are neglected, and it can generate oscillatory solutions. The central differencing scheme is illustrated in Figure 3.3.

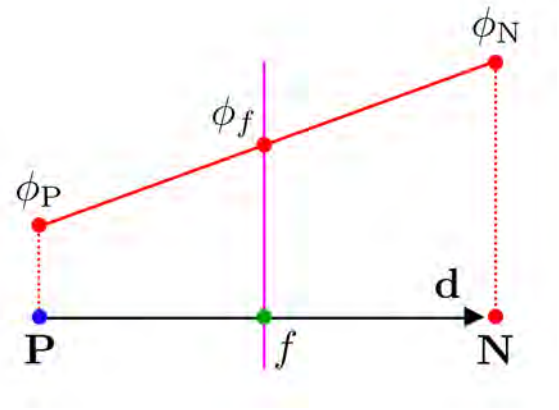

Figure 3.3: Central differencing scheme [1].

$$\phi_x = f_x \phi_P + (1 - f_x)\, \phi_N \quad \text{where} \quad f_x = \frac{fN}{PN} = \frac{|x_f - x_N|}{|\mathbf{d}|} \tag{3.40}$$

Another method is the upwind differencing scheme overcomes the disadvantages of the central differencing scheme by considering the direction of the flow. This scheme is adequate for dominant convective flows. The upwind differencing scheme is first order accurate, bounded, but diffusive. It can also be named with respect to the direction of the flow.

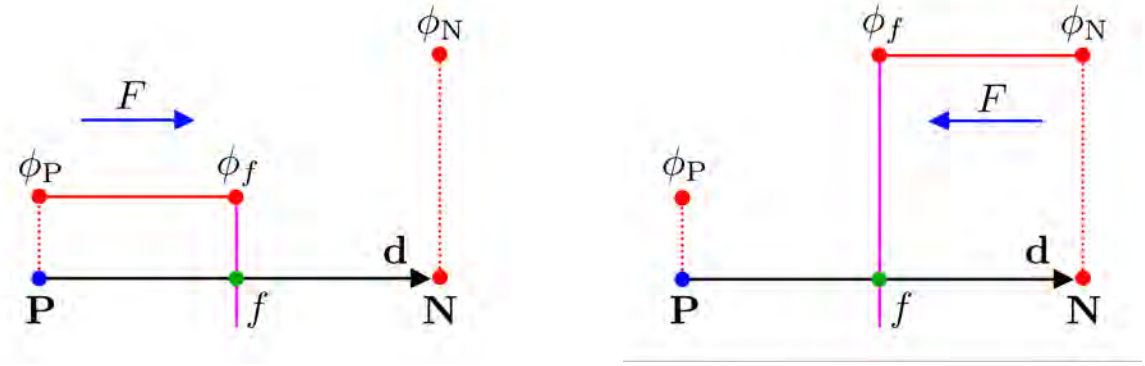

(a) Forward upwind. (b) Backward upwind.

Figure 3.4: Upwind differencing schemes [1].

The upwind differencing scheme is illustrated in Figure 3.4. The face value is determined by

$$\phi_f = \begin{cases} \phi_P & \text{if} \quad F \geq 0 \\ \phi_N & \text{if} \quad F < 0 \end{cases} \tag{3.41}$$

Another second order accurate scheme is linear upwind differencing scheme known as Beam-Warming scheme that can be unbounded in case of highly convective flows, or strong gradients. The linear upwind differencing scheme is illustrated in Figure 3.5 for neighboring cells.

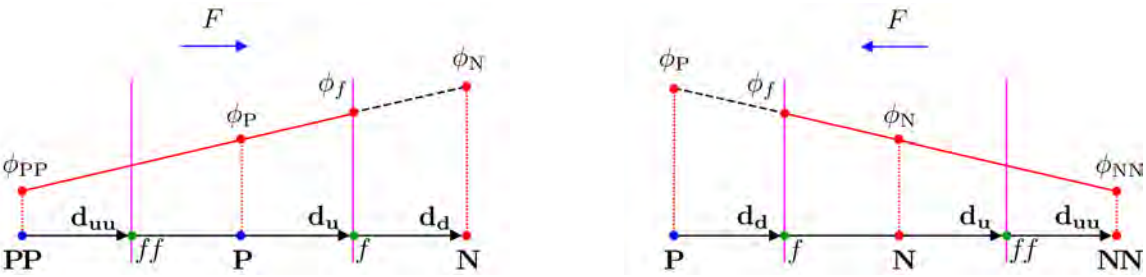

(a) Forward linear upwind. (b) Backward linear upwind.

Figure 3.5: Linear upwind differencing schemes [1].

It defines the face value by,

$$\phi_f = \begin{cases} \phi_{\mathrm{P}} + \frac{1}{2}\left(\phi_{\mathrm{P}} - \phi_{\mathrm{PP}}\right) & \text{if} \quad F \geq 0 \\ \phi_{\mathrm{N}} + \frac{1}{2}\left(\phi_{\mathrm{N}} - \phi_{\mathrm{NN}}\right) & \text{if} \quad F < 0 \end{cases} \tag{3.42}$$

A gradient limiter function ($\psi(r)$) is generally applied to prevent boundedness. When the limiter function ($\psi(r)$) detects strong gradients, it switches to a low order scheme (upwind). The idea of using a limiter function ($\psi(r)$) is based on observing the ratio of consecutive gradients.

$$\phi_f = \begin{cases} \phi_{\mathrm{P}} + \frac{1}{2}\phi_{\mathrm{P}}^{-}\left(\phi_{\mathrm{P}} - \phi_{\mathrm{PP}}\right) & \text{if} \quad F \geq 0 \\ \phi_{\mathrm{N}} + \frac{1}{2}\phi_{\mathrm{P}}^{+}\left(\phi_{\mathrm{N}} - \phi_{\mathrm{NN}}\right) & \text{if} \quad F < 0 \end{cases} \tag{3.43}$$

It is straightforward to design a Total Variation Diminishing (TVD) scheme that is second order accurate and bounded by adding a good limiter function ($\psi(r)$). TVD schemes do not undershoot or overshoot during the computation or amplify high resolution. In addition, the choice of $\psi(r)$ defines the order of accuracy and boundedness. The downside of using a limiter function is that the accuracy decreases locally to the first order in case of sharp gradients. However, it suppresses the oscillations. There are various type of limiters such as vanLeer, SuperBee and MinMod, that can be selected in accordance with the particular problem.

$$\begin{aligned} r_{\mathrm{P}}^{-} &= \frac{\phi_{\mathrm{N}} - \phi_{\mathrm{P}}}{\phi_{\mathrm{P}} - \phi_{\mathrm{PP}}} \\ r_{\mathrm{P}}^{+} &= \frac{\phi_{\mathrm{P}} - \phi_{\mathrm{N}}}{\phi_{\mathrm{N}} - \phi_{\mathrm{NN}}} \end{aligned} \tag{3.44}$$

The convective and diffusive terms are two distinct terms that must be treated differently. The discretization of the diffusive term is straightforward, and it can be approximated by using the central differencing scheme that is a second-order and unbounded approach, which might cause oscillations.

3.2.2 Temporal Discretization

The semi-discrete form of the general transport equation is given with Equation 3.38. After discretizing the convective and diffusive terms, we proceed with temporal discretization by using the Method of Lines (MOL) method. The fundamental benefit of MOL is allowing us to choose numerical approximations with various accuracy for temporal and spatial expressions in the general transport equation. Therefore, each expression will have different accuracy.

Afterwards, it is straightforward to use any time discretization scheme, e.g., Crank-Nicolson, Euler implicit, forward Euler, backward differencing, Adams-Bashforth or Adams-Moulton. It is important that the order of the temporal discretization does not need to have the same order the spatial terms do. Each term can be discretized with different approximation methods which can yields to different accuracies. The overall accuracy is going to be second order, considering all the individual terms are at least second order accurate.

After the discretization procedure is completed, a system of algebraic equations for the transported quantity ϕ can be solved in every control volume.

$$[\mathbf{A}] \times [\phi] = [\mathbf{b}] \tag{3.45}$$

3.3 FREE SURFACE FLOWS

Free surface flow is a branch of moving boundary flows where the position of the boundary is known at an initial time and can be determined in the following time. Therefore, there are two boundary conditions that should be applied on the free surface. The kinematic boundary condition requires that there will be a sharp interface between phases where there is no mass flux through it, given below:

$$[\mathbf{U} - \mathbf{U} \cdot \mathbf{n}]_{fs} = 0 \tag{3.46}$$

Equation 3.46 states that the normal component of the fluid velocity and the normal component of the free surface velocity are equivalent. The dynamic boundary condition requires that the momentum is conserved at the free surface. Therefore, the forces acting on the free surface should be in equilibrium. This boundary condition applies that the normal forces acting on the free surface are equal magnitude and opposite direction, and the tangential forces acting on the free surface are equal magnitude and direction.

$$\begin{aligned} \kappa &= \frac{1}{R_t} + \frac{1}{R_s} \\ (\mathbf{n} \cdot T)_{liquid} \cdot \mathbf{n} + \boldsymbol{\sigma}\kappa &= -(\mathbf{n} \cdot T)_{gas} \cdot \mathbf{n} \\ (\mathbf{n} \cdot T)_{liquid} \cdot \mathbf{t} - \frac{\partial \boldsymbol{\sigma}}{\partial t} &= -(\mathbf{n} \cdot T)_{gas} \cdot \mathbf{t} \\ (\mathbf{n} \cdot T)_{liquid} \cdot \mathbf{s} - \frac{\partial \boldsymbol{\sigma}}{\partial s} &= -(\mathbf{n} \cdot T)_{gas} \cdot \mathbf{s} \end{aligned} \tag{3.47}$$

Here, $(\mathbf{n}, \mathbf{t}, \mathbf{s})$ represents the unit vectors in local coordinate system at the free surface and κ is the curvature of the free surface. The surface tension (σ) is a property of a liquid that depends on the temperature and the attraction between the particles. It can be defined as the force acting on the tangential direction per unit length of the free surface element. Therefore, the total surface tension force can be calculated by

$$\mathbf{F}_\sigma = \boldsymbol{\sigma} \mathrm{d}l \tag{3.48}$$

The surface tension forces acting on the tangential direction cancel out for an infinitesimally small element when $\boldsymbol{\sigma}$ is sustained. The normal components of the surface tension forces can be defined as an external force that actually causes a pressure jump over the free surface, as shown in Equation 3.47. In industrial applications, the shear stresses acting on the free surface can be neglected. Additionally, the normal stress components and free-surface tension can be ignored. In this case, the dynamic boundary condition at the free surface is simplified to $p_{liquid} = p_{gas}$.

There are several methods to define the location of the free surface that can besimplified to the following groups.

3.3.1 Interface-Capturing Methods

The general principle of interface-capturing methods is computing the fraction by partially filled cells near the interface to determine the shape of free surface at the fixed grid instead of defining an interface as a boundary. One method depends on the motion of massless particles at the interface, called Marker and Cell (MAC) Scheme, proposed by Harlow and Welch [47]. MAC Scheme is an exquisite approach for complex free-surface flows. However, it is computationally expensive in three dimensions when it is coupled with governing equations. Another method is computing a transport equation for volume fraction of the liquid on the cell, known as Volume of Fluid (VoF) method, proposed by Hirt and Nichols [48]. In VoF approach, the fraction of each control volume is represented by α, so that $\alpha = 0$ denotes the empty control volumes, while $\alpha = 1$ indicates the filled control volumes [49]. The transport equation can be defined by;

$$\frac{\partial \alpha}{\partial t} + \nabla \cdot (\alpha \mathbf{U}) = 0 \tag{3.49}$$

To find the original location of the free surface, the whole domain can be treated as a single fluid, where a weight function can be defined to describe the phase;

$$\begin{aligned} \rho &= \rho_1 \alpha + \rho_2 (1 - \alpha) \\ \mu &= \mu_1 \alpha + \mu_2 (1 - \alpha) \end{aligned} \tag{3.50}$$

In this case, there is no free-surface boundary. Therefore, kinematic and dynamic boundary conditions do not need to be prescribed. Nevertheless, Equation 3.49 satisfies the kinematic boundary condition and the dynamic boundary condition is implicitly considered. Hence, the surface tension effects are non-negligible on the

free-surface, the effect should be considered as a body force. The surface tension effects the partially filled cells around the free surface. Since the gradient of volume fraction (α) on the full and empty cells is equivalent to zero, the surface tension force can be described by continuum surface approach, proposed by Brackbill [50]:

$$\mathbf{F}_\sigma = \int_V \boldsymbol{\sigma} \kappa \nabla \alpha \mathrm{d}V \tag{3.51}$$

When the surface tension becomes dominant, the pressure term and the body forces denoting the surface tension effects become larger in the momentum equations and these terms have to balance each other. Since the free-surface curvature depends on volume fraction (α), it is problematic to define pressure and volume fraction as identicals in three-dimensions.

$$\kappa = \nabla \cdot \mathbf{n} = -\nabla \cdot \left(\frac{\nabla \alpha}{|\nabla \alpha|} \right) \tag{3.52}$$

Another critical issue is the discretization of the convective term in Equation 3.49. Because first-order schemes smear the interface, while higher order schemes can be oscillatory causing undershoots or overshoots by violating the condition:

$$0 < \alpha < 1 \tag{3.53}$$

There are several methods to overcome this problem by ensuring a sharp interface and a monotone profile of volume fraction (α) through the free-surface [51, 52, 53, 54]. The best alternative form was proposed by Weller et al. (2008) [55], introducing an artificial compression term to the right-hand side of Equation 3.49.

$$\frac{\partial \alpha}{\partial t} + \nabla \cdot (\alpha \mathbf{U}) + \nabla \cdot [\mathbf{U}_c \alpha (1 - \alpha)] = 0 \tag{3.54}$$

where $\mathbf{U}$ is the mean velocity, $\mathbf{U}_c$ is the relative velocity between two liquids, also represented as compression velocity [91]. The compression velocity can be calculated by

$$\mathbf{U}_c = C_\alpha \left| \frac{\phi}{\mathbf{S}_f} \right| \mathbf{n} \tag{3.55}$$

The boundedness of this equation is achieved by MULES (multidimensional universal limiter for explicit solution). MULES uses a limiter factor of the fluxes of divergence term to ensure the final value of volume fraction (α) is between 0 and 1 [56].

Another branch of interface-capturing methods is level-set approach, proposed by Osher and Sethian et al. (1998) [57]. According to this approach, $\phi = 0$ defines the free-surface, whereas the value of ϕ is defined by the distance from the surface and can be signed positive at one side of the surface and negative on the other side. This function can be represented by a solution of transport equation:

$$\frac{\partial \phi}{\partial t} + \nabla \cdot (\phi \mathbf{U}) = 0 \tag{3.56}$$

where $\mathbf{U}$ represents the fluid velocity and the surface on $\phi = 0$ is the free-surface. The advantage of level-set method is ϕ smoothly differs across the free-surface, while there are discontinuities in volume fraction (α) on the free-surface.

In level set methods, the step-wise variation in physical properties of the liquids are maintained:

$$\rho = \begin{cases} \rho_{liquid} & \phi < 0 \\ \rho_{gas} & \phi > 0 \end{cases} \tag{3.57}$$

However, this condition is not applicable for viscous flows. In viscous flows, there must be a region with a finite thickness where the physical properties rapidly and smoothly change on the free-surface.

In level-set methods, ϕ needs to re-initialized. Sussmann et al. (1994) proposed an approach to solve this problem by

$$\frac{\partial \phi}{\partial \tau} = \operatorname{sgn} \phi_0 \left(1 - |\nabla \phi|\right) \tag{3.58}$$

This approach ensures that ϕ and ϕ_0 have the same sign and zero level that satisfies the condition $|\nabla \phi|$. The original level-set method does not conserve the mass. Conservation of mass can be enforced by defining the right-hand side of Equation 3.58 as a function of local imbalance [58].

Interface-capturing methods are the most widely used in commercial codes for computing free-surface flows including submerged bodies flow around ships, slamming bodies and droplet-wall interactions.

3.3.2 Interface-Tracking Methods

In order to calculate the free surface flow around a submerged object, there are studies based on linearization about the undisturbed free surface. This approach requires a height function $\zeta = H(x, y, t)$, which is the position of the free surface relative to the unperturbed state.

Applying the kinematic boundary condition on H gives

$$\frac{\partial H}{\partial t} = u_z - u_x \frac{\partial H}{\partial x} - u_y \frac{\partial H}{\partial y} \tag{3.59}$$

Equation 3.59 can be integrated in time explicitly. The fluid velocity on the free surface can be obtained by using dynamic boundary condition or extrapolation. There are several studies by using finite volume method for the height equation with enforcing boundary conditions on the free surface [59, 60, 61, 62].

The crucial problem in interface-tracking methods is that the movement of the free surface affects stability. The reason is that the indication of numerous grid nodes needs to be computed, while there is only one discrete equation per cell on the free surface. Correct approaches should be applied at the intersection of the boundaries with the free-surface to avoid wave reflection or instability [62].

Free-surface flows such as flow around submerged bodies or open channel flows are generally associated with Froude number.

$$Fr = \frac{U}{\sqrt{gL_{ref}}} \tag{3.60}$$

where U is the reference velocity, g is gravitational acceleration and L_{ref} is the reference length. When $Fr < 1$, wave particles can move in all directions. However, $Fr > 1$ the velocity of the fluid exceeds the wave speed and wave particles cannot move in the upstream direction.

The methods used to compute free-surface is extremely crucial since small waves can generate disturbances which causes convergence problems for a steady-state solution. At locations where there should not be waves physically, methods that do not generate waves satisfy the radiation condition.

3.3.3 Hybrid Methods

Hybrid methods are the combination of interface-capturing and interface-tracking methods where the physical properties of both liquids are smeared over grid points normal to the free-surface. Both phases are treated as a single fluid. The velocity field is used to compute the movement of marker particles that are removed and added to keep equivalent distance between them. At the end of each time step, the physical properties are re-computed [63].

3.4 TURBULENCE MODELING

Turbulence modeling is the construction and use of a mathematical model to predict the effects of turbulence. Turbulent flows are common place in most real life scenarios, including the flow of blood through the cardiovascular system, the airflow over an aircraft wing, the re-entry of space vehicles, besides others. In spite of decades of research, there is no analytical theory to predict the evolution of these turbulent

flows. The equations governing turbulent flows can only be solved directly for simple cases of flow. For most real life turbulent flows, CFD simulations use turbulent models to predict the evolution of turbulence. These turbulence models are simplified constitutive equations that predict the statistical evolution of turbulent flows.

3.4.1 Kolmogorov Scale

The first discovery of turbulence is based on an experiment performed by Osborne Reynolds, in which he discovered that there are two different states of flow could occur in pipe flow [64]. The first state called laminar flow where the adjacent fluid layers move smoothly with respect to each other. Therefore, laminar flow has a smooth shaped velocity distribution. The second state is called turbulent, where the flow showed chaotic, unsteady characteristics with various sizes of eddies. For turbulent flows, the time-averaged velocity distribution can be defined in two dimensions. However, the instantaneous velocity fluctuates in three spatial dimensions, rapidly.

The turbulence modeling is based on the energy cascade theory developed by Kolmogorov, where the turbulence contains different sizes of eddies which surpasses its energy to another one. The large eddies terminate and transfer their energies to the small eddies in a chain process, and small eddies encounter the same process and share their power with the smaller ones. This process pursues until it is reached to the smallest eddy size. The molecular viscosity is very effective on dissipating the turbulent kinetic energy at the smallest eddy size [65, 66]. The smallest eddy size is represented by the Kolmogorov micro-length (η) and time scale (t_η) denoted by

$$\eta = \left(\frac{\nu^3}{\epsilon}\right)^{\frac{1}{4}} \tag{3.61}$$

$$t_\eta = \left(\frac{\nu}{\epsilon}\right)^{\frac{1}{2}} \tag{3.62}$$

where ν is the molecular kinematic viscosity and ϵ is the dissipation rate of turbulent kinetic energy.

3.4.2 Reynolds Averaging

ϕ represents instantaneous value of any physical fluid property at a discrete time t and position $\mathbf{x}$. ϕ can be decomposed into a mean variable $\left(\overline{\phi}\right)$ and (ϕ') as shown in Figure 3.6:

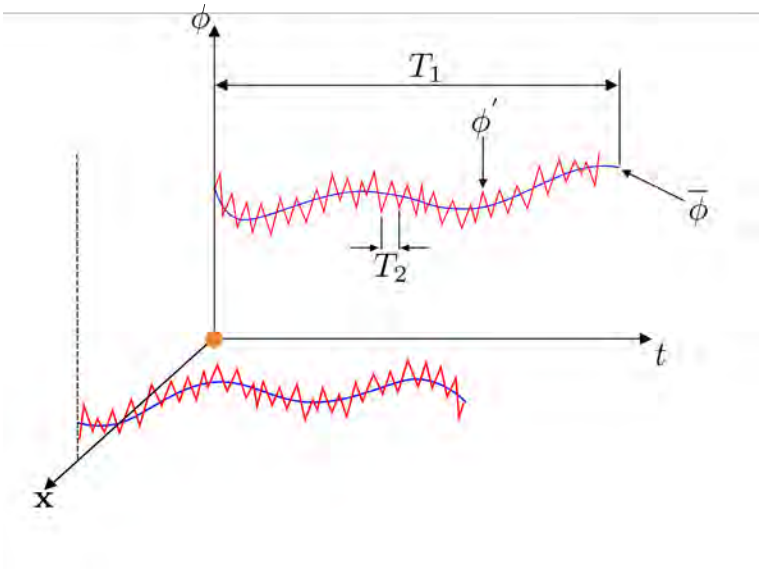

Figure 3.6: Fluctuations of transported quantities [1].

$$\phi(\mathbf{x},t) = \underbrace{\overline{\phi}(\mathbf{x},t)}_{\text{Mean component}} + \underbrace{\phi'(\mathbf{x},t)}_{\text{Fluctuating component}} \tag{3.63}$$

Here, $\overline{\phi}$ can be computed by any Reynolds averaging methods [23].

Time Averaging

Time averaging technique represent the mean of any physical property (ϕ) over a time interval. This method is applicable for steady flows where the flow on average does not vary with time itself. Applying averaging over a time interval T gives:

$$\overline{\phi}\left(\mathbf{x},t\right)=\lim_{T\to\infty}\frac{1}{T}\int_{t}^{t+T}\phi\left(\mathbf{x},t\right)\mathrm{d}t \tag{3.64}$$

Spatial Averaging

Spatial averaging is used for averaging of any physical property ϕ over a space interval or a control volume. Therefore, $\bar{\phi}$ depends on only time t:

$$\overline{\phi}\left(t\right)=\lim_{V\to\infty}\frac{1}{V}\int_{V}\phi\left(\mathbf{x},t\right)\mathrm{d}V \tag{3.65}$$

Ensemble Averaging

Ensemble averaging represents the mean of several identical properties at a certain time t, that is also applicable for unsteady flows. Here N, represents the number of identical quantities, which eliminates the effects of turbulent fluctuations.

$$\overline{\phi}\left(\mathbf{x},t\right)=\lim_{N\to\infty}\frac{1}{N}\sum_{i=1}^{N}\phi\left(\mathbf{x},t\right) \tag{3.66}$$

3.4.3 Incompressible RANS Equations

The incompressible RANS equations are based on substitution of time-averaged variables into the governing equations of fluid motion. Applying Reynolds decomposition to the physical properties gives:

$$\begin{aligned} p&=\overline{p}+p^{'}\\ \mathbf{U}&=\overline{\mathbf{U}}+\mathbf{U}^{'}\\ \overline{\mathbf{U}}&=\overline{u}\mathbf{i}+\overline{v}\mathbf{j}+\overline{w}\mathbf{k}\\ \mathbf{U}^{'}&=u^{'}\mathbf{i}+v^{'}\mathbf{j}+w^{'}\mathbf{k} \end{aligned} \tag{3.67}$$

Substituting these variables into time-averaged incompressible Navier-Stokes equations for a Newtonian fluid gives:

$$\overline{\nabla \cdot \left[\rho\left(\overline{\mathbf{U}}+\mathbf{U}'\right)\right]} = 0$$
$$\overline{\frac{\partial}{\partial t}\left[\rho\left(\overline{\mathbf{U}}+\mathbf{U}'\right)\right]+\nabla\cdot\left[\rho\left(\overline{\mathbf{U}}+\mathbf{U}'\right)\left(\overline{\mathbf{U}}+\mathbf{U}'\right)\right]} = \overline{-\nabla\left(\overline{p}+p'\right)+\nabla\cdot\left(\mu\left[\nabla\left(\overline{\mathbf{U}}+\mathbf{U}'\right)+\nabla\left(\overline{\mathbf{U}}+\mathbf{U}'\right)^{\intercal}\right]\right)+\mathbf{F_B}} \tag{3.68}$$

Then, the Reynolds-averaged Navier-Stokes equations transform into:

$$\begin{gathered}\nabla\cdot\left[\rho\overline{\mathbf{U}}\right]=0\\ \frac{\partial}{\partial t}\left[\rho\overline{\mathbf{U}}\right]+\nabla\cdot\left(\rho\overline{\mathbf{U}}\overline{\mathbf{U}}\right)=-\nabla\overline{p}+\left[\nabla\cdot\left(\overline{\boldsymbol{\tau}}-\rho\overline{\mathbf{U}}\overline{\mathbf{U}}\right)\right]+\overline{\mathbf{F_B}}\end{gathered} \tag{3.69}$$

Equation 3.69 seem very similar to the governing equations of the fluid motion. However, the momentum equation includes non-linear terms that are due to turbulent fluctuations. Therefore, six new unknown variables are added to the momentum equation. These unknown variables are called Reynolds stress tensor $\left(\boldsymbol{\tau}^{\boldsymbol{R}}\right)$ and given by,

$$\boldsymbol{\tau}^{\boldsymbol{R}}=-\rho\begin{pmatrix}\overline{u'u'} & \overline{u'v'} & \overline{u'w'}\\ \overline{v'u'} & \overline{v'v'} & \overline{v'w'}\\ \overline{w'u'} & \overline{w'v'} & \overline{w'w'}\end{pmatrix} \tag{3.70}$$

The RANS equations are not in a coupled form, and the Reynolds stress tensor needs to be computed by an appropriate turbulence model. It is evident that the Reynolds stress tensor is a non-linear convection expression in the momentum equation, and this non-linearity must be described in terms of averaged components by any model.

3.4.4 Boussinesq Hypothesis

The Boussinesq hypothesis is an analogy that determines the Reynolds stress tensor by modeling via a linear function as the averaged velocity gradients.

$$\boldsymbol{\tau}^{\boldsymbol{R}}=\rho\overline{\mathbf{U}'\mathbf{U}'}=\mu_t\left[\nabla\mathbf{U}+(\nabla\mathbf{U})^{\intercal}\right]-\frac{2}{3}\left[\rho k+\mu_t\left(\nabla\cdot\mathbf{U}\right)\right]\mathbf{I} \tag{3.71}$$

For incompressible flows, Equation 3.71 can be further simplified:

$$\boldsymbol{\tau^R} = \rho\overline{\mathbf{U}'\mathbf{U}'} = \mu_t\left[\nabla\mathbf{U} + (\nabla\mathbf{U})^\intercal\right] - \frac{2}{3}\rho k\mathbf{I} \tag{3.72}$$

In Equation 3.72, the pressure term (p) can be combined by the term $\left(\frac{2}{3}k\mathbf{I}\right)$. Here, the turbulent kinetic energy is denoted by k, and turbulent eddy viscosity is represented by ν_t. The turbulent kinetic energy can be computed by,

$$k = \frac{1}{2}\overline{\mathbf{U}'\mathbf{U}'} \tag{3.73}$$

The Boussinesq hypothesis assists us in transforming the problem of computing the Reynolds stress term into the determination of turbulent kinetic energy and turbulent eddy viscosity.

3.4.5 Reynolds Stress Equation Models

There are several turbulence models based on Boussinesq hypothesis to determine the turbulent viscosity in terms of velocity and turbulent length scales (l):

$$\mu_t = \rho l\sqrt{k} \tag{3.74}$$

The turbulence models can be divided into four fundamental categories:

- Zero-equation models
- One-equation models
- Two-equation models
- Second-order closure models

The zero equation models are developed to compute (μ_t) straightforwardly without requiring any differential equation. The one-equation models use one transport

equation to compute (μ_t), while two-equation models use various distinct transport equations to calculate discrete turbulent fluxes. Second-order models are widely used in industrial applications due to highly accurate predictions with low-cost computations.

Standard $k-\epsilon$ Turbulence Model

The standard $k-\epsilon$ turbulence modelis based on the Bousssinesq hypothesis by using the thermal diffusivity (k_t), and the turbulent viscosity (μ_t):

$$\mu_t = \rho C_\mu \frac{k^2}{\epsilon} \tag{3.75}$$

and

$$k_t = \frac{c_p \mu_t}{\mathrm{Pr}_t} \tag{3.76}$$

where the dissipation rate of turbulent kinetic energy (ϵ):

$$\epsilon = \frac{1}{2}\frac{\mu}{\rho}\overline{[\nabla \mathbf{U}' + (\nabla \mathbf{U}')^\intercal] : [\nabla \mathbf{U}' + (\nabla \mathbf{U}')^\intercal]} \tag{3.77}$$

In standard $k-\epsilon$ turbulence model, turbulent kinetic energy and turbulent kinetic energy dissipation rate are computed by two distinct equations;

$$\begin{aligned} \frac{\partial}{\partial t}(\rho k) + \nabla \cdot (\rho \mathbf{U} k) &= \nabla \cdot \left[\left(\mu + \frac{\mu_t}{\sigma_k}\right)\nabla k\right] + P_k - \rho\epsilon \\ \frac{\partial}{\partial t}(\rho \epsilon) + \nabla \cdot (\rho \mathbf{U} \epsilon) &= \nabla \cdot \left[\left(\mu + \frac{\mu_t}{\sigma_\epsilon}\right)\nabla \epsilon\right] + C_{\epsilon 1}\frac{\epsilon}{k}P_k - C_{\epsilon 2}\rho\frac{\epsilon^2}{k} \end{aligned} \tag{3.78}$$

where the turbulent Prandtl number is denoted by (Pr_t). The model constants are assigned to the following values in Table 3.1.

Table 3.1: Model constants of standard $k-\epsilon$ turbulence model.

$\mathbf{Pr}_t$	$\boldsymbol{C_{\epsilon 1}}$	$\boldsymbol{C_{\epsilon 2}}$	$\boldsymbol{C_\mu}$	$\boldsymbol{\sigma_k}$	$\boldsymbol{\sigma_\epsilon}$
0.90	1.44	1.92	0.09	1.00	1.30

The production of turbulent energy (P_k) can be described in a compact form:

$$P_k = \tau^{\mathbf{R}} : \nabla \mathbf{U} \tag{3.79}$$

The original derivation of the standard $k-\epsilon$ turbulence model states that the flow is fully turbulent, and therefore, the effects of molecular viscosity are neglected. In this case, the standard $k-\epsilon$ turbulence model is feasible for fully turbulent, High-Reynolds numbers and free-shear slows, in which the boundary layer flow cannot be integrated into the wall. To model the boundary layer flow around a solid body with the standard $k-\epsilon$ turbulence model, the equations must be integrated over a fine enough mesh to capture the turbulence quantities accurately. Low-Reynolds number turbulence models are one of the approaches suggested, integrating two unknown variables to the solid body. Low-Reynolds number $k-\epsilon$ turbulence models damp the viscosity through a damping function [67].

The main disadvantage of two-equation models is the stagnation point problem, in which the models can over-predict the turbulent kinetic energy production in high strain regions. For this reason, a bounding approach on the local turbulent timescale (t_s) is proposed by Medic et al [68]. The turbulent timescale is given by:

$$t_s = \frac{k}{\epsilon} \tag{3.80}$$

and the turbulent viscosity is reformulated by;

$$\mu t = \rho C_\mu k t_s \tag{3.81}$$

The ϵ equation is transformed and represented in terms of the local turbulent timescale (t_s)

$$\frac{\partial}{\partial t}(\rho\epsilon) + \nabla \cdot (\rho \mathbf{U} \epsilon) = \nabla \cdot \left[\left(\mu + \frac{\mu_t}{\sigma_\epsilon} \right) \nabla \epsilon \right] + C_{\epsilon 1} \frac{1}{t_s} P_k - C_{\epsilon 2} \rho \frac{\epsilon}{t_s} \tag{3.82}$$

Furthermore, the Reynolds stress tensor $\left(\boldsymbol{\tau}^{\boldsymbol{R}}\right)$ must be limited to remain positive. Therefore, the turbulent timescale (t_s) is limited by;

$$t_s = \min\left[\frac{k}{\epsilon}, \frac{\alpha}{\sqrt{6}C_\mu S_t}\right] \tag{3.83}$$

where $\alpha = 0.6$, $S_t = \sqrt{\mathbf{S}_t \cdot \mathbf{S}_t}$ and $\mathbf{S}_t = \frac{1}{2}\left(\nabla\mathbf{U} + (\nabla\mathbf{U})^\intercal\right)$.

Standard $k-\omega$ Turbulence Model

Despite the fact that $k-\epsilon$ turbulence models are applicable for free shear flows, they are poor models for predicting the flows with adverse pressure gradients. However, converting the dissipation rate of turbulent kinetic energy (ϵ) into specific turbulent dissipation (ω) overcomes separation phenomena. This approach was developed by Kolomogorov et al. [69], in which ω acts a turbulent timescale (t_s) and the turbulent length scale (l) is given by;

$$l = \frac{\sqrt{k}}{\omega} \tag{3.84}$$

The standard $k-\omega$ turbulence model is developed by Wilcox et al., in which is based on Boussinessq hypothesis [70, 71]. The standard $k-\omega$ turbulence model uses two transport equations to compute the two large scales of eddies, in which replacing ϵ with ω increases the robustness of the simulation. Additionally, the standard $k-\omega$ turbulence model does not require damping functions to resolve the boundary layer, since it is effective with weak adverse pressure gradients. The specific turbulent dissipation rate (ω):

$$\omega = \frac{\epsilon}{C_\mu k} \tag{3.85}$$

The standard $k-\omega$ turbulence model equations are given by

$$\begin{aligned}
\frac{\partial}{\partial t}(\rho k) + \nabla \cdot (\rho \mathbf{U} k) &= \nabla \cdot \left[\left(\mu + \frac{\mu_t}{\sigma_{k1}} \right) \nabla k \right] + P_k - \beta^* \rho k \omega \\
\frac{\partial}{\partial t}(\rho \omega) + \nabla \cdot (\rho \mathbf{U} \omega) &= \nabla \cdot \left[\left(\mu + \frac{\mu_t}{\sigma_{\omega 1}} \right) \nabla \omega \right] + \frac{\gamma \omega}{k} P_k - \beta \rho \omega^2
\end{aligned} \tag{3.86}$$

The model constants are assigned to the following values in Table 3.2.

Table 3.2: Model constants of standard $k - \omega$ turbulence model.

$\mathbf{Pr}_t$	$\boldsymbol{\gamma}$	$\boldsymbol{\beta}$	$\boldsymbol{\beta^*}$	$\boldsymbol{\sigma_{k1}}$	$\boldsymbol{\sigma_{\omega 1}}$
0.90	5/9	0.075	0.09	0.50	0.50

The major disadvantage of standard $k - \omega$ turbulence model is its sensitivity to the initial values assigned at free-stream. Therefore, the solution depends on the initialization [72].

Baseline (BSL) $k - \omega$ Turbulence Model

The Baseline (BSL) $k - \omega$ turbulence model was proposed by Menter et al. [72]. It is the combination of standard $k - \epsilon$ and $k - \omega$ turbulence models that take the strength of both models. It is robust as the standard $k - \omega$ model, based on the low Reynolds number formulation. Therefore, it can compute flows with adverse weak pressure gradients with high accuracy. This model provides a better resolution in the far-field as standard $k - \epsilon$ turbulence model due to the independence of free-stream values. This model uses a modified $k - \omega$ model based on the standard $k - \epsilon$ model [72].

$$\begin{aligned}
\frac{\partial}{\partial t}(\rho k) + \nabla \cdot (\rho \mathbf{U} k) &= \nabla \cdot \left[\left(\mu + \frac{\mu_t}{\sigma_{k2}} \right) \nabla k \right] + P_k - \beta^* \rho k \omega \\
\frac{\partial}{\partial t}(\rho \omega) + \nabla \cdot (\rho \mathbf{U} \omega) &= \nabla \cdot \left[\left(\mu + \frac{\mu_t}{\sigma_{\omega 2}} \right) \nabla \omega \right] + \frac{\gamma}{\nu_t} P_k - \beta \rho \omega^2 + 2 (1 - F_1) \frac{\rho \sigma_{\omega 2}}{\omega} \nabla k \cdot \nabla \omega
\end{aligned} \tag{3.87}$$

The difference between Equation 3.87 and Equation 3.86 is the cross-diffusion term. Multiplying Equation 3.87 with blending function yields the Baseline (BSL)

formulation. The blending function (F_1) depends on the solution variants and the nearest wall distance ($d_\perp$).

$$\begin{aligned} F_1 &= \tanh\left(\gamma_1^4\right) \\ \gamma_1 &= \min\left(\max\left(\frac{\sqrt{k}}{\beta^* \omega \left(d_\perp\right)^2}, \frac{500\nu}{\left(d_\perp\right)^2 \omega}\right), \frac{4\rho\sigma_{\omega 2} k}{CD_{k\omega}\left(d_\perp\right)^2}\right) \\ CD_{k\omega} &= \max\left(2\rho\sigma_{\omega 2}\frac{1}{\omega}\nabla k \cdot \nabla\omega, 10^{-20}\right) \end{aligned} \tag{3.88}$$

The model constants are given in Table 3.3.

Table 3.3: Model constants of Baseline (BSL) $k-\omega$ turbulence model.

$\mathbf{Pr}_t$	$\boldsymbol{C_{\alpha 1}}$	$\boldsymbol{C_{\alpha 2}}$	$\boldsymbol{C_{\beta 1}}$	$\boldsymbol{C_{\beta 2}}$	$\boldsymbol{\beta^*}$	$\boldsymbol{\sigma_{k1}}$	$\boldsymbol{\sigma_{k2}}$	$\boldsymbol{\sigma_{\omega 1}}$	$\boldsymbol{\sigma_{\omega 2}}$
0.9	0.5976	0.4404	0.075	0.0828	0.09	2.0	1.0	2.0	1.0

Shear-Stress Transport (SST) $k-\omega$ Turbulence Model

The shear-stress transport (SST) $k-\omega$ turbulence model is a modified version of the baseline $k-\omega$ model that comparatively provides an accurate estimation of adverse pressure gradients. It satisfies Bradshaw's hypothesis on the linear relationship between turbulent kinetic energy (k) and the shear stress (τ_{xy}) calculated in the boundary layer.

$$\tau_{xy} = \rho a_1 k \tag{3.89}$$

In conventional two-equation models, the shear stress is computed by

$$\tau_{xy} = \mu_t \boldsymbol{\Omega} \tag{3.90}$$

in which the vorticity is denoted by $\boldsymbol{\Omega}$. Bradshaw's hypothesis is irrelevant, since the production of turbulent kinetic energy (k) is much larger than the dissipation (ω) [73]. Therefore, the turbulent viscosity is bounded by

$$\nu_t = \frac{\rho a_1 k}{\max\left(a_1\omega, \sqrt{2}S_t F_2\right)} \tag{3.91}$$

where F_2 is blending function.

$$\begin{aligned} F_2 &= \tanh\left(\gamma_2^2\right) \\ \gamma_2 &= \max\left(\frac{\sqrt{k}}{\beta^* d_\perp}, \frac{500\nu}{\left(d_\perp\right)^2 \omega}\right) \end{aligned} \tag{3.92}$$

Another modification is necessary for the turbulent kinetic energy production (P_k).

$$\tilde{P}_k = \min\left(P_k, 20\beta^*\rho k\omega\right) \tag{3.93}$$

The SST turbulence model equations are:

$$\begin{aligned} \frac{\partial}{\partial t}\left(\rho k\right) + \nabla\cdot\left(\rho\mathbf{U}k\right) &= \nabla\cdot\left[\left(\mu + \frac{\mu_t}{\sigma_{k2}}\right)\nabla k\right] + P_k - \beta^*\rho k\omega \\ \frac{\partial}{\partial t}\left(\rho\omega\right) + \nabla\cdot\left(\rho\mathbf{U}\omega\right) &= \nabla\cdot\left[\left(\mu + \frac{\mu_t}{\sigma_{\omega 2}}\right)\nabla\omega\right] + \frac{\gamma}{\nu_t}P_k - \beta\rho\omega^2 + 2\left(1-F_1\right)\frac{\rho\sigma_{\omega 2}}{\omega}\nabla k\cdot\nabla\omega \end{aligned} \tag{3.94}$$

3.5 PRESSURE-VELOCITY COUPLING ALGORITHMS

Pressure-velocity coupling is one of the significant phenomena. Solving the discretized form of incompressible Navier-Stokes equations requires that the velocity field be known beforehand in momentum equations that satisfy the continuity equation. The convective terms are non-linear in the momentum equations. Additionally, momentum equations are coupled since velocity components are included in each equation and the continuity equation. There are no equations solving pressure terms explicitly, even though it appears in each momentum equation. Therefore, it is clear that pressure gradient is the most important term in momentum equations [74].

The pressure field could be computed explicitly from the discretized momentum equations if the pressure gradient is known beforehand. The continuity equation works as a density transport function for compressible flows, while the energy equation

operates as a temperature transport equation. Therefore, the pressure field could be straightforwardly obtained using the state equation. For incompressible flows, density remains constant, and it is not related to the pressure field. Hence, a coupling between pressure and velocity fields is necessary to solve the flow field. The sequential procedure for solving the Navier-Stokes equations can be achieved using SIMPLE, PISO, and PIMPLE algorithms.

The discretized continuity and momentum equations are given below, respectively.

$$\begin{aligned} \int_V \nabla \cdot \mathbf{U} \mathrm{d}V &= \sum_f \mathbf{S}_f \cdot \mathbf{U}_f \\ a_\mathrm{P} \mathbf{U}_\mathrm{P}^n + \sum_\mathrm{N} a_\mathrm{N} \mathbf{U}_\mathrm{N}^n &= Q_\mathrm{P}^n - (\nabla p)_\mathrm{P}^n \end{aligned} \tag{3.95}$$

(Q_P^n) is an expression that includes all the terms with regard to the velocity field.

$$\begin{aligned} H(\mathbf{U}) &= Q_\mathrm{P} - \sum_\mathrm{N} a_\mathrm{N} \mathrm{U}_\mathrm{N} \\ a_\mathrm{P} \mathbf{U}_\mathrm{P} = Q_\mathrm{P} - \sum_\mathrm{N} a_\mathrm{N} \mathbf{U}_\mathrm{N} - (\nabla p)_\mathrm{P} &= \mathbf{H}(\mathbf{U}) - (\nabla p)_\mathrm{P} \end{aligned} \tag{3.96}$$

In Equation 3.96, $(\mathbf{H}(\mathbf{U}))$ the matrix coefficients of the velocity field, and the right-hand contains the unsteady terms. The discretized continuity equation can be rewritten by subtracting $(\mathbf{U}_f)$.

$$\begin{aligned} \mathbf{U}_f &= \left[\frac{\mathbf{H}(\mathbf{U})}{a_\mathrm{P}}\right]_f - \left[\frac{1}{a_\mathrm{P}}\right](\nabla p)_f \\ \sum_f \mathbf{S}_f \cdot \left[\left[\frac{1}{a_\mathrm{P}}\right]_f\right] &= \sum_f \mathbf{S}_f \cdot \left[\frac{\mathbf{H}(\mathbf{U})}{a_\mathrm{P}}\right]_f \end{aligned} \tag{3.97}$$

Finally, the discretized governing equations of fluid flow are transformed into the following matrices.

$$\begin{aligned} a_\mathrm{P} \mathbf{U}_P &= \mathbf{H}(\mathbf{U}) - \sum_f S(p)_f \\ \sum_f \mathbf{S}_f \cdot \left[\left[\frac{1}{a_\mathrm{P}}\right]_f\right] &= \sum_f \mathbf{S}_f \cdot \left[\frac{\mathbf{H}(\mathbf{U})}{a_\mathrm{P}}\right]_f \end{aligned} \tag{3.98}$$

in which $\left(\sum_f S\left(p\right)_f\right)$ is the discrete form of the pressure gradient (∇p). The face flux (F) can be computed by,

$$F = \mathbf{S}_f \mathbf{U}_f - \mathbf{S}_f \cdot \left[\left[\frac{\mathbf{H}\left(\mathbf{U}\right)}{a_{\mathrm{P}}}\right]_f - \left[\frac{1}{a_{\mathrm{P}}}\right]_f \left(\nabla p\right)_f\right] \tag{3.99}$$

3.5.1 Semi-Implicit Method for Pressure Linked Equations (SIMPLE) Algorithm

The SIMPLE algorithm is based on guess and correct loop for solving the pressure in Poisson equation, proposed by Patankar and Spalding (1972) for steady-state problems [75].

The solution process can be summarized as follows:

- The velocity field is computed from the momentum equation. The pressure gradient term is computed by using the pressure distribution from the previous time step or initial guess. Then the velocity equation is under-relaxed with an under-relaxation factor (α_U).
- A new pressure equation is solved to determine the new pressure field.
- The fluxes are computed by using Equation 3.99. The pressure field needs to be corrected, since the new pressure field contains pressure and convection-diffusion errors. Therefore, the pressure field needs to be approximated and ($\mathbf{H}\left(\mathbf{U}\right)$) coefficients needs to be recomputed with the fluxes. The pressure field then under-relaxed via (α_p) in order to consider velocity errors.

$$\phi_{\mathrm{P}}^{n} = \phi_{\mathrm{P}}^{n-1} + \alpha\left(\phi_{\mathrm{P}}^{n*} - \phi_{\mathrm{P}}^{n-1}\right) \tag{3.100}$$

Here, (ϕ_{P}^{n}) represents the approximated pressure distribution that is going to be used for momentum predictor step, $\left(\phi_{\mathrm{P}}^{n-1}\right)$ is the pressure field used in the momentum

predictor step, (ϕ_{P}^{n*}) is the solution of the pressure equation and (α) is the under-relaxation factor. The under-relaxation factors are generally a typical feature of steady-state problems, which controls the change of the variable (ϕ).

3.5.2 Pressure Implicit with Splitting of Operators (PISO) Algorithm

The pressure-velocity coupling for unsteady problems are originally proposed by Issa [76]. The PISO algorithm can be summarized as follows:

- The first step is the momentum predictor step, where the momentum equation is solved. Since the pressure gradient term is not known, the data from the previous time step is used to predict the new velocity field.
- This step is the pressure solution step, where the predicted velocity field is used to assemble ($\mathbf{H}(\mathbf{U})$) operator, and the pressure equation is formulated to estimate the new pressure field.
- This step is the velocity corrector step, in which the computed fluxes are corrected due to the new pressure field.

Equation 3.96 illustrates that the velocity corrector contains the transported corrections in the velocity field and the change in the pressure gradient. In the velocity corrector step, the transported corrections due to neighboring cells are neglected. Therefore, it is necessary to correct the ($\mathbf{H}(\mathbf{U})$) term to compute a new pressure field until the tolerance is reached.

PISO algorithm at least one correction step and increasing the number of corrections definitely improve the accuracy and the stability of the computation. For non-orthogonal meshes, at least one corrector step stabilizes the solution. Additionally, adding momentum predictor step stabilizes the solution and provide better approximations for the velocity.

The main difference of PISO algorithm is the time derivation term and the consistency of the coupling equation. Therefore, the fields are not under-relaxed, but the stability criteria must be satisfied by Courant-Friedrichs-Lewy (CFL) condition. CFL condition requires that the information from one cell to another must reach at most in one time-step. This stability criteria is obtained as:

$$\mathrm{Co} = \frac{|\mathbf{U}|\,\Delta t}{\Delta x} \tag{3.101}$$

3.5.3 Pressure Implicit with Splitting of Operators with Iterative Marching (PIMPLE) Algorithm

The PIMPLE algorithm is simply a combination of SIMPLE and PISO algorithms that enables the usage of large time-steps, and specially developed under OpenFOAM®. The PIMPLE algorithm uses SIMPLE algorithm in every time-step with multiple outer iterations to solve the pressure-Poisson equation. Then the solution goes through a PISO algorithm for the pressure field with multiple non-orthogonal correctors. Then, the velocity and fluxes are corrected, and the information is used for the next time step in the SIMPLE algorithm. This loop continues until the convergence criteria is reached [77].

The details of the pressure-velocity coupling methods used in OpenFOAM®, can be found in Moukalled et al. (2016) [78].

3.6 WAVE GENERATION

3.6.1 Introduction

It is necessary to determine the forces applied to the vehicles operating in the ocean to understand the wave-ship interaction. This phenomenon can be achieved by approximating the wave pressure field; the kinematics of water particles formulates that. An undulation of the calm water surface disturbs the pressure distribution through the basin, in which the total pressure is no longer only dependent on hydrostatic pressure. The motion of the water column affects the vertical acceleration of the water particles. Therefore, the governing equations of fluid motion are used to find the velocity and pressure field of the wave motion. There is no such thing as a universal theory that can be used to model the wave motion due to the different characteristics of a wave, since there are various identities of wave inducers.

3.6.2 Wave Modeling

The water wave theories provide a great understanding of the ocean and coastal structures under different wave conditions. The well-known Morison equation is widely used to estimate the wave forces acting on the structures, which neglects the induction of wave kinematics due to the existence of the structure. This assumption depends on the accuracy and the dimension difference between the wave and structure.

Experimental, analytical, and numerical approaches can be used to deal with wave-ship interaction problems. In the experimental approach, the prototype itself or the model scale of the prototype is used to investigate the problem with appropriate measurements and correlation of the results. The experimental studies on wave-structure interactions provide significant physical explanations of the phenomenon at the cost of model production and scale effects. Analytical methods are the solutions of partial differential equations that define the boundary value problem by modeling

the kinematics and dynamics of the water particles around the ship. In this method, simplifications are applied, in which fewer dominant terms are neglected. Numerical methods are based on the solution of governing equations and relevant boundary conditions, in which the wave-ship interaction problem is treated differently than the analytical approach. In the numerical approach, the equations are discretized by solving linear systems of equations by using matrices. Additionally, the governing equations of fluid motion remain unchanged, and the physical boundary conditions are used to create well-posed and diagonally dominant matrices. In this case, the only approximation is accomplished by the discretization methods.

In the study of wave dynamics, viscous effects are mostly negligible due to the substantial structure dimensions and the strength of the motion of water particles. Therefore, incompressible and inviscid flow with the assumption of irrotational flow can simplify this phenomenon into a potential flow problem, in which velocity potential terms are used, and the problem is solved by the application of linearized dynamic and kinematic boundary conditions. To describe the three-dimensional wave motion by velocity potential ϕ, continuity equation transforms into the Laplace equation:

$$\nabla^2\phi = \frac{\partial^2\phi}{\partial x^2} + \frac{\partial^2\phi}{\partial y^2} + \frac{\partial^2\phi}{\partial z^2} \tag{3.102}$$

where x and y coordinates in the horizontal direction and z is in the vertical direction.

Linear boundary conditions specify the periodicity of wave characteristics in time and space and the velocity components on the seafloor due to permeability. Non-linear boundary conditions are divided into two groups. Dynamic free-surface boundary conditions depend on the force balance on the free surface. The kinematic free-surface boundary condition expresses the relationship between the vertical velocities of the particles on the water surface and the wave elevation.

The wave theories are classified into two fundamental groups depending on the

treatment of non-linear boundary conditions. In each category, there are various types of wave theories applicable for different ocean environment.

3.6.3 Linear Wave Theory

Linear wave theory is commonly called airy wave theory or Stokes first order wave theory, that is used for modeling gravity waves on a fluid surface. Linear wave theory is widely used in ocean and coastal engineering to model tsunami waves approaching to the shoreline. This theory is used for approximation of wave characteristics, since it is accurate for small fraction of wave height of wavelength in both shallow and deep-water regions. In linear wave theory, the non-linear boundary conditions are linearized, and the phenomena are modeled through a second-order partial differential equation by applying linearized boundary conditions to the physical problem. The dynamic boundary condition is described by the unsteady Bernoulli equation as:

$$-\frac{\partial \phi}{\partial t}+\frac{1}{2}\left(\nabla \phi\right)^{2}+g\eta=C\left(t\right) \quad \text{on} \quad z=\eta\left(x,t\right) \tag{3.103}$$

And the kinematic boundary condition can be found by the application of dynamic boundary condition on the free surface, where $p=0$;

$$-\frac{\partial \phi}{\partial z}=\frac{\partial \eta}{\partial t}-\frac{\partial \phi}{\partial x}\frac{\partial \eta}{\partial x} \quad \text{on} \quad z=\eta\left(x,t\right) \tag{3.104}$$

The simplest way to linearize the non-linear free-surface boundary conditions is approximating the boundary conditions on the free-surface via Taylor series expansion around the still water level and ignoring higher-order terms. In this case, the boundary value problem has an analytical solution, allowing to find velocity potential by using separation of variables [79]. The kinematics of particles and pressure distribution can be calculated by:

$$u=\frac{H}{2}\omega\frac{\cosh\left(k\left(h+z\right)\right)}{\sinh\left(kh\right)}\cos\left(kx-\omega t\right) \tag{3.105}$$

$$w = \frac{H}{2}\omega \frac{\sinh\left(k\left(h+z\right)\right)}{\sinh\left(kh\right)} \sin\left(kx - \omega t\right) \tag{3.106}$$

$$p = -\rho g z + \rho g \frac{H}{2} \frac{\cosh\left(k\left(h+z\right)\right)}{\cosh\left(kh\right)} \cos\left(kx - \omega t\right) \tag{3.107}$$

The velocity and pressure terms depend on the time and horizontal space, in which are governed by periodic trigonometric functions, while the dependence of vertical space is governed by hyperbolic functions. In linear wave theory, the wave is described by a basic sine or cosine functions, in which the wave crests and trough follow the equivalent patterns, the water particles follow closed orbits. The shape of the orbits depend on the water depth and the pressure has no longer hydrostatic distribution due to the change in vertical acceleration of water particles.

The propagation of water waves is dispersive, therefore waves with different wavelengths and periods have different celebrities. This relationship is explained through dispersion relationship:

$$\omega^2 = gk \tanh\left(kh\right) \tag{3.108}$$

Even though the linear theory is an excellent approach to describe wave motions, its relevancy range is limited since the significance of non-linear terms becomes more considerable. Therefore, non-linear wave theories are capable of predicting large wave motions widely observed in the ocean.

3.6.4 Non-linear Wave Theory

The dynamic and kinematic free-surface boundary conditions in nonlinear wave theories are determined differently than in linear theories. Stokes wave theories are named after the degree of non-linearity is considered.

Generally, dynamic and kinematic free surface boundary conditions in nonlinear theories are treated differently than linear ones. The well-known Stokes wave theory

describes a group of nonlinear water waves, named according to the degree of nonlinearity described by them. Nonlinear waves can be defined via the solution of partial differential equations by perturbation methods. Perturbation method is an astonishing approach, in which the behavior of the particular system is determined by the variation of the perturbation parameter. The solution is described as the expansion of perturbation parameter:

$$x = X_0 + \epsilon X_1 + \epsilon^2 X_2 + \epsilon^3 X_3 + O\left(\epsilon^4\right) \tag{3.109}$$

The exact solution can be reached by adding higher-order terms depending on the value of the perturbation parameter (ϵ). In Stokes wave theory, wave steepness ($k\zeta$) is the perturbation parameter and inclusion of this particular parameter in the governing equations and boundary conditions results for the solution of Stokes wave with higher-order. However, after third-order expansion, this approach becomes difficult.

3.6.5 Stokes V Wave Theory

Fifth order Stokes wave theory is based on modelling the behavior of deep water waves [80]. The potential flow theory is used to find the analytical solution of inviscid incompressible fluid. The velocity potential and wave profile is expanded by:

$$\begin{aligned}
\frac{\beta\phi}{\overline{C}} = \frac{2\pi\phi}{L\overline{C}} &= \left(\lambda A_{11} + \lambda^3 A_{13} + \lambda^5 A_{15}\right)\cosh\beta S \sin\theta \\
&+ \left(\lambda^2 A_{22} + \lambda^4 A_{24}\right)\cosh 2\beta S \sin 2\theta \\
&+ \left(\lambda^3 A_{33} + \lambda^5 A_{35}\right)\cosh 3\beta S \sin 3\theta \\
&+ \left(\lambda^3 A_{33} + \lambda^5 A_{35}\right)\cosh 3\beta S \sin 3\theta \\
&+ \left(\lambda^4 A_{44}\right)\cosh 4\beta S \sin 4\theta \\
&+ \left(\lambda^5 A_{55}\right)\cosh 5\beta S \sin 5\theta
\end{aligned} \tag{3.110}$$

and

$$\begin{aligned}\beta y = \lambda \cos\theta &+ \left(\lambda^2 B_{22} + \lambda^4 B_{24}\right) \cos 2\theta \\ &+ \left(\lambda^3 B_{33} + \lambda^5 B_{35}\right) \cos 3\theta \\ &+ \left(\lambda^4 B_{44}\right) \cos 4\theta \\ &+ \left(\lambda^5 B_{55}\right) \cos 5\theta\end{aligned} \tag{3.111}$$

in which the phase angle θ is calculated by,

$$\theta = \frac{2\pi}{L}\left(x - \overline{C}t\right) \tag{3.112}$$

Here, the expansions show that how A_{ij} and B_{ij} perturbation parameters are introduced to the problem. These parameters are calculated in terms of h/L. Skjelberia and Hendrickson et al. (1961) [80] proposed that the wave height corresponds to the vertical distance of the wave profile at phase angles of 0 and π. Therefore, the perturbation parameter (λ) is calculated by,

$$\frac{\pi H}{h} = \frac{L}{h}\left(\lambda + \lambda^3 B_{33} + \lambda^5 \left(B_{35} + B_{55}\right)\right) \tag{3.113}$$

The pressure and velocity term are related via the unsteady Bernoulli equation;

$$\frac{\partial \phi}{\partial t} + \frac{1}{2}\nabla\phi + \frac{p}{\rho} = -g\left(C\left(t\right) + S - h\right) \tag{3.114}$$

where the Bernoulli constant is denoted by $C\left(t\right)$. To find the analytical solution, the dispersion relation for Stokes V wave theory is proposed via

$$\frac{h}{L_0} = \frac{h}{L}\tanh\beta d\left(1 + \lambda^2 C_1 + \lambda^4 C_2\right) \tag{3.115}$$

where $L_0 = \frac{gT^2}{2\pi}$ is the wave length in deep water and C_i are polynomial expressions of the wave length. Netwon-Raphson algorithm is used to solve this iterative system. If Stokes V is applied on out of its range, a three crested waves can appear in the solution that is physically wrong.

3.6.6 Wave Breaking

The behavior of wave breaking varies from shallow water to deep water conditions. The reason waves break in shallow water is due to excessive shoaling while propagating over the shore. The shallow water waves are affected by the changes in water depth, and wave height increases as the wave propagates towards the shore. The breaking criteria for shallow water waves is simply based on wave steepness and water depth. In deep water conditions, wave break due to hydrodynamic instabilities. There are theoretical explanations to this specific phenomena, In this study, the wave breaking criteria is based on Fenton's approach [81]:

$$\left(\frac{H}{L}\right)_{max} \approx \frac{0.141063 + 0.0095721\left(\frac{2\pi}{kh}\right) + 0.0077829\left(\frac{2\pi}{kh}\right)^2}{1 + 0.0788340\left(\frac{2\pi}{kh}\right) + 0.0317567\left(\frac{2\pi}{kh}\right)^2 + 0.0093407\left(\frac{2\pi}{kh}\right)^3} \tag{3.116}$$

3.7 MOTIONS OF SIX DEGREES OF FREEDOM

The six degree of freedom (6DoF) is a dynamic mesh motion library that computes the linear and angular velocity components, forces and moments on a moving body to perform translational and rotational motion of the center of gravity in Cartesian coordinate system.

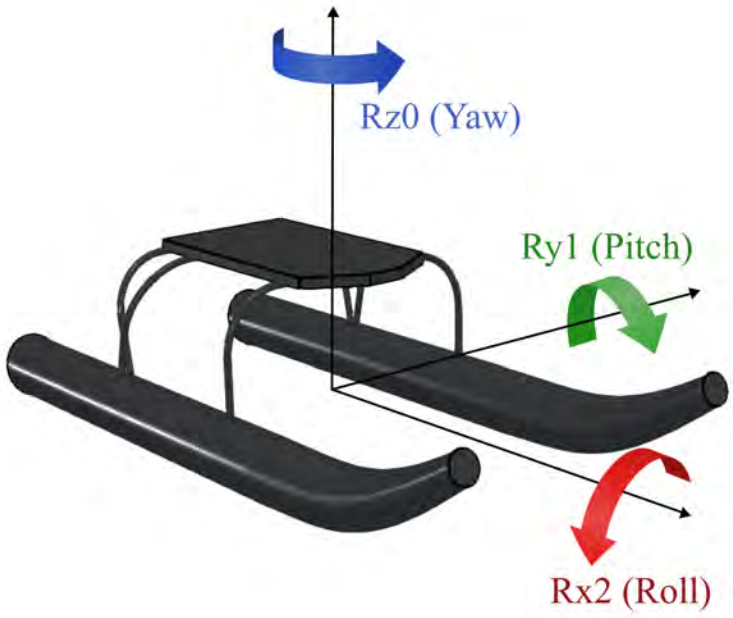

Figure 3.7: Cardan Angles represented on the catamaran model.

The translational motion of the center of gravity,

$$\mathbf{F}_G = m\dot{\mathbf{U}}_G \tag{3.117}$$

in which $\mathbf{F}_G$ is the external force vector, m is the mass and $\dot{\mathbf{U}}_G$ is the translational motion of the center of gravity. In the earth-fixed coordinates, the translational motion can be described as a dynamic equation:

$$\mathbf{F} = m\left(\dot{\mathbf{U}} + \dot{\mathbf{\Omega}} \times \mathbf{R}_G\right) + m\left[\mathbf{\Omega} \times \mathbf{U} + \mathbf{\Omega} \times (\mathbf{\Omega} \times \mathbf{R}_G)\right] \tag{3.118}$$

where $\mathbf{U} = [u, v, w]^\intercal$ is the translational velocity, $\mathbf{\Omega} = [p, q, r]$ is the angular velocity in the earth-fixed coordinates and $\mathbf{R})_G = [x_G; y_G; z_G]^\intercal$ is the position of the center of gravity in space. The transformation matrix can be described in terms of Cardan angles (ψ, θ, ϕ);

$$\mathbf{R} = \begin{bmatrix} \cos(\theta)\cos(\psi) & \cos(\theta)\sin(\psi) & -\sin(\theta) \\ \sin(\psi)\sin(\theta)\cos(\psi) - \cos(\phi)\sin(\psi) & \sin(\phi)\sin(\theta)\sin(\psi) + \cos(\phi)\sin(\psi) & \sin(\phi)\cos(\theta) \\ \cos(\phi)\sin(\theta)\cos(\psi) + \sin(\phi)\sin(\psi) & \cos(\phi)\sin(\theta)\sin(\psi) + \sin(\phi)\sin(\psi) & \cos(\phi)\cos(\theta) \end{bmatrix} \tag{3.119}$$

where $p = \dot{\phi}$, $q = \dot{\theta}$ and $r = \dot{\psi}$. Then the translational forces $\mathbf{F} = [T_x, T_y, T_z]^\intercal$ and angular moments $\mathbf{M} = [M_x, M_y, M_z]^\intercal$ acting on the floating body can be computed by:

$$\begin{aligned} \mathbf{F} &= \mathbf{R}\mathbf{F}_G \\ \mathbf{M} &= \mathbf{R}\mathbf{M}_G \end{aligned} \tag{3.120}$$

The angular motion of the hull, $\dot{\mathbf{\Omega}}$, can be computed as follows:

$$\mathbf{M} = \mathbf{I}\dot{\mathbf{\Omega}} + m\mathbf{R}_G \times \dot{\mathbf{U}} + \mathbf{\Omega} \times \mathbf{I}\mathbf{\Omega} + m\mathbf{R}_G \times (\mathbf{\Omega} \times \mathbf{U}) \tag{3.121}$$

where $\mathbf{I}$ is the moment of inertia matrix,

$$\mathbf{I} = \begin{bmatrix} \mathbf{I}_{xx} & \mathbf{I}_{xy} & \mathbf{I}_{xz} \\ \mathbf{I}_{yx} & \mathbf{I}_{yy} & \mathbf{I}_{yz} \\ \mathbf{I}_{zx} & \mathbf{I}_{zy} & \mathbf{I}_{zz} \end{bmatrix} \tag{3.122}$$

Hence $\mathbf{I}_{ij}$ is the moment of inertia of the floating body for $i = j$ in earth-fixed coordinates system, it can be represented by:

$$\begin{aligned} \mathbf{I}_{xx} &= \mathbf{I}_{xx_G} + m\left(y_G^2 + z_G^2\right) \\ \mathbf{I}_{yy} &= \mathbf{I}_{yy_G} + m\left(x_G^2 + z_G^2\right) \\ \mathbf{I}_{zz} &= \mathbf{I}_{zz_G} + m\left(x_G^2 + y_G^2\right) \\ \mathbf{I}_{xy} &= \mathbf{I}_{yx} = \mathbf{I}_{xy_G} + mx_G y_G \\ \mathbf{I}_{xz} &= \mathbf{I}_{zx} = \mathbf{I}_{xz_G} + mx_G z_G \\ \mathbf{I}_{yz} &= \mathbf{I}_{zy} = \mathbf{I}_{yz_G} + my_G z_G \end{aligned} \tag{3.123}$$

Six-degrees of freedom rigid body motions of a hull in the earth-fixed coordinate system can be represented by six non-linear coupled equations. The instantaneous forces and moments acting on the hull needs to be defined to solve the 6DoF motion equations. Therefore, the pressure and viscous forces acting on ship should be integrated over the ship surface. The total force and moment acting on the hull can be represented by:

$$\mathbf{F}_G = m\mathbf{g} + \int_{ship} \mathrm{d}\mathbf{F}_S \mathbf{M}_G = \mathbf{R}_G \times m\mathbf{g} + \int_{ship} \mathbf{R}_i \mathrm{d}\mathbf{F}_S \tag{3.124}$$

where $\mathrm{d}\mathbf{F}_S$ is the surface force of an infinitesimal element on the ship.

3.8 OVERSET (CHIMERA) GRIDS

The overset (Chimera) grid approach provides the capability to solve complex configurations of large body motions. In this concept, two or more domains are allowed to overlap, and the solution is interpolated between them. This method provides good mesh quality for each domain and unlimited complexity of body motions. When this approach is being used, a background domain containing the physical boundaries and a separate domain surrounding the rigid body are created and meshed separately. Since the overlapping domain moves within the background domain, the overlapping cells will change. The information between cells will be transferred via blanking approach. In the blanking approach, the equations are solved in active cells, blanked cells are left temporarily non-active and interpolated cells receive the information from each domain.

Even though overset approach is a remarkable method for modeling of complex body motions, it is based on several number of interpolations between overlapping computational grids, which can lead to difficulties for mass conservation. As a result, convergence instabilities including oscillations can be observed.

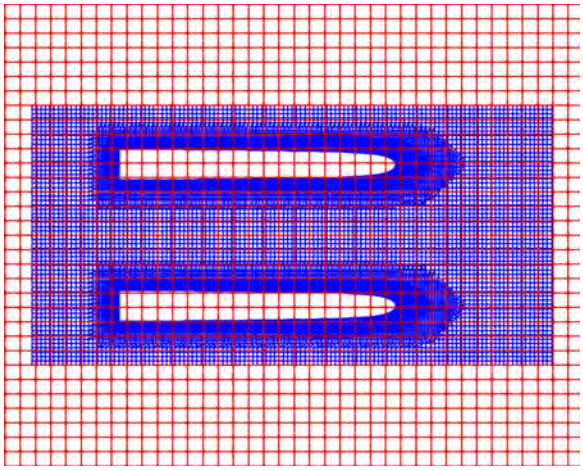

Figure 3.8: Overset (Chimera) grid structure.

In Figure 3.8, the zones are determined by color. The red zone belongs to the background domain. The blue zone is the zone around the rigid body. Each domain include interpolating cells. The cells around the rigid body (blanked cells in overset mesh) are actually in background mesh, and their donors are located in overset mesh. The interpolation can be performed by various interpolation schemes:

- cellVolumeWeight
- inverseDistance
- leastSquares
- trackingInverseDistance

In this study, *inverseDistance* method is being used. In inverseDistance method the interpolated cells are acceptor cells, that their donors are interpolated and send the information into acceptor cells. Donor cells are marked from the nearest cells and marked for closest donors. In this method, the weights for the interpolation are based on the distances from the cell centers.

The weights for interpolation are determined from distances of cell centers. To compute the weights for the interpolation, the sum of inverse distances are needed.

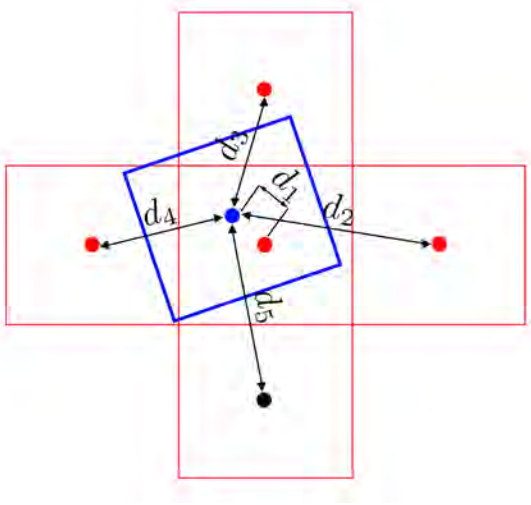

Figure 3.9: The determination of weights based on the distance of cell centers [2].

$$S = \sum_{i=1}^{N} \frac{1}{|d_i|} \tag{3.125}$$

in which the number of donors are determined by N, and the distance between the cell center of each donor and the center of the acceptor cell are represented by d_i. In that case, the weights w_i are computed as follows:

$$w_i = \frac{\frac{1}{|d_i|}}{\sum_{i=1}^{N} \frac{1}{|d_i|}} \tag{3.126}$$

The interpolated value of the field ϕ can be computed by the addition over all neighbors

$$\phi = \sum_{i=1}^{N} w_i \phi_i \tag{3.127}$$

CHAPTER 4
VALIDATION AND VERIFICATION STUDIES

To carry out hydrodynamic performance simulations of a catamaran in calm water, the numerical approach in OpenFOAM® needs to be validated. In this case, an unsteady multiphase flow around KCS (Kris Container Ship) hull is modeled, and hence the drag coefficients, trim and sinkage data and wave profiles are validated comparing with the existing experimental data.

4.1 GEOMETRY AND TEST CONDITIONS

The main characteristics of KCS hull and its isometric 3D model is given in Table 4.1 and in Figure 4.1, respectively. The KCS hull is a 3600 TEU container ship that has a bulbous bow design. The validation data is provided recently at Tokyo 2015 A Workshop on CFD in Ship Hydrodynamics workshop. For steady-state calm water simulations, the model ship is scaled by a similarity ratio of 1/31.599. The length between perpendiculars is measured to be 7.2786 m and the draft is 0.3418 mm For unsteady simulations, the model ship is towed at different advance speed and the simulation results are compared with the experimental data.

Figure 4.1: Kriso Container Ship (KCS) hull geometry.

Table 4.1: Main particulars of KCS hull.

Main Particulars	**Symbol**	**Model 1**	**Model 2**
Scale Factor	λ	31.599	37.879
Length between perpendiculars	L_{PP}	7.2786	6.0702
Maximum beam of waterline	B_{WL}	1.0190	0.8498
Depth	D (m)	0.6013	0.5015
Design draft	T (m)	0.3418	0.2850
Displacement volume	∇ (m^3)	1.6490	0.9571
Wetted surface area	S (m^2)	9.5531	6.6978
Longitudinal center of buoyancy	LCB	-1.48	-1.48
Longitudinal center of gravity	LCG	3.53	2.945
Vertical center of gravity (from keel)	KG	0.23	0.192
Moment of inertia	K_{xx}/B_{WL}	0.40	0.39
	K_{yy}/L_{PP}	0.25	0.25
	K_{zz}/L_{PP}	0.25	0.25

Calm water-resistance simulations were conducted to define the total resistance of KCS at different advance speeds from 0.92 m/s to 2.38 m/s. In this scenario, the hull is free to heave and pitch with all other rigid body motions are fixed. The geometry contained the bare hull and the rudder as an appendage. The computation setup for the calm-water resistance is given in Table 4.2.

Table 4.2: Towing conditions for the KCS hull in calm-water.

Parameters	**Case**					
	1	**2**	**3**	**4**	**5**	**6**
Speeds (m/s)	0.915	1.281	1.647	1.922	2.196	2.379
Froude Number (Fr)	0.108	0.152	0.195	0.227	0.260	0.282
Reynolds Number (Re)	5.23×10^6	7.33×10^6	9.42×10^6	1.10×10^7	1.26×10^7	1.36×10^7

For seakeeping simulations, the full scale geometry is scaled by 1/37.879 to conduct validations under regular waves in head seas. The model is towed at 2.017 m/s to reach the service Froude number. The model is free to heave and pitch, while all other rigid body motion are restricted. The wave steepness $\left(\frac{H}{L}\right)$ was fixed at 1/60 in all cases, in which the water depth is established to be infinite. The wave conditions are represented in Table 4.3. In the present validation study, the regular waves were modeled with 5^{th} order Stokes wave theory.

Table 4.3: Regular head wave conditions for the KCS seakeeping computations.

Parameter	**Case**				
	1	**2**	**3**	**4**	**5**
Wave length: L	3.949	5.164	6.979	8.321	11.840
Wave height: H	0.062	0.078	0.123	0.149	0.196
Wave Steepness: H/L	0.016	0.015	0.018	0.017	0.016
L/L_{PP}	0.650	0.850	1.150	1.370	1.950

4.2 MESH GENERATION

A rectangular prism-shaped computational domain is built based on the ITTC recommendations for multiphase ship resistance and seakeeping simulations. The computational domain is built with a mirror plane since KCS model has a symmetric

mono-hull geometry. Preferentially, the hull is placed on the positive X-axis in which the movement impacts in the same direction and with gravitational force applied on the negative Z-axis. The domain size for resistance simulations with Froude number up to 1.0 can be determined in terms of length overall (L_{AO}) in Figure 4.2.

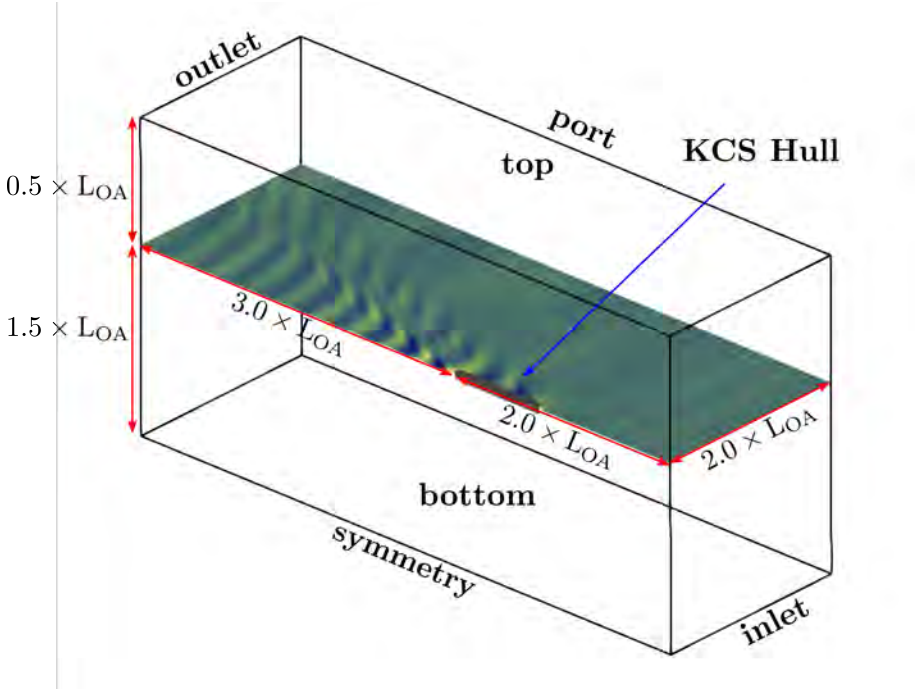

Figure 4.2: Computational domain for KCS Hull.

The inlet boundary is located $1.0 \times L_{OA}$ upstream of the hull to capture the bow wave and its effect on dynamic pressure on the hull. The outlet boundary is placed $3.0 \times L_{OA}$ downstream of the hull to prevent from wave reflection from the boundary. The height of the top exterior boundary is commonly $0.5 \times L_{OA}$ far away from the free surface. The exterior boundaries on the sides are placed $2.0 \times L_{OA}$ far away from the ship in order to capture the wake and minimize the impact of the location on numerical computations. The depth of the sea floor is taken distant enough from the free surface simulations in which the sea floor does not have considerable effects on the hull.

To conduct multiphase ship simulations, Numeca Hexpress is used to generate

mesh structure around KCS hull. Numeca Hexpress is a tool that used to generate non-conformal body fitted unstructured grids on the hull with high quality boundary layers. The domain discretization helps us define refinement levels that determine the number of divisions of the existing elements in half. Therefore, $\left(\frac{L_{OA}}{1000}\right)$ corresponds to 8 refinements of the initial mesh structure. In Hexpress, the mesh generation is applied in five steps; initial mesh generation, adaptation, snapping, optimization and viscous layer insertion. The first step of mesh generation process is generating an initial mesh encompasses the whole domain. The initial mesh corresponds to the isotropic subdivision of the computational domain in three dimensions that is chosen as a rectangular bounding box for multiphase ship simulations.

The initial block mesh should be generated as follows; 20 elements in longitudinal axis, 3-4 elements in lateral axis and 8-10 elements in vertical axis. In grid dependency studies, a systematical methodology is being followed by keeping the same refinement levels on the free surface and the vehicle. This methodology ensures the whole volume being refined systematically and not only the volume around the vehicle. Considering that the initial mesh contains N number of cells in each direction (X, Y, Z), the initial number of cells for various grid levels can be established in terms of N_{medium}: for coarse mesh the initial number of cells defined by $N_{coarse} = 0.75 \times N_{medium}$, for fine mesh the initial number of cells defined by $N_{fine} = 1.25 \times N_{medium}$. In Hexpress, the initial number of cells should be an integer. Therefore, it is not possible to keep a constant refinement ratio, as it can be set with structured grids.

The second step is adapting the mesh by subdividing the cells to the extent that specified geometrical criteria based on the refinement levels are satisfied. There are three criteria available; curve, surface, and volume. For the curve and surface criteria, cells that intersect with the solid body are considered refinement candidates. These candidates are subjected to proximity test between curves and surfaces, curvature measurement, and specification of target cell sizes on the solid body's curves and

surfaces. For the volume criterion, cells intersecting or located inside a substantial three-dimensional volume are marked to refine the cell size larger than the prescribed target size.

Anisotropic mesh refinement algorithm depends on the cell's orientation in Cartesian coordinates when surface or volume criteria are applied with target cell size. Since the initial mesh is oriented on the Cartesian coordinate system, cell refinement is applied by comparing the initial cell size and the target cell size. For the surface refinement criterion, the target sizes are computed on the surface with two surface tangent and normal vectors. These target sizes are mapped and compared to the actual cell size to apply the cell's appropriate refinement level. In practice, cells oriented parallel to the surfaces of the solid body may be refined anisotropically. A cell oriented with 45 degrees between the tangent of the surface and principal axis never is refined.

For resistance and seakeeping simulations, the anisotropic refinements are applied on the free surface and on KCS Hull. It is applied 4 refinements on the deck, 6 refinements on the side ship walls, 8 refinements on the bow, shaft and transom, 10 refinements on the rudder. The free surface is located at z = 0.3418 m for model 1 and z = 0.2850 m for model 2 which cover the entire computational domain. Mesh refinement normal to the free surface is set to $\left(\frac{L_{OA}}{500}\right)$ with aspect ratio of 20 and a local diffusion of 4 to ensure the free surface capturing for both models. For grid dependency studies, diffusion is adapted for each grid level; 2 diffusion levels for coarse, 3 levels for medium, 4 levels for fine and 5 levels for the extra fine mesh. For coarse mesh, the diffusion is reduced to 3 for the free surface.

Furthermore, to capture the wave system in the downstream of the hull in its respective Kelvin angle, an additional refinement sector is generated. This wave refinement sector is shown in Figure 4.3. The target cell size in normal direction of the free surface is set to $\left(\frac{L_{OA}}{1000}\right)$ with aspect ratio 8. The ship wave length can be

computed by

$$\lambda_{ship} = 2\pi Fr^2 L_{OA} \tag{4.1}$$

and the Kelvin angle can be approximated by a piecewise equation as follows:

$$\alpha = \begin{cases} Fr \leq 0.5 & 20^\circ \\ Fr > 0.5 & \tan^{-1}\left(\frac{\sqrt{2\pi Fr^2 - 1}}{4\pi Fr^2 - 1}\right) \end{cases} \tag{4.2}$$

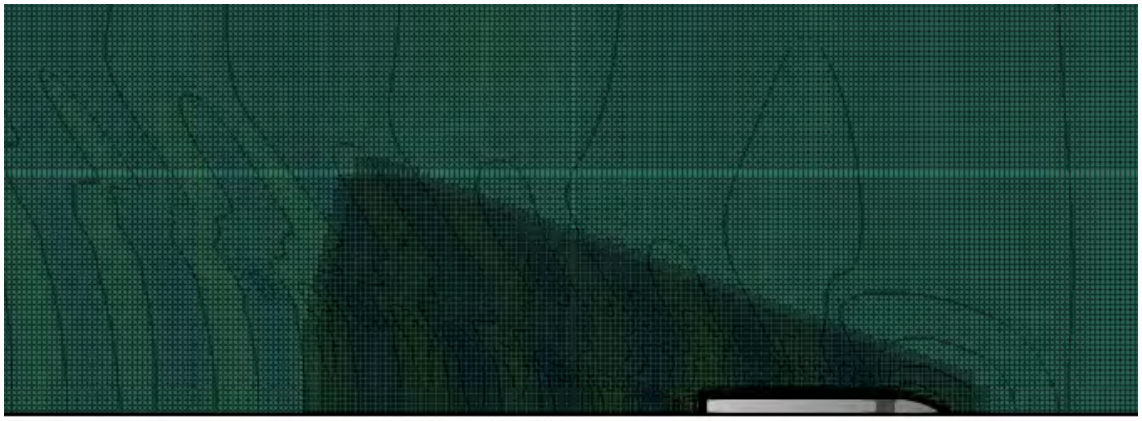

Figure 4.3: Wave refinement region on the free surface.

After the generation of refined mesh, the mesh was snapped to the boundaries involved in the computational domain. The goal of snapping is to project the adapted mesh on the surface to obtain a good quality body conforming mesh. This operation includes advanced algorithms for geometrical features such as corners and curves in the mesh. These algorithms ensure that, when the mesh is projected onto the solid body, a mesh vertex is attached to each corner of the body and that a path of mesh edges is attached to the curve. However, the snapping of the mesh onto a body can generate distorted elements. Finally, the mesh is smoothed by moving points on the surface and in the volume to provide a mesh with a good but not guaranteed quality.

After snapping action, the mesh can involve poor quality cells usually located at the corners and curves. Some of these cells may be concave, twisted or may even

have a negative volume. Twisted cells generally have distorted shapes. Besides concave cells look like boomerang which one of the tetrahedrons has a negative volume. Therefore, convex cells are significant to ensure stability and robustness of the numerical computation. However, adaptation of concave cells can cause negative cells in the computational domain. The presence of negative cells is a sign of inadequate cell sizes in a complex region. Nevertheless, further mesh refinements solve the problem. Optimization stage removes of all the concave, twisted and negative cells in the mesh and transform them to convex hexahedra cells.

High Reynolds number flows contain strong gradients on the walls and in free shear layers that requires high resolution of the computation across the shear layers and normal to the boundary layer. Therefore, a very specific approach of anisotropic mesh refinement is required in the critical regions to capture the strong gradients. Anisotropic mesh refinement is based on successive subdivisions of the cells connected to the walls. Additionally, this technique is computationally cost-effective and robust. Here, the viscous layers are inflated from the surface based in inflation factor and first layer thickness. The first layer thickness can be defined in terms of reference length (L_{ref}), kinematic viscosity (ν) and target non-dimensional wall distance (y^+). The relation between width of the first cell on the wall y_{wall} and the non- dimensional wall distance (y^+), can be obtained by using Blasius equation:

$$y_{wall} = 6 \left(\frac{U_{ref}}{\nu} \right)^{-\frac{7}{8}} \left(\frac{L_{ref}}{2} \right)^{\frac{1}{8}} y_1^+ \cdots \tag{4.3}$$

where (U_{ref}) is the reference velocity. The non-dimensional wall distance value (y^+) can be estimated by:

$$y^+ = \max \left(y^+_{min}, \min \left(30 + \frac{(Re - 10^6) \times 270}{10^9}, y^+_{max} \right) \right) \tag{4.4}$$

where $y^+_{min} = 50$ and $y^+_{max} = 300$. For the numerical computations, the length overall of the hull is considered as reference length (L_{ref}), while the maximum advance speed

is chosen for the reference velocity (U_{ref}). The wall functions are used to model the boundary layer.

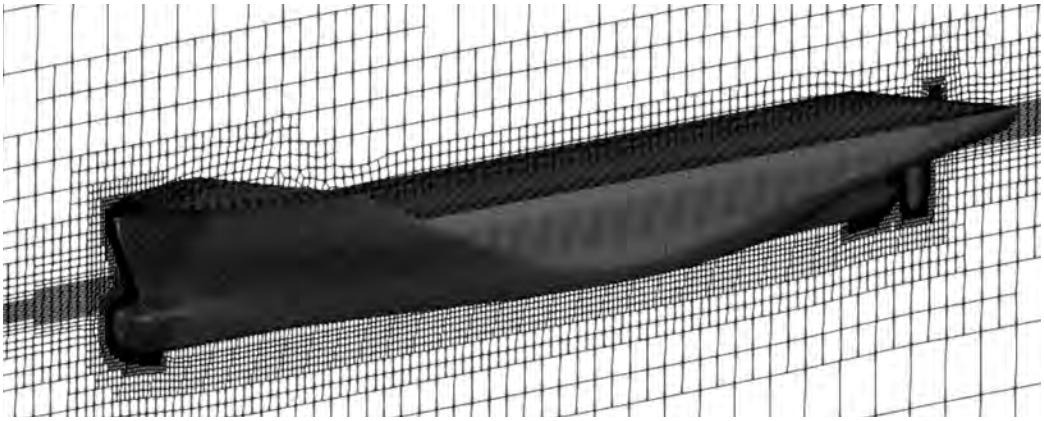

(a) Coarse mesh.

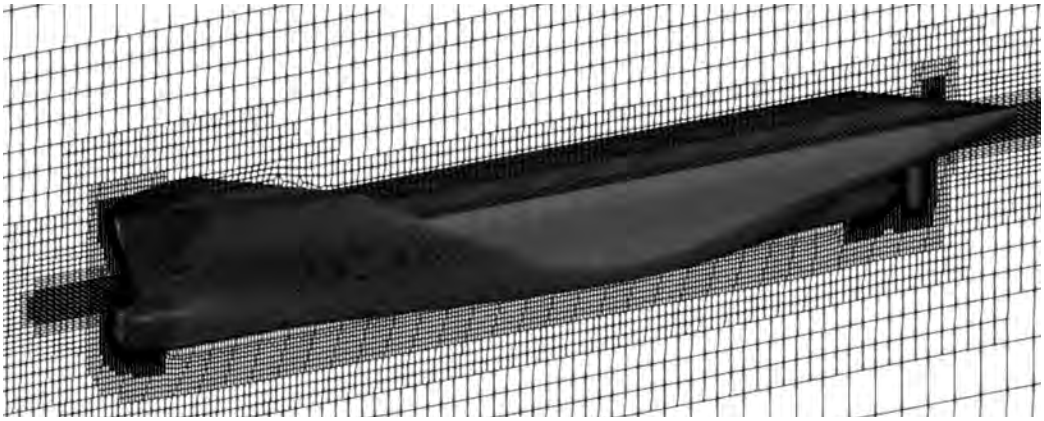

(b) Medium mesh.

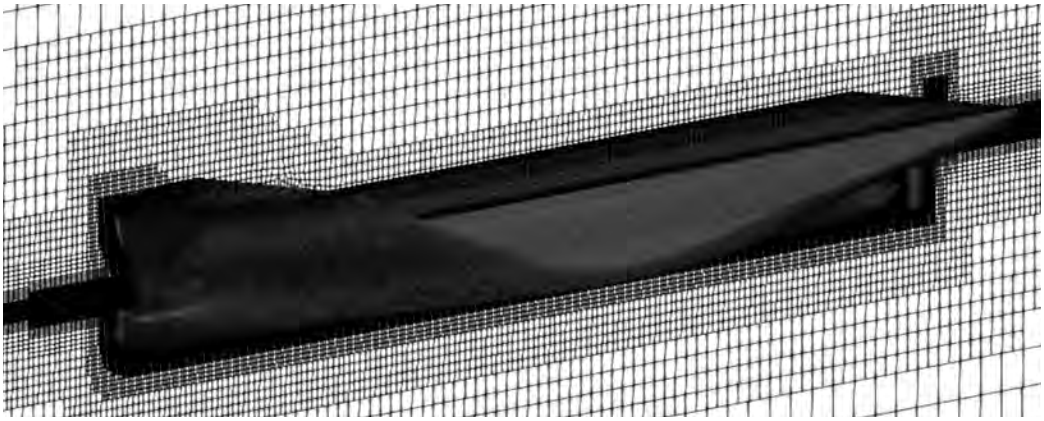

(c) Fine mesh.

Figure 4.4: Various grid refinement levels around KCS hull.

Table 4.4: Mesh quality metrics for grid dependency studies of calm-water resistance simulations.

Mesh Characteristics	**Coarse**	**Medium**	**Fine**
Number of cells	1667834	3500672	6968592
Maximum non-orthogonality	75.9638	70.5288	71.1487
Maximum skewness	3.6961	3.2335	3.6817
Maximum aspect ratio	45.4962	34.4385	35.1914

4.3 COMPUTATION SETUP

4.3.1 Physics Modeling

The RANS-VoF solver *interFoam* is used to simulate multiphase flow around the ship, that employs a Finite Volume Method (FVM) to discretize the Navier Stokes equations. Continuity and momentum equations are coupled via predictor-corrector scheme, in which details are discussed in Section 3.5. Time-derivative terms were discretized using first-order implicit scheme, which is bounded and stable for industrial applications. The convective terms were discretized by a total variation diminishing (TVD) second order accurate, bounded scheme with van Leer limiter [82]. The diffusion terms were discretized via central differencing schemes. To capture the free-surface, higher order interface capturing scheme was used, which is a combination of upwind and downwind schemes. The pressure-velocity coupling and solution procedure was based on PIMPLE algorithm [83], that is a combination of SIMPLE [75] and PISO algorithms [76].

As mentioned in Section 3.4, the selection of turbulence model is crucial in modeling High-Reynold number flows. Therefore, we used $k-\omega$ SST turbulence model, in which showed accurate predictions in resolving boundary layer. Particularly, the non-dimensional wall distance (y^+) needs to be lower than 1, since the accuracy of

the computation resolutely depends on the (y^+) value. In this study, SST $k-\omega$ turbulence model [84] with wall functions [27] to resolve the boundary layer.

The dynamic trim and sinkage of the ship is modeled using *rigidBodyMotion* model, in which only heave and pitch motions are allowed.

4.3.2 Time Step Selection

The Courant-Friedrichs-Lewy (CFL) number (Co) is a stability condition, that defines the appropriate time step, where the properties of the fluid are guaranteed to be solved at each grid point while the flow is moving through a discrete spatial grid. Therefore, CFL condition must be satisfied to ensure stability. For calm-water resistance simulations, the time step should be $\left(\Delta t = 0.005 \sim 0.01 \frac{L_{ref}}{U_{ref}}\right)$, where ($L_{ref}$) corresponds to the length between perpendiculars of the ship (L_{PP}) and (U_{ref}) is the ship advance speed, respectively.

For regular wave conditions, the time step Δt must be at least $T/60$ for short waves, and $T/100$ for regular waves, in which T is the wave period in seconds [85].

4.3.3 Boundary Conditions

Boundary conditions are mathematical expressions that apply new constraints to the physical problem on specific boundaries. These conditions must be appropriately defined for the problem to provide a stable and accurate numerical solution. Pressure, velocity, and volume fraction fields are imposed as Dirichlet boundary conditions at the inlet that mimics free flow. For far-field conditions, one can define a symmetry boundary condition if the boundary is far from the ship. However, the ship and its motions will be significantly affected if the computational domain boundaries are close to the ship. Under this circumstance, Neumann boundary conditions would be more desirable. For outlet, it is crucial to define a special condition that prevents reflection and applies radiation. Bottom patch can be treated as no-slip wall.

In OpenFOAM®, the boundaries should be treated based on the physical problem as well. At the inlet, *fixedValue* boundary condition is applied for velocity that sets the velocity field to a constant value. *fixedFluxPressure* boundary condition is defined for the pressure field at the inlet that adjusts the pressure gradient based on the velocity boundary condition. The volume fraction is also set to a constant value by using *fixedValue*. For outlet, the *outletPhaseMeanVelocity* boundary condition is applied that adjusts the velocity for each phase to reach the mean value. The *zeroGradient* boundary condition is set at the outlet to extrapolate the pressure quantity from the nearest cell value for the pressure field. For the velocity field, *variableHeightFlowRateInletVelocity* is applied that provides a velocity boundary condition for free-surface flow based on an end-user volumetric flow rate. Here, the flow-rate is computed proportional to the volume fraction at each face of cells on the patch. Additionally, the volume fraction is ensured to be limited between 0 and 1. The boundary conditions specified for calm-water resistance simulations are given in Table 4.5.

Table 4.5: Boundary conditions for calm-water resistance simulations.

Boundary	**Pressure**	**Velocity**	**Volume Fraction**	**Turbulent Quantities**
inlet	fixedFluxPressure	fixedValue	fixedValue	fixedValue
outlet	zeroGradient	outletPhaseMeanVelocity	variableHeightFlowRate	inletOutlet
top	totalPressure	pressureInletOutletVelocity	inletOutlet	inletOutlet
bottom	symmetryPlane	symmetryPlane	symmetryPlane	symmetryPlane
sides	symmetryPlane	symmetryPlane	symmetryPlane	symmetryPlane
hull	fixedFluxPressure	fixedValue	zeroGradient	wallFunction

For seakeeping simulations, *waveVelocity* boundary condition is applied, that provides a velocity boundary condition specified by the superposition of wave models. The volume fraction and pressure boundary conditions are affected by this condition. In the case of velocity oscillation gradually increases compared to the mean flow, flow reversal occurs. To avoid this unstability, *fixedFluxPressure* pressure boundary condition is applied. For volume fraction, *waveAlpha* boundary condition is applied,

in which this boundary condition sets the volume fraction value to that specified by a superposition of wave models. The boundary conditions for seakepping simulations are provided in Table 4.6.

Table 4.6: Boundary conditions for seakeeping simulations.

Boundary	**Pressure**	**Velocity**	**Volume Fraction**	**Turbulent Quantities**
inlet	fixedFluxPressure	waveVelocity	waveAlpha	fixedValue
outlet	zeroGradient	outletPhaseMeanVelocity	variableHeightFlowRate	inletOutlet
top	totalPressure	pressureInletOutletVelocity	inletOutlet	inletOutlet
bottom	symmetryPlane	symmetryPlane	symmetryPlane	symmetryPlane
sides	symmetryPlane	symmetryPlane	symmetryPlane	symmetryPlane
hull	fixedFluxPressure	fixedValue	zeroGradient	wallFunction

4.4 RESULTS AND DISCUSSION

This section presents the results of convergence analysis of the the numerical computations, while the following section presents the application of the methods for RANS-VoF simulation of a ship in calm water and head-seas. Following this, the same procedure was applied on the catamaran model of interest.

4.4.1 Calm Water Resistance Simulations

In this section, calm-water resistance simulations around KCS hull are conducted considering the conditions given in Table 4.2. A negative value of trim and sinkage corresponds to the position, in which the bow of the ship is inclined downward. Here the total resistance coefficient (C_T) is calculated by,

$$C_T = \frac{2R_T}{\rho S U_{ref}^2} \tag{4.5}$$

where, (R_T) is the total resistance, (ρ) is the density of water, (S) is the wetted surface area and (U_{ref}) is the reference velocity. The trim angle is calculated by the

vertical distance change at the bow (Δt_b) and the stern (Δt_s) with respect to position in still-water.

$$\theta = \tan^{-1}\left(\frac{2\left|\Delta t_b + \Delta t_s\right|}{L_{PP}}\right) \tag{4.6}$$

Numerical uncertainty of the total resistance coefficient is assessed for three various types of grids. As listed in Table 4.4, three types of grid size, i.e., coarse, medium and fine grids are considered. To carry out grid dependency analysis, all towing conditions are established as given in Table 4.2.

Figure 4.5 illustrates the influence of mesh refinement levels on the hydrodynamic performance of KCS hull. The experimental data are obtained from the model experiment with KCS provided by Tokyo 2015 Workshop. Figure 4.5a shows the effect of grid refinement levels on the total resistance coefficient. The total resistance coefficients follow the same trend in all three refinement levels. However, as the mesh refinement level increases, the total resistance curve approaches closer to the experimental data. In Figure 4.5b, the change in dynamic trim is presented in terms of increasing speed and three grid refinement levels. The computational results show higher consistency in trim with the experimental data. Figure 4.5c shows the vertical change on the location of center of gravity. It is observed that, the maximum error is observed in the heave motion. Since the change is very small, the error seems higher. In fact, the change in vertical position is approximately 0.6 mm. In this case, the amount of error in heave motion is quite acceptable.

Figure 4.6, wave elevation contour graphs are provided. It is observed that, the Kelvin wave angle rises as the Froude number gradually increases. Additionally, the variation between crests and troughs due to bow generated wave system gradually increases.

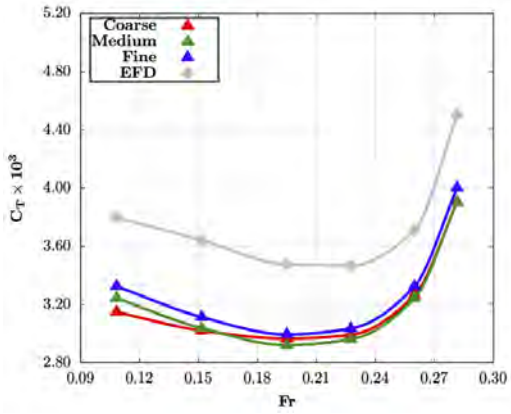

(a) Total resistance coefficient.

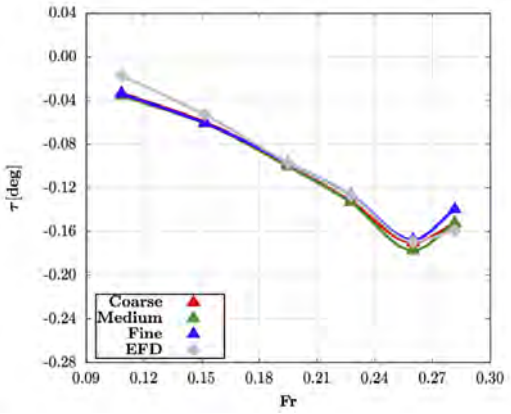

(b) Trim.

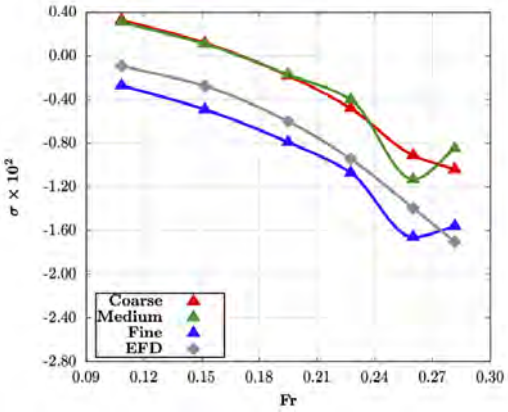

(c) Sinkage.

Figure 4.5: Grid dependency analysis at different Froude numbers.

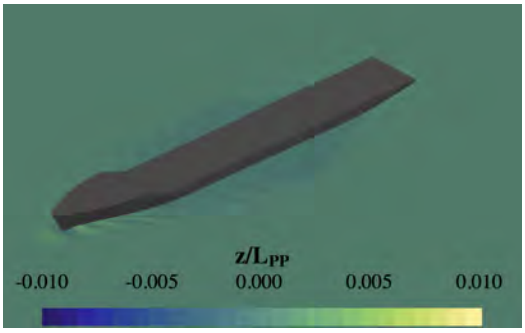

(a) Fr = 0.108

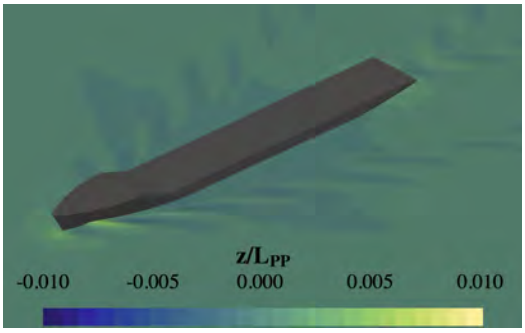

(b) Fr = 0.152

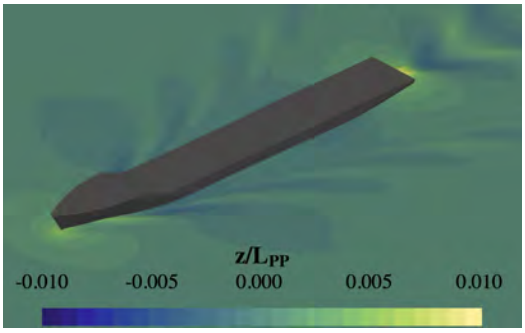

(c) Fr = 0.195

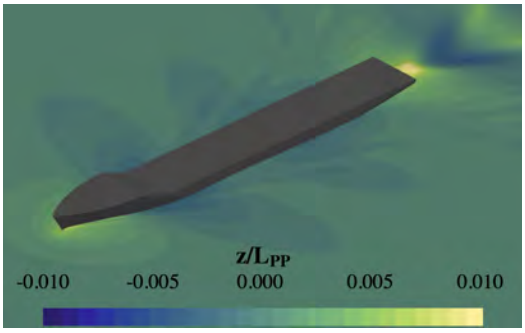

(d) Fr = 0.227

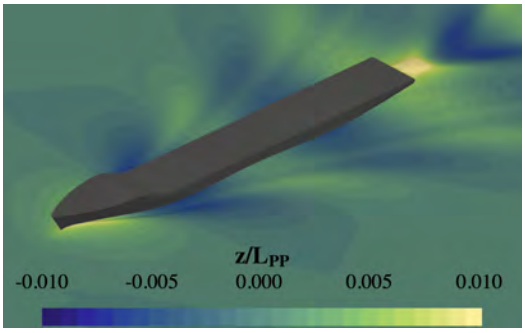

(e) Fr = 0.260

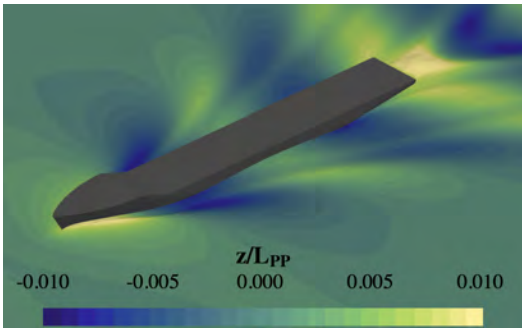

(f) Fr = 0.282

Figure 4.6: Free surface wave elevation around KCS at different Froude numbers.

4.4.2 Seakeeping Analysis in Regular Waves

The seakeeping analysis of KCS hull consist of five head-wave computations with various wavelength (λ) and wave height (H) sequences. All wave conditions have approximately wave steepness of $k\zeta = 0.05$. The model-scale hull is accelerated from rest to 2.017 m/s allowing heave and pitch motions. Instantaneous free-surface wave elevation contour graphs for the calm-water resistance and seakeeping computations are illustrated in Figure 4.8.

The total resistance and seakeeping analysis are conducted based on Fourier series reconstruction to evaluate the harmonics of the resultant signals. The reconstructed Fourier time series $r\,(t)$ take the following form:

$$r\,(t) = \frac{r_0}{2} + \sum_{n=1}^{N} r_n \cos\left(n\omega_e t + \gamma_n\right) \tag{4.7}$$

in which r_n is the amplitude of n^{th} harmonic and γ_n is the phase lag originated from the incident wave crest positioned at the bow at initial time. The 0^{th} harmonic corresponds to the mean value of the signal and the higher harmonics are calculated by using:

$$\begin{aligned} a_n &= \frac{2}{T_e}\int_0^{T_e} r\,(t)\cos\left(n\omega_e t\right)\mathrm{d}t \quad (n = 1, 2, 3, ...) \\ b_n &= \frac{2}{T_e}\int_0^{T_e} r\,(t)\sin\left(n\omega_e t\right)\mathrm{d}t \quad (n = 1, 2, 3, ...) \end{aligned} \tag{4.8}$$

The corresponding amplitudes and phase lags are derived from:

$$\begin{aligned} r_n &= \sqrt{a_n^2 + b_n^2} \\ \gamma_n &= \tan^{-1}\left(-\frac{b_n}{a_n}\right) \end{aligned} \tag{4.9}$$

In this analysis, ω_e is the encounter frequency of the wave and T_e is the encounter period of the wave. To calculate the encounter frequency (ω_e), supposing the ship velocity is denoted by V_s, the encounter velocity of the ship with respect to the waves

can be computed in terms of encounter angle β and wave speed V_w:

$$V_e = V_w - V_s \cos\beta \tag{4.10}$$

Hence, the wave encounter frequency (ω_e), satisfies

$$\omega_e = \omega \left(1 - V_s \frac{\omega}{g} \cos\beta\right) \tag{4.11}$$

This situation is represented in Figure 4.7.

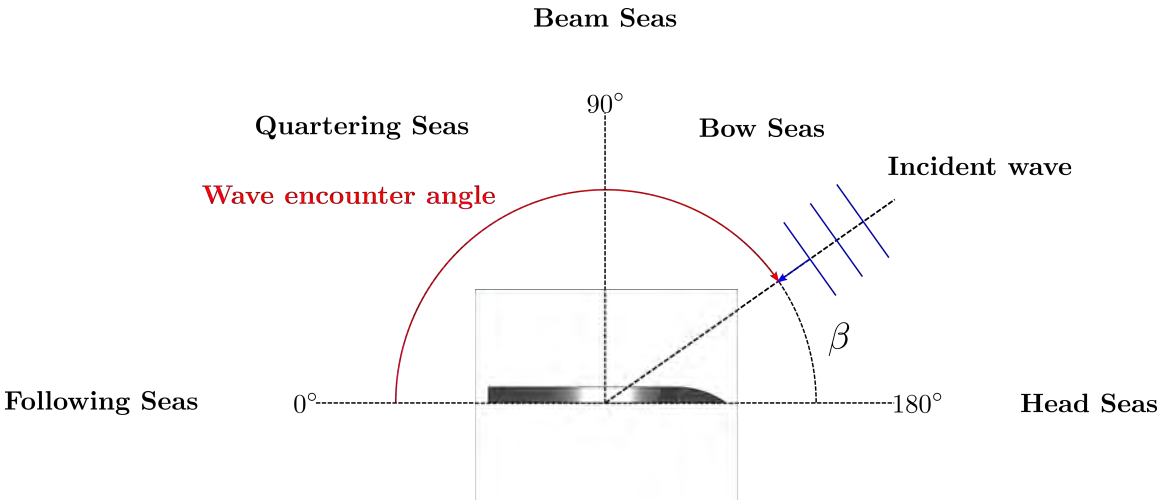

Figure 4.7: Wave encounter angle.

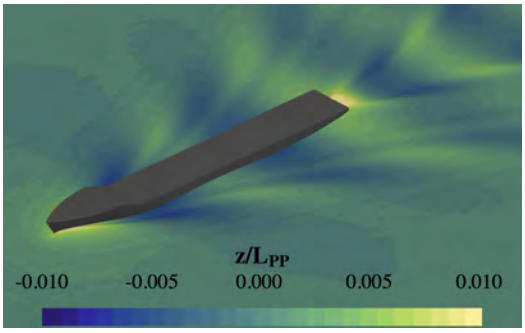

(a) Calm water.

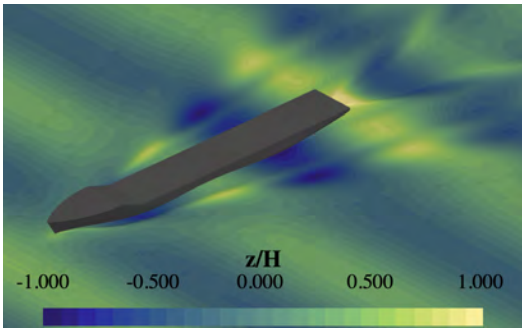

(b) $\lambda/\mathrm{L_{PP}} = 0.650$

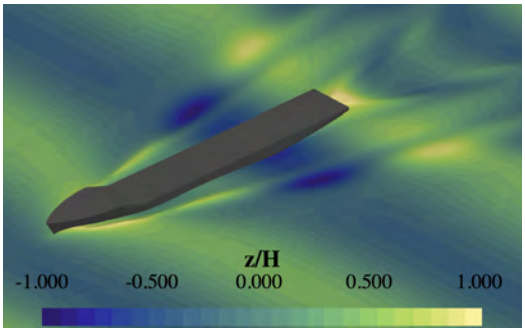

(c) $\lambda/\mathrm{L_{PP}} = 0.850$

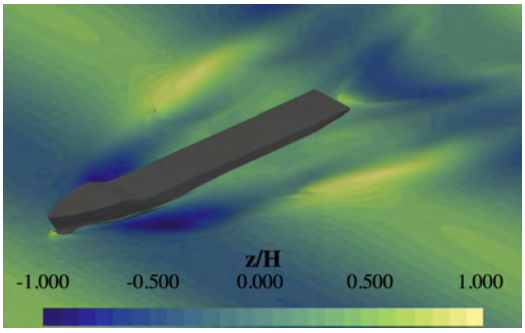

(d) $\lambda/\mathrm{L_{PP}} = 1.150$

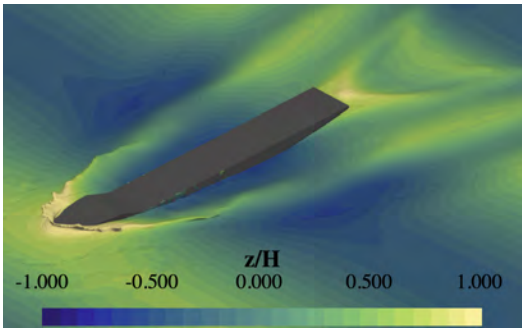

(e) $\lambda/\mathrm{L_{PP}} = 1.370$

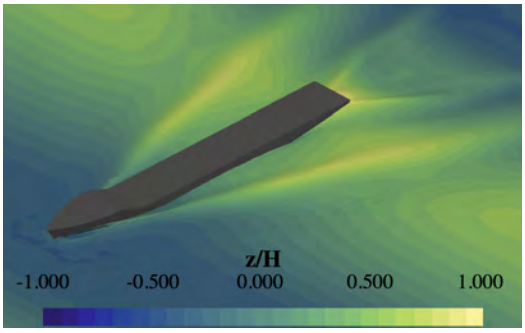

(f) $\lambda/\mathrm{L_{PP}} = 1.950$

Figure 4.8: Instantaneous free surface wave elevations.

The summary of the predicted and experimental results for seakeeping analyzes are shown in Table 4.7. The table includes the total resistance coefficient (C_T), normalized heave (z/ζ) and pitch angle ($\theta/k\zeta$).

The total resistance coefficient is accurately predicted with the largest error of 8.64%. This error corresponds to approximately 10 N discrepancy with the experimental results. the predicted resistance is within 10% for all cases. However, the error in heave and pitch motions are much larger than total resistance coefficient, since the absolute values are smaller. The mean heave is predicted to the value within 20%, where the largest error is found in Case 4 by approximately 4 mm. The largest error for mean pitch is found to be at Case 3, due to the resonance issues reported [86].

Table 4.7: Results of the seakeeping simulations in regular-head waves.

Parameters		**Case**				
		1	**2**	**3**	**4**	**5**
$C_T \times 10^3$	CFD	8.154	8.572	15.118	15.160	11.606
	EFD	8.253	9.244	14.157	13.955	10.842
	E%D	1.20%	7.27%	-6.79%	-8.64%	7.05%
z/ζ	CFD	-0.753	-0.546	-0.238	-0.204	-0.193
	EFD	-0.809	-0.628	-0.278	-0.249	-0.201
	E%D	6.94%	13.06%	14.45%	18.12%	3.74%
$\theta/k\zeta$	CFD	-0.1063	-0.1154	-0.0016	-0.0048	-0.056
	EFD	-0.1078	-0.1303	-0.0026	-0.0068	-0.057
	E%D	1.39%	11.42%	38.46%	30.47%	-1.17%

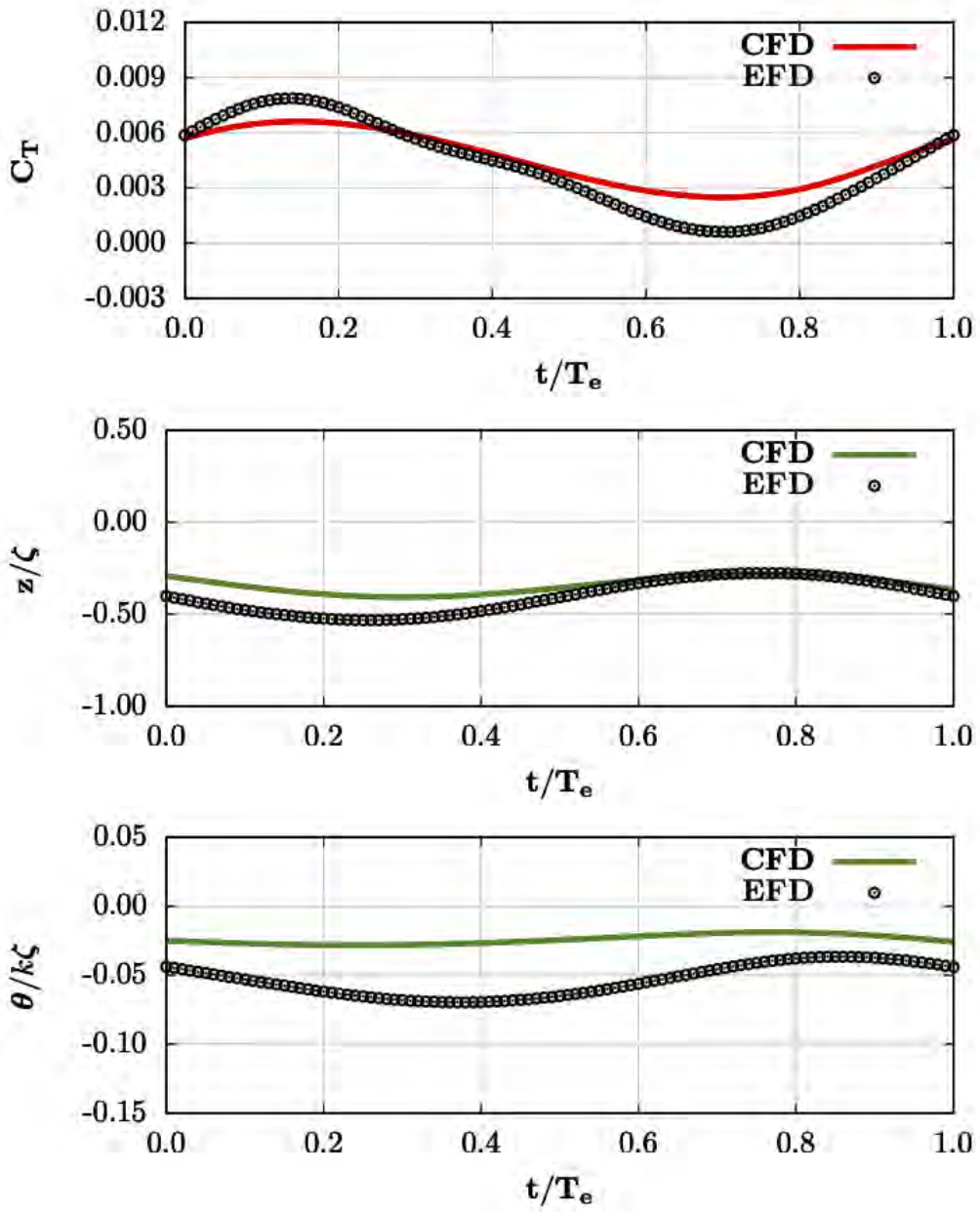

Figure 4.9: Time histories of drag coefficient, heave and pitch angle for Case 1.

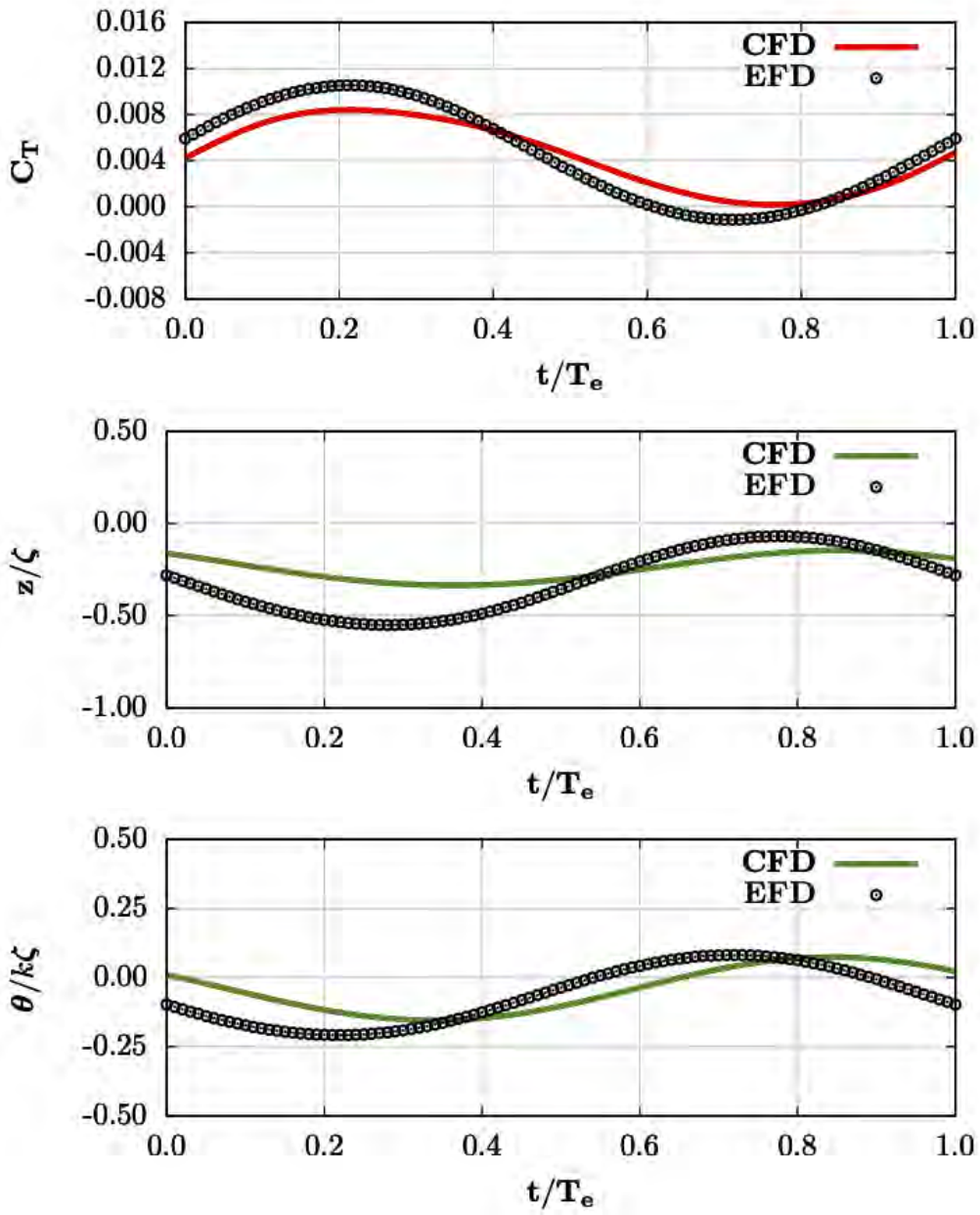

Figure 4.10: Time histories of drag coefficient, heave and pitch angle for Case 2.

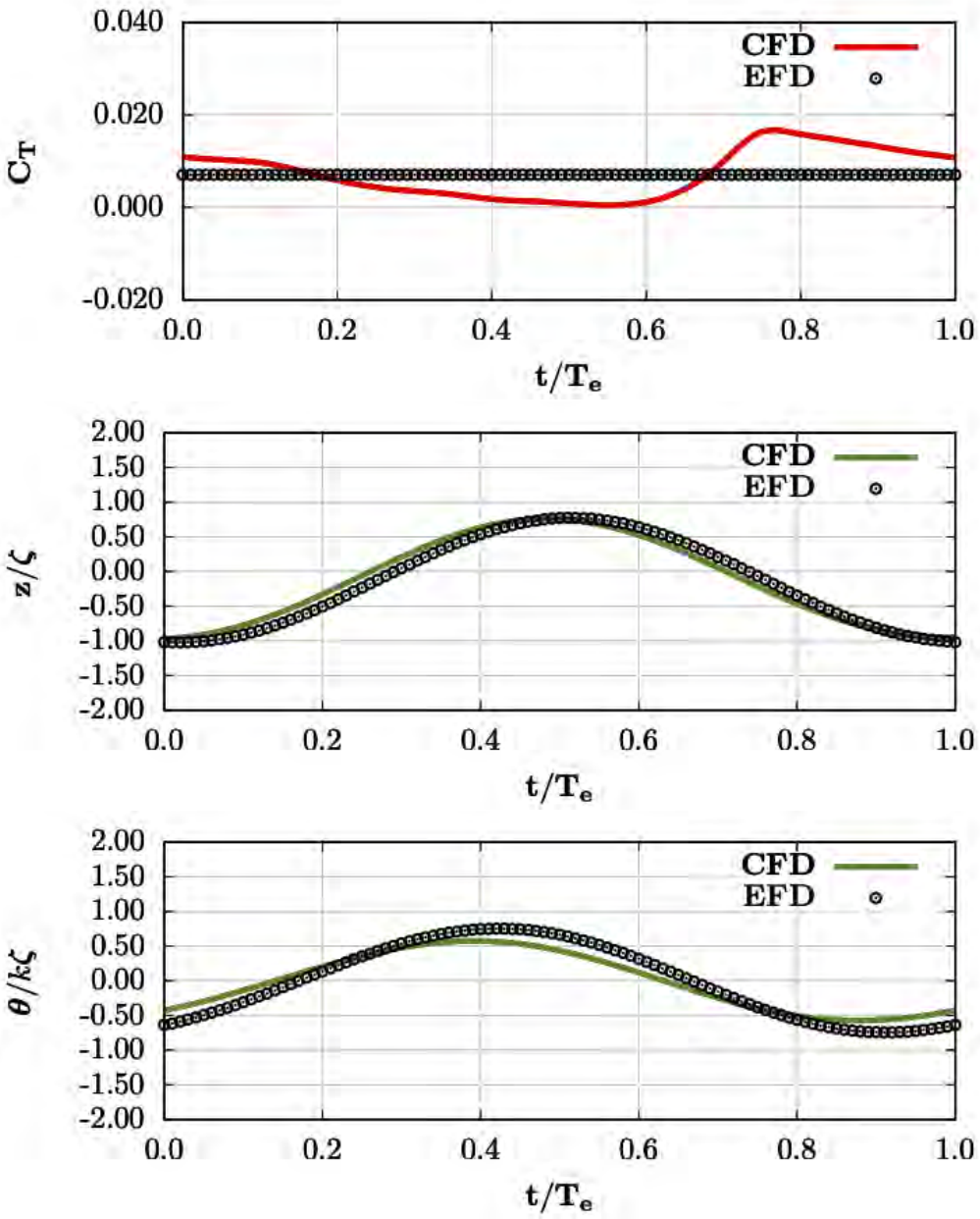

Figure 4.11: Time histories of drag coefficient, heave and pitch angle for Case 3.

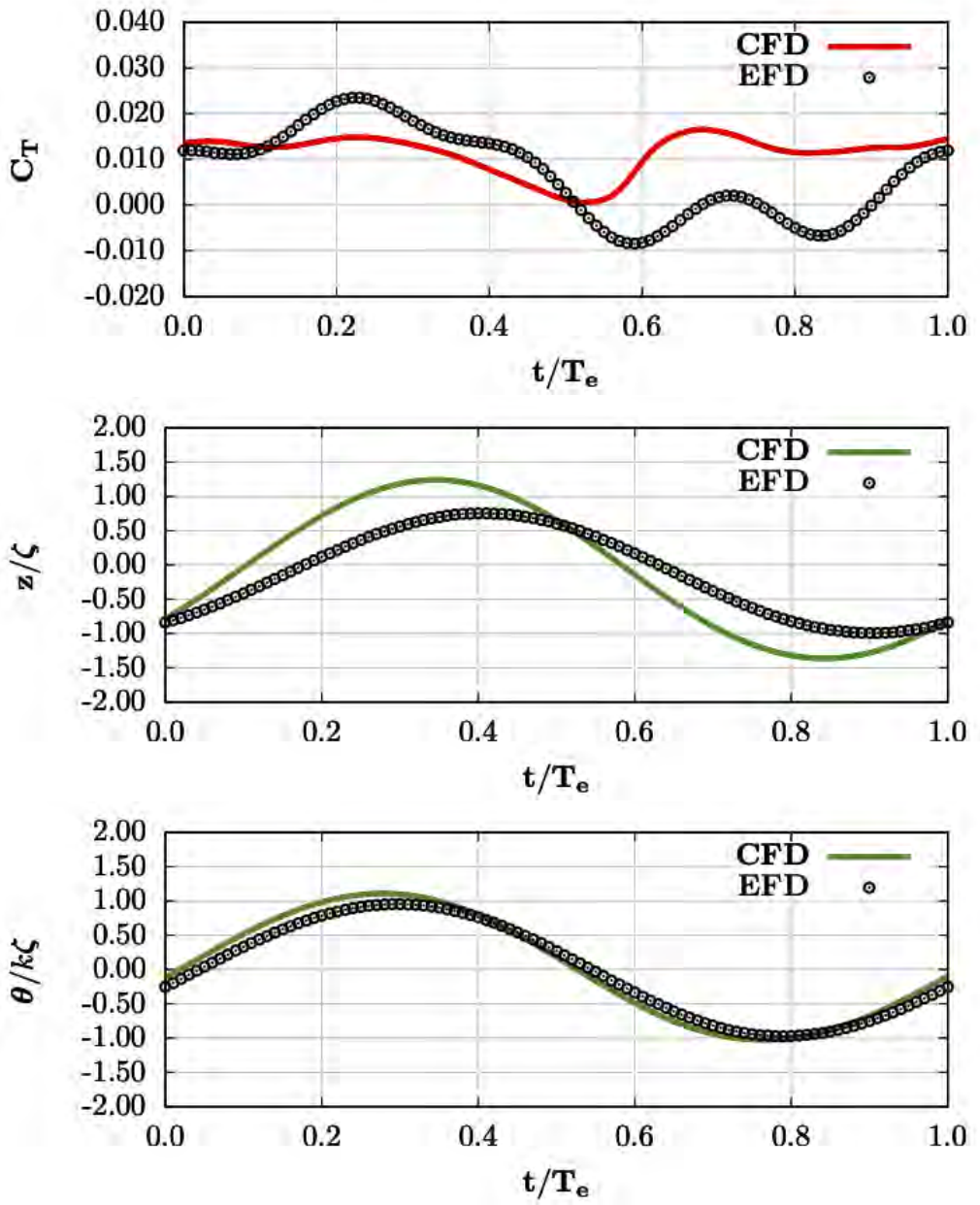

Figure 4.12: Time histories of drag coefficient, heave and pitch angle for Case 4.

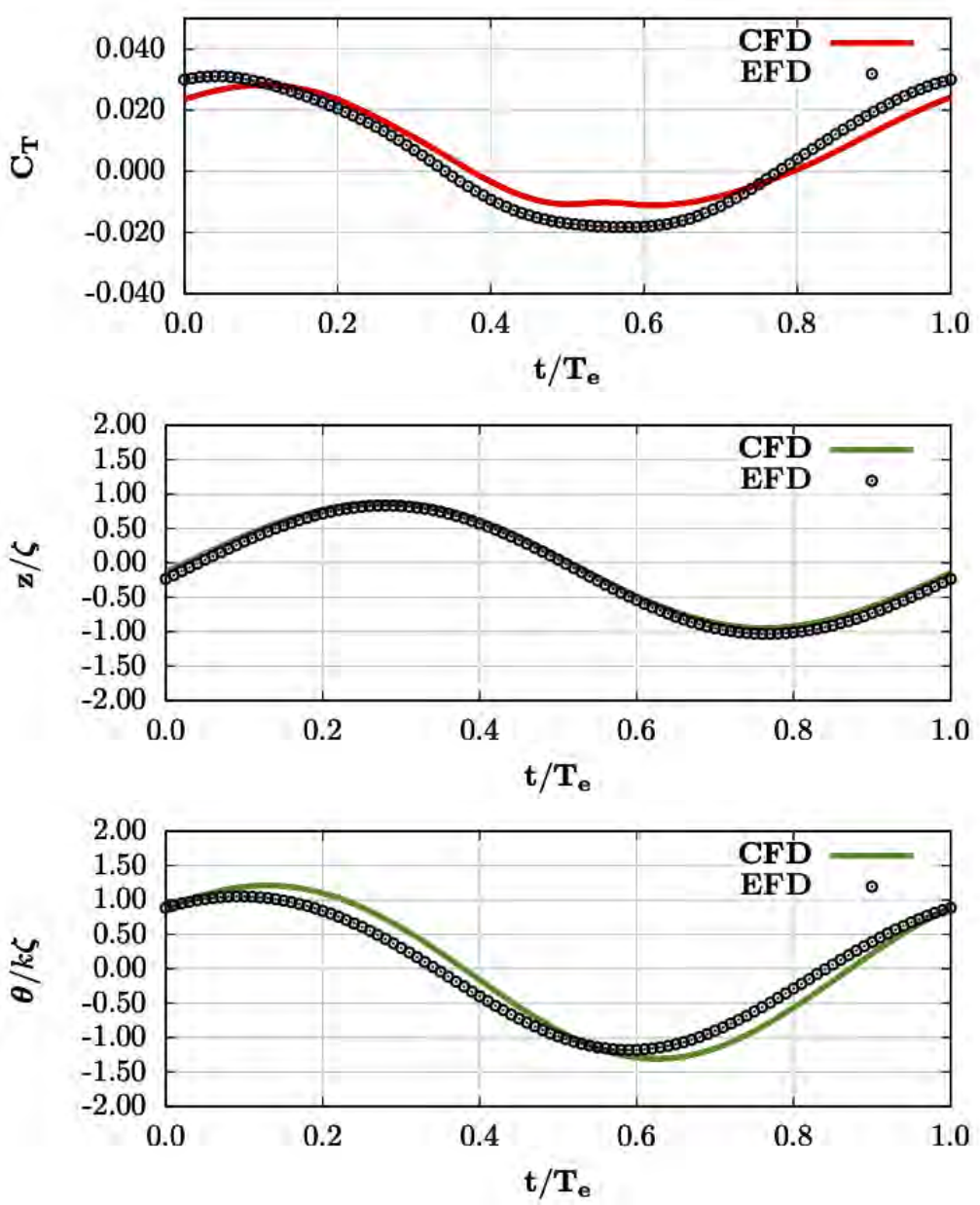

Figure 4.13: Time histories of drag coefficient, heave and pitch angle for Case 5.

CHAPTER 5
HYDRODYNAMIC PERFORMANCE PREDICTION OF THE CATAMARAN IN CALM WATER

In this chapter, the hydrodynamic performance of a catamaran of interest is analyzed through a parametric study in different water depths. The validated approach in Chapter 3 is applied on the vehicle to discuss the shallow water effects on the resistance, trim and sinkage, respectively.

5.1 GEOMETRY AND TEST CONDITIONS

To investigate the performance of a catamaran in limited water depths, WAM-V 16 USV model of interest is selected. The geometry includes the pontoons, suspension and articulation systems and the payload tray, as shown in Figure 5.1. The main particulars of WAM-V 16 is given in Table 5.1.

Figure 5.1: WAM-V 16 USV CAD model.

Table 5.1: Main particulars of WAM-V 16.

Main Particulars	**Symbol**	**Value**
Length overall	L_{OA} (m)	4.895
Length waterline	L_{WL} (m)	3.906
Breadth waterline	B_{WL} (m)	2.426
Breadth of the demihull	b (m)	0.432
Distance between center of demihulls	H_D (m)	1.994
Draft	T (m)	0.120
Depth waterline	D_{WL} (m)	0.211
Block Coefficient	C_B (-)	0.158
Displacement	Δ (kg)	324.2
Wetted Surface Area	S (m^2)	4.059
Vertical center of gravity	KG (m)	0.379
Longitudinal center of gravity	LCG (m)	1.528

The calm-water resistance simulations of WAM-V 16 model are carried at different advance speeds from 0.25 m/s to 5.00 m/s and different water depths from $h/L_{OA} = 0.25$ to $h/L_{OA} = 1.50$. Grid sensitivity analysis is carried out only at deep water conditions ($h/L_{OA} = 1.50$).

Table 5.2: Towing conditions for the WAM-V 16 in calm-water.

Depth / Length Ratio $\mathbf{h/L_{OA}}$ **(-)**	**Advance Speed** $\mathbf{U_{ref}}$ **(m/s)**	**Froude Number Fr (-)**	**Reynolds Number Re (-)**
0.25	0.25	0.040	8.576×10^5
	0.50	0.081	1.715×10^6
0.50	1.00	0.162	3.431×10^6
	1.50	0.242	5.146×10^6
0.75	2.00	0.323	6.861×10^6
	2.48	0.400	8.508×10^6
1.50	3.00	0.485	1.029×10^7
	4.00	0.646	1.372×10^7
	5.00	0.808	1.715×10^7

5.2 MESH GENERATION

In this section, the details of the mesh generation process are provided. To analyze the calm-water resistance prediction of the catamaran model, the computational domain is constructed following the ITTC recommendations [85]. Since the model is a multi-hull geometry, it is known that the interference between wave-generated systems will affect the pressure distribution on the demihulls [87]. Therefore, the computational domain is generated for the whole geometry, as shown in Figure 5.2. The computational domain has dimensions of $-3.0 \leq x/L_{OA} \leq 2.0$, $-2.0 \leq y/L_{OA} \leq 2.0$, $-1.5 \leq z/L_{OA} \leq 0.5$. The flow is considered to be in the direction of the negative x-axis, and the positive z-axis is taken to be in the upward direction. According to the coordinate system, the pitching motion is around y-axis, the heave motion is on z-axis.

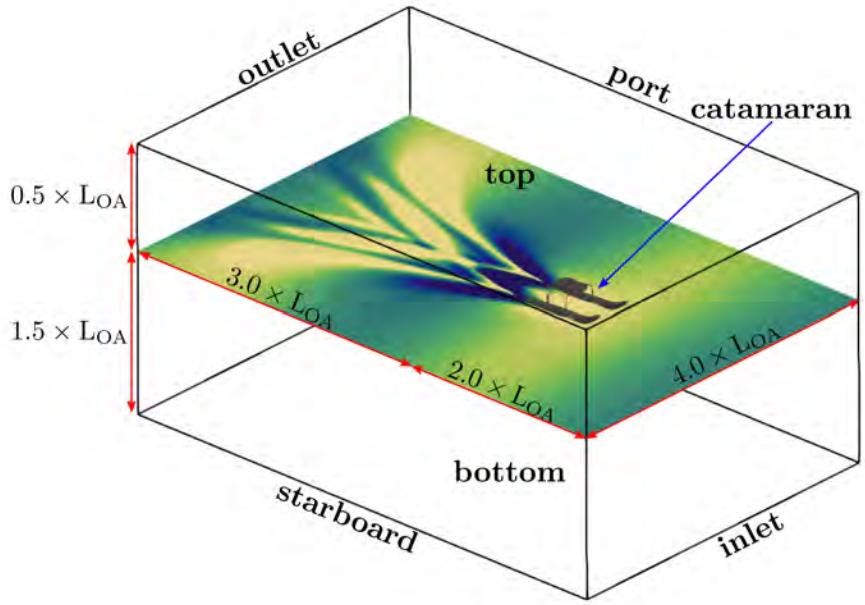

Figure 5.2: Computational domain for WAM-V 16 model.

To investigate the effects of different grid refinement levels on the catamaran performance, three different computational mesh generated around the catamaran. The mesh generation approach for grid sensitivity analysis applied in the validation studies are followed. The initial block mesh is generated as follows; 20 elements in longitudinal axis, 8 elements in lateral axis and 10 elements in vertical axis. The grid refinement levels are determined based on the initial number of cells, as discussed in Chapter 4. The mesh characteristics of the three computational grids are given in Table 5.3.

Table 5.3: Mesh characteristics used for grid dependency study.

Mesh Parameter	**Coarse**	**Medium**	**Fine**
Number of cells	4330275	10049175	16824510
Max. non-orthogonality	70.5288	74.8088	79.3803
Max. skewness	3.21634	3.15838	3.13912
Max. aspect ratio	94.0290	41.4609	32.0000

For calm-water resistance simulations, anisotropic mesh refinement levels are applied on the free surface and the vehicle, It is applied 6 refinements on the pontoons, 8 refinements on suspension system and 6 refinements on the payload tray. The free surface is located at z = 0.12 m. Mesh refinement normal to the free surface is set to $\left(\frac{L_{OA}}{500}\right)$ with aspect ratio of 20 and a local diffusion of 4. Furthermore, to capture the wave system in the downstream of the vehicle in its respective Kelvin angle, an additional refinement sector is generated by following the same approach discussed in Chapter 4. The target cell size in normal direction of the free surface is set to $\left(\frac{L_{OA}}{1000}\right)$ with aspect ratio 20.

To capture the viscous flow effects, the first cell distance to the wall is approximated by Blasius equation and applied to the vehicle, as the similar approach established in Chapter 4. In Figure 5.3 refinement regions and levels around the catamaran are illustrated. Figure 5.4 presents the free surface mesh refinements and Kelvin wave refinement regions around the catamaran model.

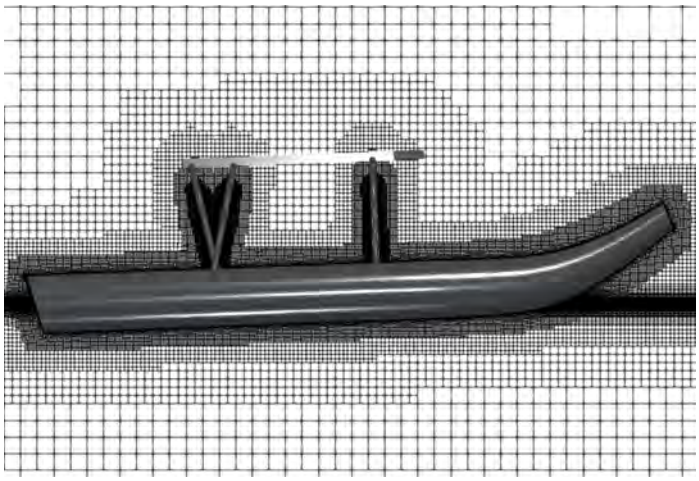

Figure 5.3: Mesh refinements around the catamaran model.

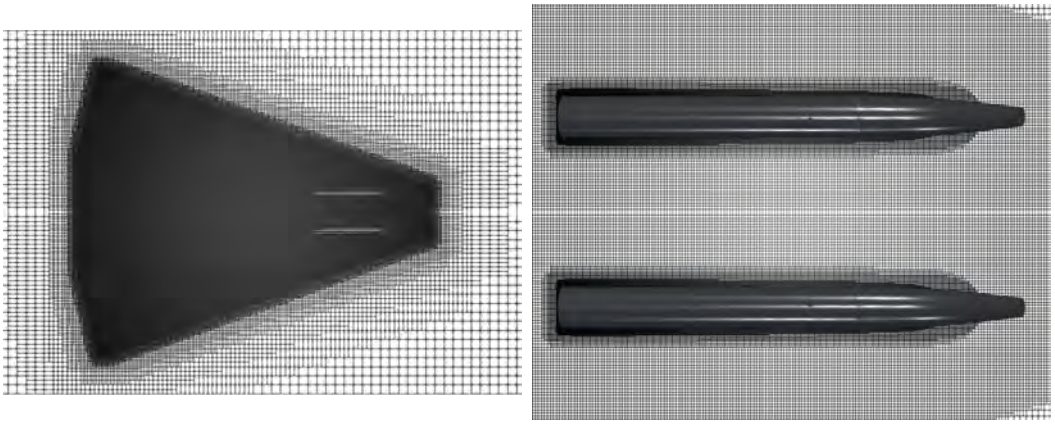

Figure 5.4: Free surface mesh refinement regions around the catamaran.

For varying water depth simulations, the bottom boundary is separated into two regions. The section between the upstream boundary and aft of the hull is constructed as the refinement region, where two refinement subregions with dimensions of length (L_{PP}) and width (B_{WL}) of the catamaran are applied to capture pressure gradients accurately. In this region, the boundary layers are generated with a target y^+_{target} value of 300 to capture the velocity gradients by avoiding substantial number of cells. The mesh characteristics for the numerical simulations for varying water depth conditions are given in Table 5.4.

Table 5.4: Mesh characteristics used for varying depth simulations.

Mesh Parameter	$\mathbf{h/L_{OA} = 0.25}$	$\mathbf{h/L_{OA} = 0.50}$	$\mathbf{h/L_{OA} = 0.75}$	$\mathbf{h/L_{OA} = 1.50}$
Number of cells	17139057	17243685	17507216	16824510
Maximum non-orthogonality	75.9751	75.9638	75.9638	79.3803
Maximum skewness	3.13062	3.17308	3.16055	3.13912
Maximum aspect ratio	28.2153	27.8478	32.0920	32.0000

5.3 COMPUTATION SETUP

To predict hydrodynamic performance of the catamaran in calm water, *interFoam* solver is used. Two degrees of freedom (2DoF) motions are modeled via *rigidBodyMotion* function, that allows heave and pitching motions of the vehicle. To couple pressure and velocity matrices, PIMPLE algorithm is used with predictor-corrector steps and subcycling accelerations, allowing numerical computation of unsteady problems with larger time steps, in which the solution becomes unstable. Therefore, a higher Courant number than a unity is selected, and the time step is adjusted to a maximum value considering ITTC recommendations [85].

To simulate multiphase flow around the catamaran model, the boundary conditions given in Section 4.3.3 are applied to the computational domain, except the bottom boundary. Since the goal is to determine the effect of seafloor on the catamaran, the bottom boundary needs to be modeled as an impermeable wall. In this case, Dirichlet boundary condition is applied on the bottom boundary.

5.4 RESULTS AND DISCUSSION

5.4.1 Grid Dependence Analyzes

In this section, the grid dependency analyzes applied to the catamaran model of interest. Grid dependency analysis is needed to estimate the accuracy of the numerical computation. In this study, grid dependency analyzes are performed at deep water conditions for nine different advance speeds. In this case, generalized Richardson extrapolation method is used to determine the effect of grid resolution on the results [88]. The grid dependency analyzes are applied to the total resistance coefficients.

Table 5.5: Results of the grid dependence study for the catamaran.

Fr	**C_T**			**p**	ε_{21}	ε_{32}	GCI_{21}	GCI_{32}
	Coarse	**Medium**	**Fine**					
0.040	5.576×10^{-2}	2.541×10^{-2}	1.235×10^{-2}	1.150	-0.031	-0.013	1.741	2.187
0.081	2.527×10^{-2}	1.481×10^{-2}	1.124×10^{-2}	1.512	-0.011	-0.036	0.945	0.751
0.162	1.435×10^{-2}	1.141×10^{-2}	1.282×10^{-2}	2.007	-0.003	0.014	0.328	0.274
0.242	1.361×10^{-2}	1.169×10^{-2}	1.168×10^{-2}	3.329	-0.002	-0.000	0.109	0.001
0.323	1.526×10^{-2}	1.436×10^{-2}	1.398×10^{-2}	1.154	-0.001	-0.000	0.186	0.112
0.400	1.435×10^{-2}	1.416×10^{-2}	1.454×10^{-2}	2.619	-0.000	-0.000	0.014	0.041
0.485	1.492×10^{-2}	1.444×10^{-2}	1.441×10^{-2}	2.980	-0.000	-0.000	0.030	0.003
0.646	8.368×10^{-3}	8.939×10^{-3}	8.7929×10^{-3}	3.192	-0.000	-0.000	0.0567	0.020
0.808	6.599×10^{-3}	6.015×10^{-3}	6.5497×10^{-3}	0.272	-0.001	-0.000	1.3598	1.777

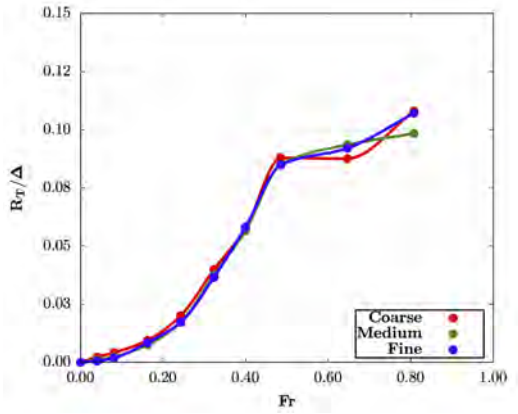

(a) Non-dimensionalized resistance versus Froude number.

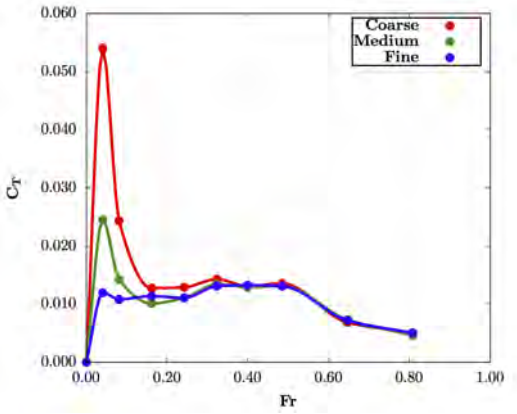

(b) Total resistance coefficient versus Froude number.

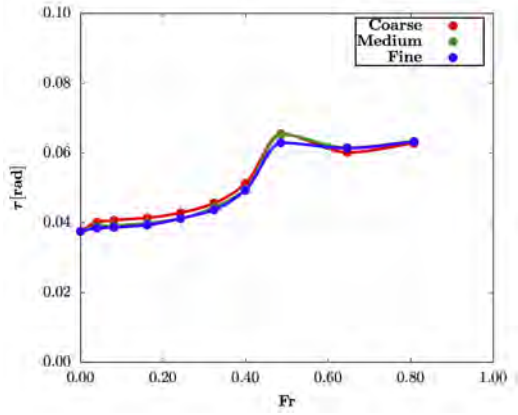

(c) Trim versus Froude number.

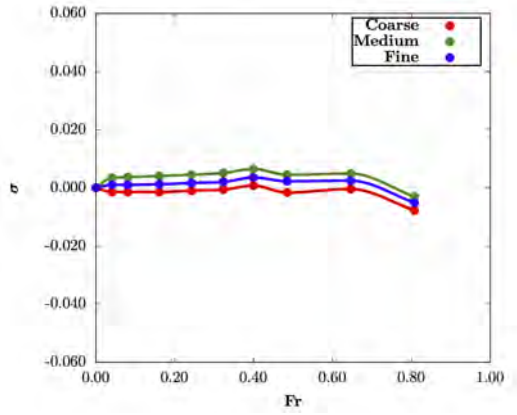

(d) Non-dimensionalized sinkage.

Figure 5.5: Grid sensitivity analysis.

The results of the grid dependency analyzes are given in Table 5.5. Here, p represents the order of accuracy, ε is the estimated error and Grid Convergence Index is a method for uncertainty estimator [89, 88]. At lower Froude numbers, desired accuracy for coarse and medium mesh are not achieved due to the lower refinement levels. This leads to higher uncertainty of the computation. In Figure 5.5 the computation results of the calm-water resistance simulations are illustrated by applying three different grid refinement levels. It is shown that the refinement ratio around the free-surface has an astonishing effect in terms of the sharp-interface resolution,

besides the higher-order numerical scheme. Furthermore, the free-surface refinement directly effects the determination of heave motion, since the distance is measured by interpolating between cell points.

5.4.2 Resistance, Trim and Sinkage

Numerical computations were carried out at four different depths and nine advance speeds, as given in Table 5.2. In this case, the seafloor was modeled as an impermeable wall. Due to the effects of the limited water depth, the depth Froude number (Fr_h) was used to determine the hydrodynamic performance of the catamaran. It is known that substantial performance changes occur in critical and subcritical flows, while the water depth has a negligible effect on the performance in lower subcritical depths.

In Figure 5.6, the hydrodynamic performance of the catamaran is briefly illustrated. It is seen that, in the subcritical region ($Fr_h << 0.5$), resistance, trim and sinkage of the vehicle are independent of the water depth. As it is expected, the resistance of the catamaran increases with the advance speed in deep water. At hullspeed, the total resistance and trim reaches its maximum at ($h/L_{OA} = 0.25$). Therefore, the shallow water definitely affects the hydrodynamic performance by requiring more power to operate than it is needed in deep water. Additionally, as the catamaran operates in trans-critical depths ($Fr_h \approx 1.0$), the dynamic trim and sinkage are effected significantly by causing extreme changes in the dynamic position.

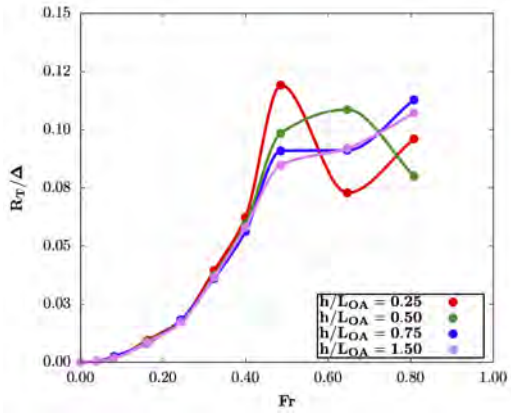

(a) Non-dimensionalized resistance versus Froude number.

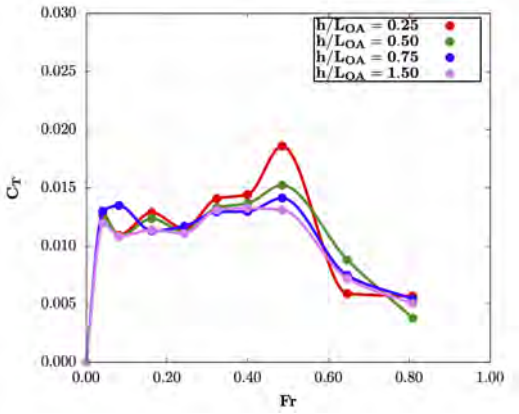

(b) Total resistance coefficient versus Froude number.

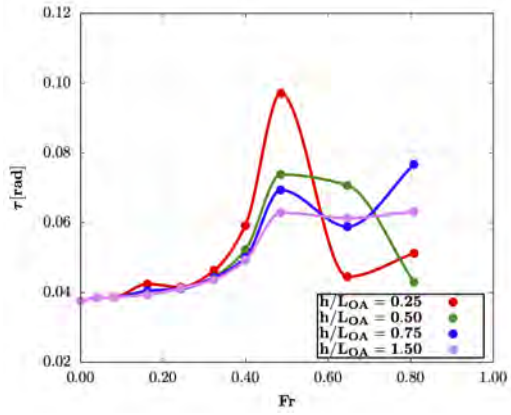

(c) Trim versus Froude number.

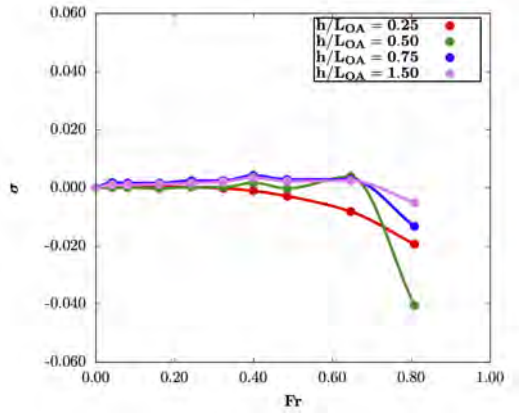

(d) Non-dimensionalized sinkage.

Figure 5.6: Hydrodynamic performance in various limited depths.

5.4.3 Wave Elevation

The most crucial component of the total resistance of a ship is the wave-making resistance, that is, the amount of the energy propagated through the water column. In Figure 5.7 and Figure 5.8, wave patterns generated by catamaran in calm water at different speeds and two distinct depth conditions. While the catamaran is operating through the water column, Kelvin wave system is generated by the transverse and divergent waves. As the speed of the catamaran increases, the divergent waves gain dominance over transverse wave systems, and the interference between bow generated waves increase and shift astern. The dynamic motions and resistance of the catamaran are directly dependent on the position and the amplitude of the wave system. It is observed that, as the surge speed increases, the wave trough overtakes the stern, and the total resistance coefficient gradually decreases. The dynamic trim and sinkage are also affected by the location of the wave trough, while the wave through approaches to the stern.

The height of the divergent waves are inversely proportional to the water depth. The reduction in the clearence under the keel increases the velocity. Therefore, the kinetic energy transforms into the potential energy by increasing the height of divergent bow waves.

The dynamic trim and sinkage of the catamaran depend on the location of the wave trough, being significantly affected as the wave through approaches the stern. As expected, the wave pattern is slightly affected by the Reynolds number (Re). As the water depth decreases, the height of the divergent bow waves increases. This is believed to be because the reduction in the clearance under the keel leads to more of the kinetic energy of the water column being transferred to potential energy, which in turn yields the higher divergent bow waves.

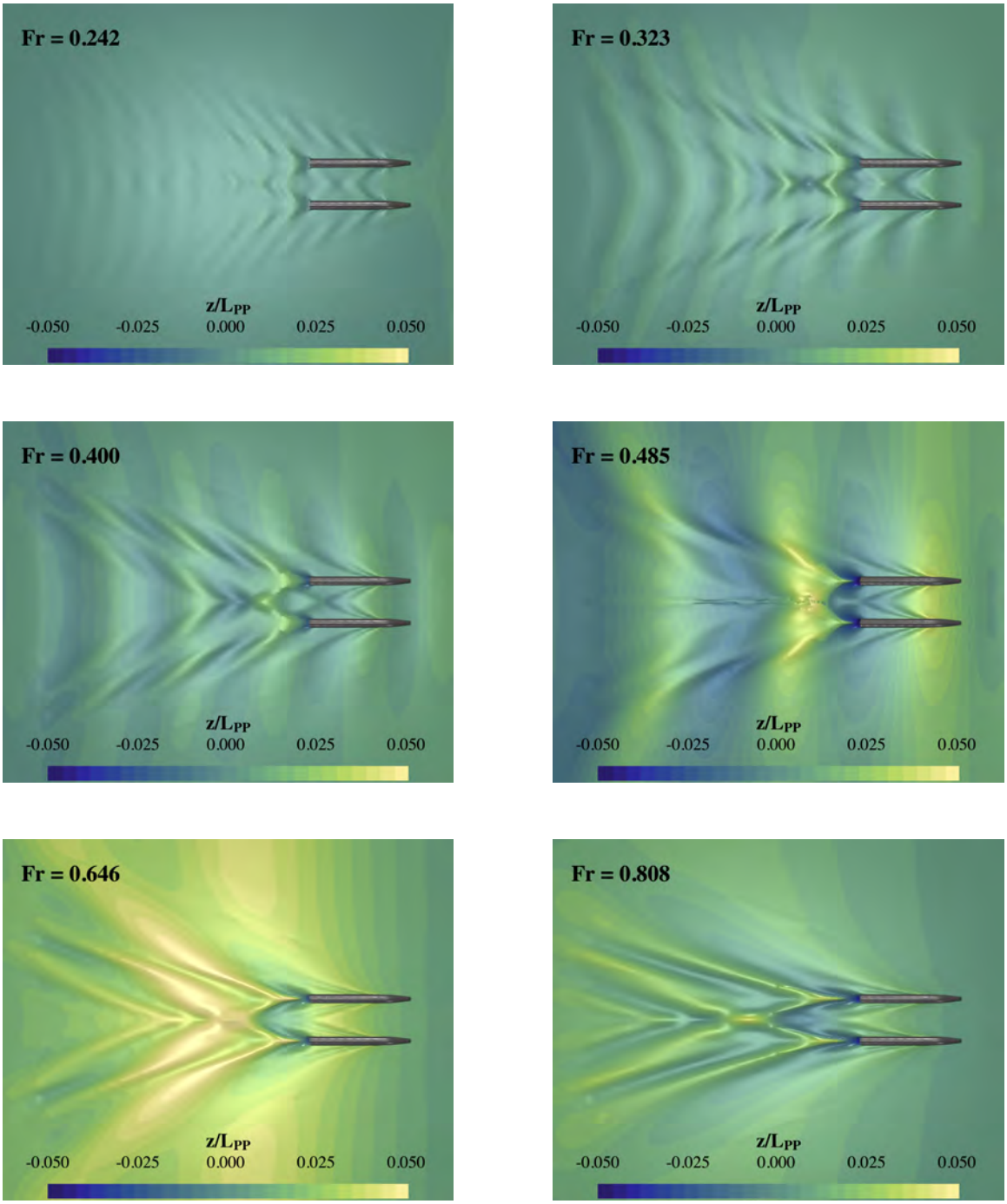

Figure 5.7: Wave elevation contour graphs at different speeds in shallow, calm water ($h = 0.25 \times L_{OA}$).

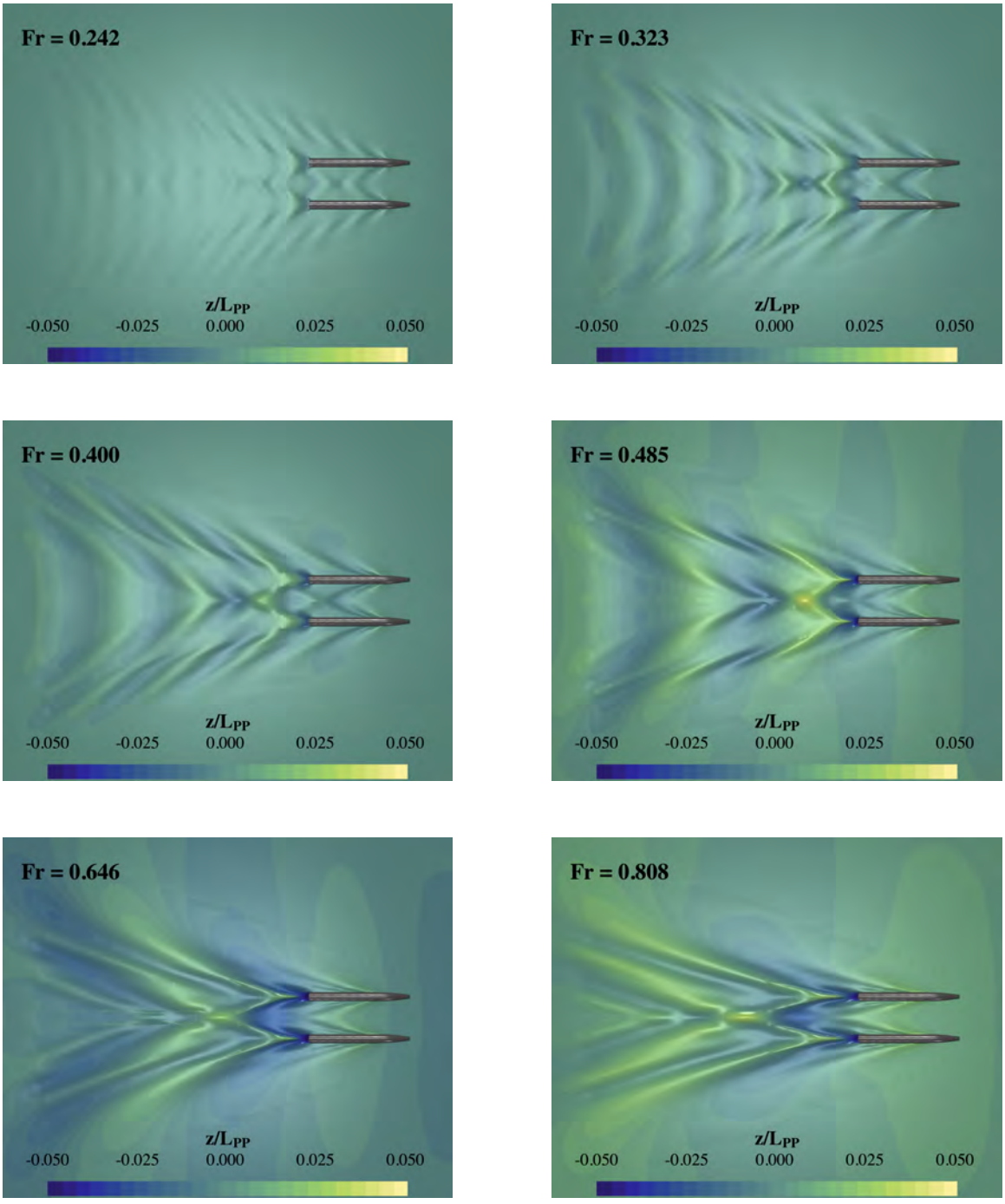

Figure 5.8: Wave elevation contour graphs at different speeds in deep, calm water ($h = 1.50 \times L_{OA}$).

The second crest of the divergent bow wave move towards the region downstream of the catamaran, resulting in different superposition of the waves propagated from the stern. When the catamaran reaches trans-critical speed, the Kelvin wave angle increases as expected.

The critical wave is observed at $Fr_h = 1.154$, located at the upstream of the catamaran. The critical wave is normal to the advance direction of the catamaran and the increment in wave elevation leads to a peak in the resistance curve (Figure 5.6a), and an excessive change in dynamic position (Figure 5.6c). The critical wave vanishes and divergent waves appear at the bow and stern of the catamaran for the vehicle operating in supercritical speeds. The decrease in Kelvin wave angle leads to a shift of bow-generated waves astern.

To investigate the wave propagation generated by the vehicle in calm water, longitudinal wave cuts need to be considered. In Figure 5.9, 5.10 the longitudinal wave cuts at the centerline of the catamaran and midplane of one of the pontoons are presented, respectively. It is seen that the amplitude of the wave trough differs with the dynamic position of the catamaran and the limited water depth. The height of the wave increases with the speed, and it reaches its maximum value at critical speed. The wave troughs propagated behind the stern have larger amplitudes compared to the ones in deep water.

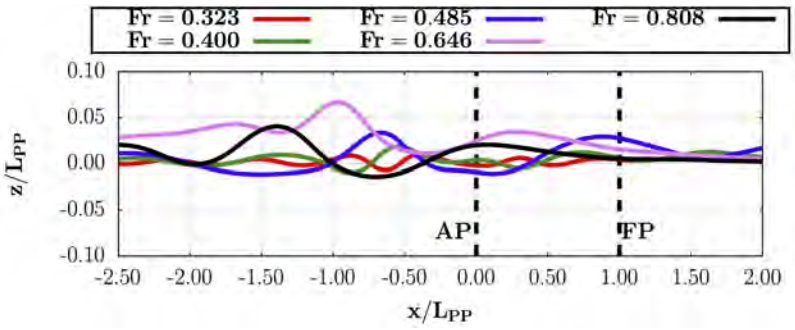

(a) Non-dimensionalized resistance versus Froude number.

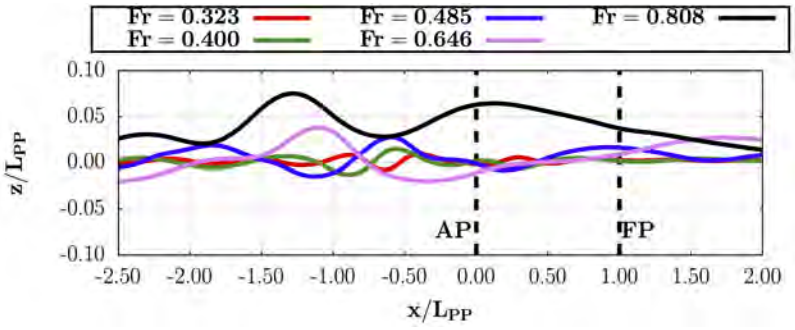

(b) Total resistance coefficient versus Froude number.

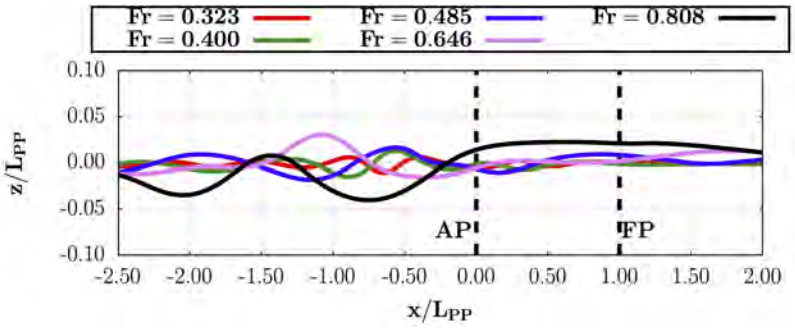

(c) Trim versus Froude number.

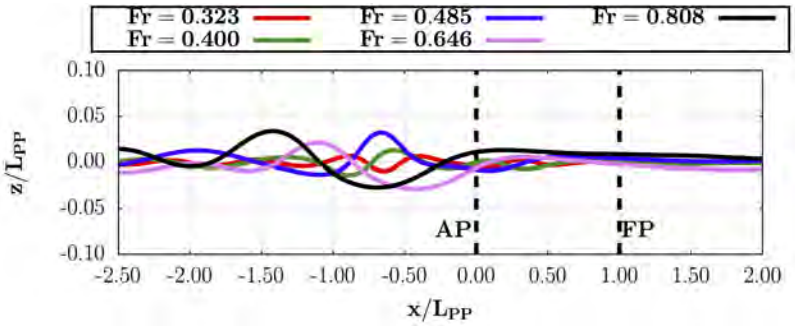

(d) Non-dimensionalized sinkage.

Figure 5.9: Longitudinal wave cut at the centerline of the WAM-V 16.

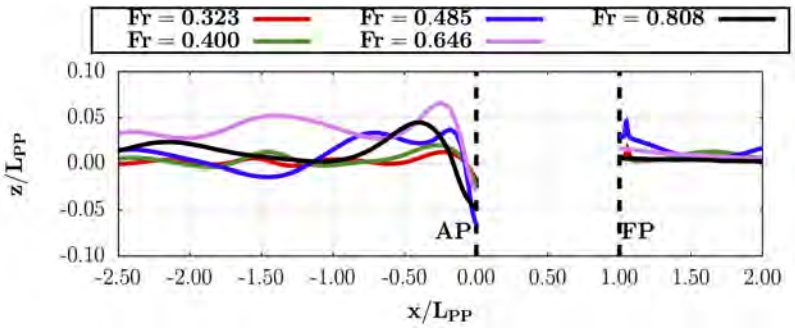

(a) Non-dimensionalized resistance versus Froude number.

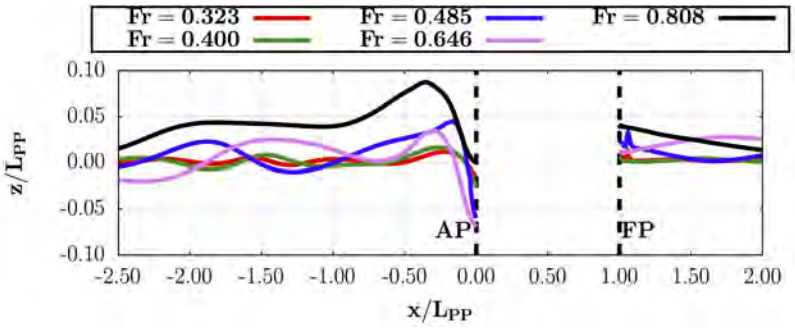

(b) Total resistance coefficient versus Froude number.

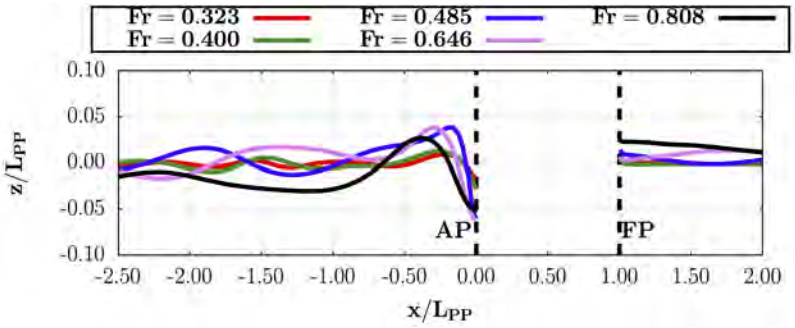

(c) Trim versus Froude number.

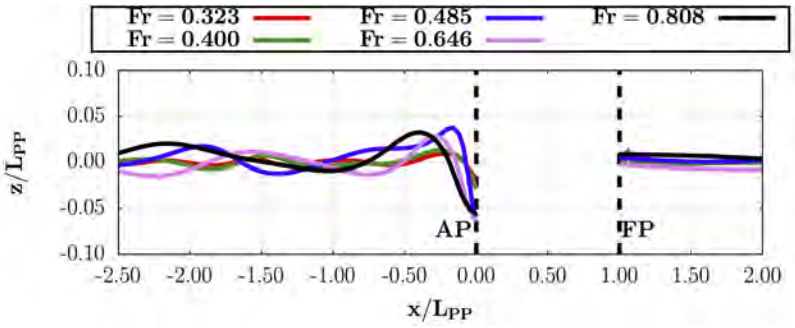

(d) Non-dimensionalized sinkage.

Figure 5.10: Longitudinal wave cut at the centerline of the pontoon.

CHAPTER 6
SEAKEEPING PERFORMANCE PREDICTION OF THE CATAMARAN IN NEAR-SHORE TRANSFORMING SEAS

In the previous chapter, the hydrodynamic performance of the catamaran is analyzed in limited depth water in the absence of the wave propagation. In this chapter, the seakeeping performance of the catamaran is analyzed in calm water, head and following seas by applying thrust forces at the thruster centerline by using the overset technology. Rather than towing the catamaran at a constant speed through the computational domain, a time dependent thrust force in terms of a ramp profile is applied on the both thruster centerline. To accomplish this physical phenomena, seakeeping performance of the catamaran of interest is analyzed by using waves2Foam® wave generation and absorption toolbox and OpenFOAM®. A unique characteristic of the current approach is the three-degrees of freedom (3DoF) motions of the vehicle are modeled via rigid body motion and overset (Chimera) grids, wave generations are modeled via 10^{th} order stream function wave theory and *overWaveDyMFoam* solver is developed to model the six degrees of freedom motions of floating bodies under wave propagation.

6.1 TEST CONDITIONS

Numerical computations are conducted to define total resistance, trim and sinkage chararacteristics of the vehicle in transforming seas by accelerating from static position to its operational speed by using 1/2 sinusoidal ramp profile. The operational speed is selected at 2 m/s. In this case, the thrust characteristics of the catamaran

are taken from results of the sea-trials [90]. The corresponding thrust force is applied to both thrusters via a half-sinusoidal ramp function, as shown in Figure 6.1.

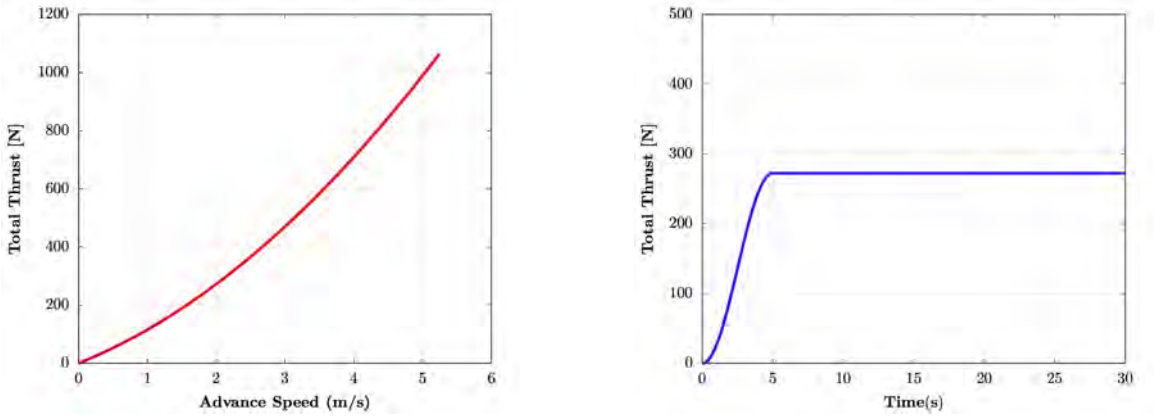

(a) Experimental data.

(b) Half-sinusoidal ramp function.

Figure 6.1: The extraction of total thrust from experimental data and application in a numerical simulation as a function of time.

The corresponding thrust force is applied to the catamaran in two distinct scenarios in calm water. In the first scenario, the catamaran operates from the shallow water zone to the deepwater zone. In this case, five simulations are carried out to evaluate performance prediction with respect to the different wave steepness. During the catamaran operation from shallow water to deep water, the vehicle encounters the head waves approaching the shoreline. In the second scenario, the catamaran operates from the deep water zone to the shallow water zone. In this scenario, five simulations are carried out with similar wave steepness as in the first scenario, while the catamaran encounters the following waves approaching the shoreline. The test conditions of the seakeeping computations are given in Table 6.1

Table 6.1: Seakeeping conditions for the WAM-V 16 model in transforming seas.

Wave Encounter Angle $\boldsymbol{\beta}$	**Wave Steepness** $\boldsymbol{H/\lambda}$	**Wave Number** $\mathbf{k}$	**Encounter Frequency** $\boldsymbol{\omega_e}$
180°	0.012	1.283	0.923
	0.018		
	0.025		
	0.036		
0°	0.012		0.156
	0.018		
	0.025		
	0.036		

6.2 COMPUTATIONAL SETUP

6.2.1 Physics Modeling

To model the motion of the vehicle along the shoreline, the overset method is a remarkable approach due to the complexity of the current phenomena. Therefore, a new solver *overWaveDyMFoam* is developed by combining an open-source wave generation and absorption toolbox "waves2Foam" and open-source CFD library OpenFOAM®. Continuity, momentum and phase transfer functions are coupled via PISO predictor-corrector scheme. In this case, time-derivative terms are discretized using Crank-Nicolson scheme, that is a second order bounded scheme. The convective terms are discretized using a TVD bounded scheme with vanLeer limiter. The diffusion terms are discretized via linear interpolation scheme. To model High-Reynolds number flow throughout the computational domain, SST $k-\omega$ turbulence model is used due to its strength in resolving boundary layer.

The pressure forces are computed by the integration of forces on the normal direction over the surface, while the viscous forces are calculated by the integration on

the tangential direction over the surface. The three-degrees of freedom motions of the catamaran is modeled via *rigidBodyMotion* function.

6.3 MESH GENERATION

To model the surge, heave and pitch motions, the catamaran is accelerated through the transforming near-shore region. This has two main consequences. Firstly, the computational domain cannot fulfill the recommendations of the ITTC [85], regarding the dimensions of the computational fluid domain. Instead, a computational domain is generated, allowing enough distance for the vehicle to accelerate through the transforming seas. Naturally, the depth of the computational domain must support the test cases considered in Chapter 5. The length of the computational domain is set as $20 \times L_{OA}$. The height of the background domain is set to $0.5 \times L_{OA}$ from the still water surface in all cases. The specifics of computational domain is illustrated in Figure 6.2.

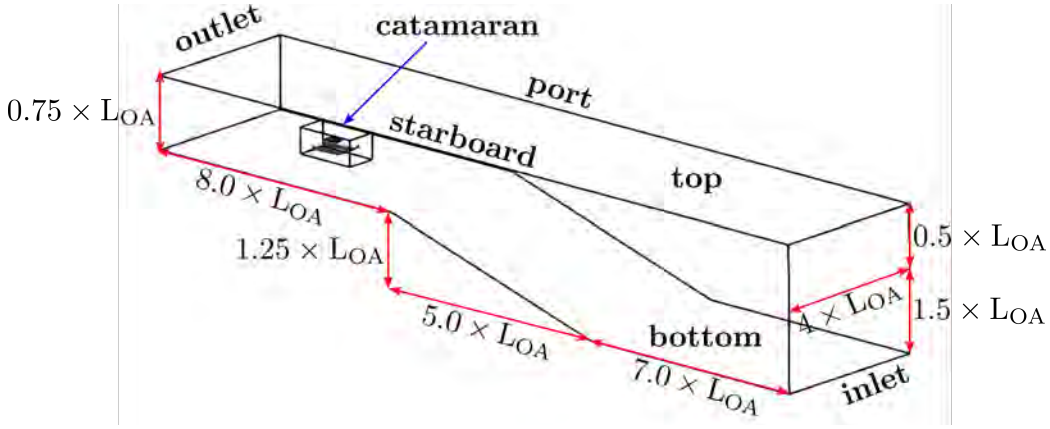

Figure 6.2: Computational domain for seakeeping simulations.

After creating a computational domain for the seakeeping simulations, the height of cells on the free-surface refinement region is calculated by applying 8 refinement levels, which corresponds to $\left(\frac{L_{OA}}{1000}\right)$. To have an isotropic mesh, the initial cell size of the overlapping domain in all three directions is defined by $\left(\frac{16 \times L_{OA}}{1000}\right)$. To generate

viscous sublayer on the bottom boundary, the same approach is used by applying a target non-dimensional wall distance $\left(y^{+}_{target}\right)$ value of 300. To create an overlapping domain slightly bigger than the catamaran, the overlapping domain is generated as multiples of its initial cell size. In this case, the reference size of the overlapping domain can be considered as a function of its dimensions. The length of the overlapping domain is set to $1.5 \times L_{ref}$, the width is set to, $1.5 \times B_{ref}$ and the height is set to $2.0 \times H_{ref}$. To have an exact cell size at interpolation location, then a refinement region is applied with a refinement level of 4 and a diffusion ratio of 3 around the overlapping domain. In Figure 6.3, the refinement regions around the catamaran and overlapping are illustrated.

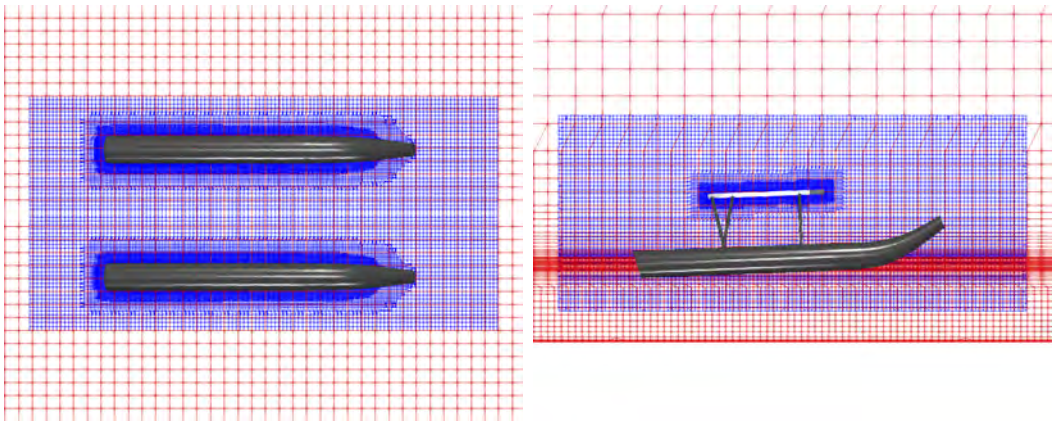

Figure 6.3: Overlapping domain and overset mesh generation.

6.4 RESULTS AND DISCUSSION

This section presents the obtained results from seakeeping simulations, their analysis and discussion. To begin with, the performance characteristics of the catamaran moving from shallow water zone to deep water zone through a sloping seafloor are analyzed. During the first 30 seconds of the simulation, the vehicle is set at rest. During this time period, the waves propagate through the domain and spread the wave energy through the water column. After 30 seconds, the vehicle starts accelerating until it reaches its maximum thrust. Between 40 and 45 seconds, the vehicle reaches to the edge of sloped seafloor, in which the resistance, trim and sinkage values maximizes and suddenly drops. At this point, the depth Froude number maximizes to $Fr_h \approx 0.7$. Even though, potential theory specifies that the critical Froude number is $Fr_h = 1.0$, previous studies based on nonlinear approaches and CFD simulations showed that critical depth Froude number is lower than a unity [91, 92]. After 45 seconds, the vehicle begin accelerating until the total resistance is equivalent to maximum thrust.

In the existence of head waves, the position of the vehicle at rest is affected by the wave propagation from deep water to shallow water. As the vehicle begins accelerating, heave motion gradually increases and reaches its maximum till it passes the shallow water zone. In this case, it is obvious that the waves approaching to the shoreline are absorbed by the sloped seafloor. When the vehicle passes to the deep water region, heave and pitch begins oscillating, since the hull is under regular wave effects.

Another way of interpreting these results can be in terms of the wave field. As the catamaran begins accelerating from shallow water zone to deep water zone, the distance between wave crests and troughs increases, and the transverse wave system is dominated by the divergent wave system. Specifically, transverse wave system is absorbed in the deep water region, in which the catamaran is not affected by the seafloor. Additionally, as the surge speed increases and the catamaran moves from

transitional zone to deep water zone, the Kelvin wave angle gradually decreases. In Figure 6.4, the instantaneous wave elevation graphs are presented. After 50 seconds, the wave-ship interaction can be observed definitively. The head waves transport their energy to the bow generated divergent waves, and the wavelength between catamaran generated waves increase. Most of the energy is absorbed by the sloped seafloor, since the wave elevation is sufficiently small in the shallow water region.

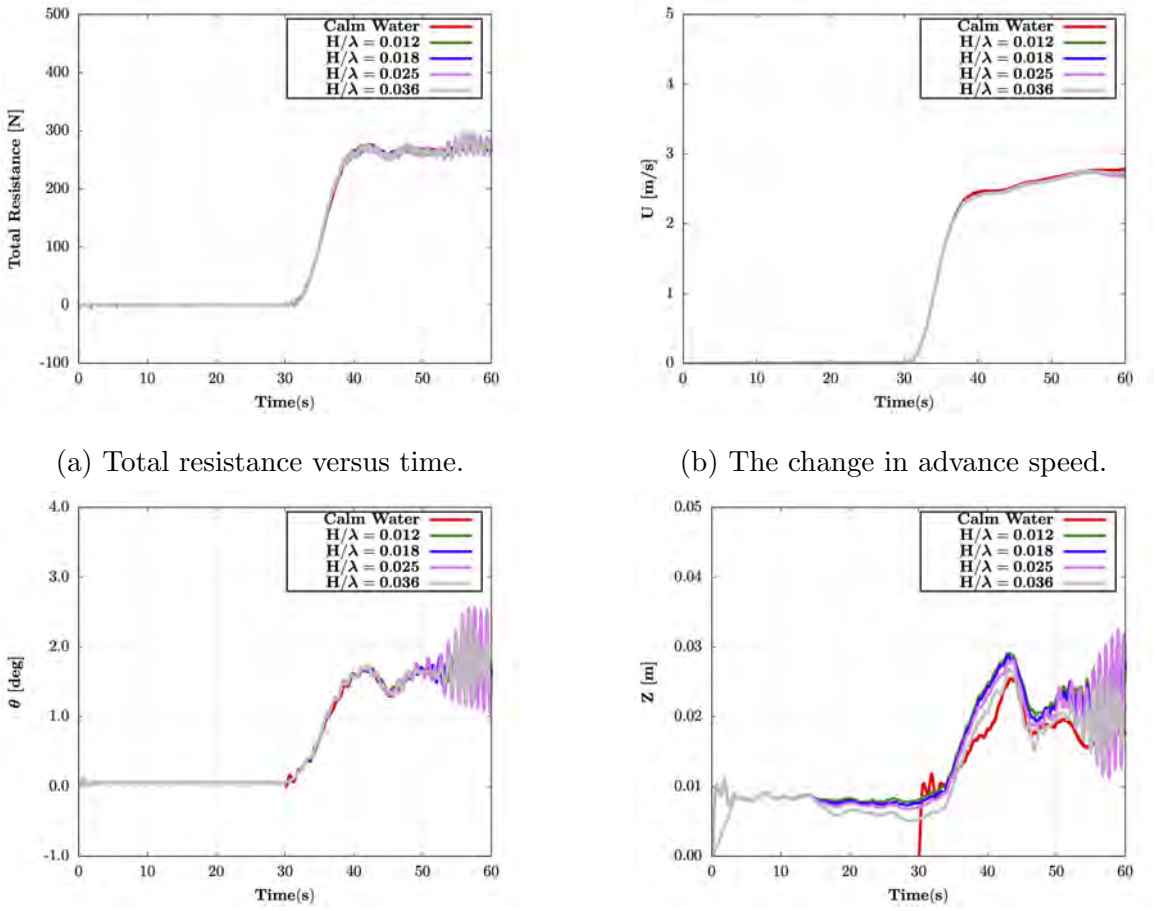

(a) Total resistance versus time.

(b) The change in advance speed.

(c) Pitch angle versus time.

(d) Heave motion versus time.

Figure 6.4: Seakeeping characteristics of the catamaran operating from shallow water zone to deep water zone.

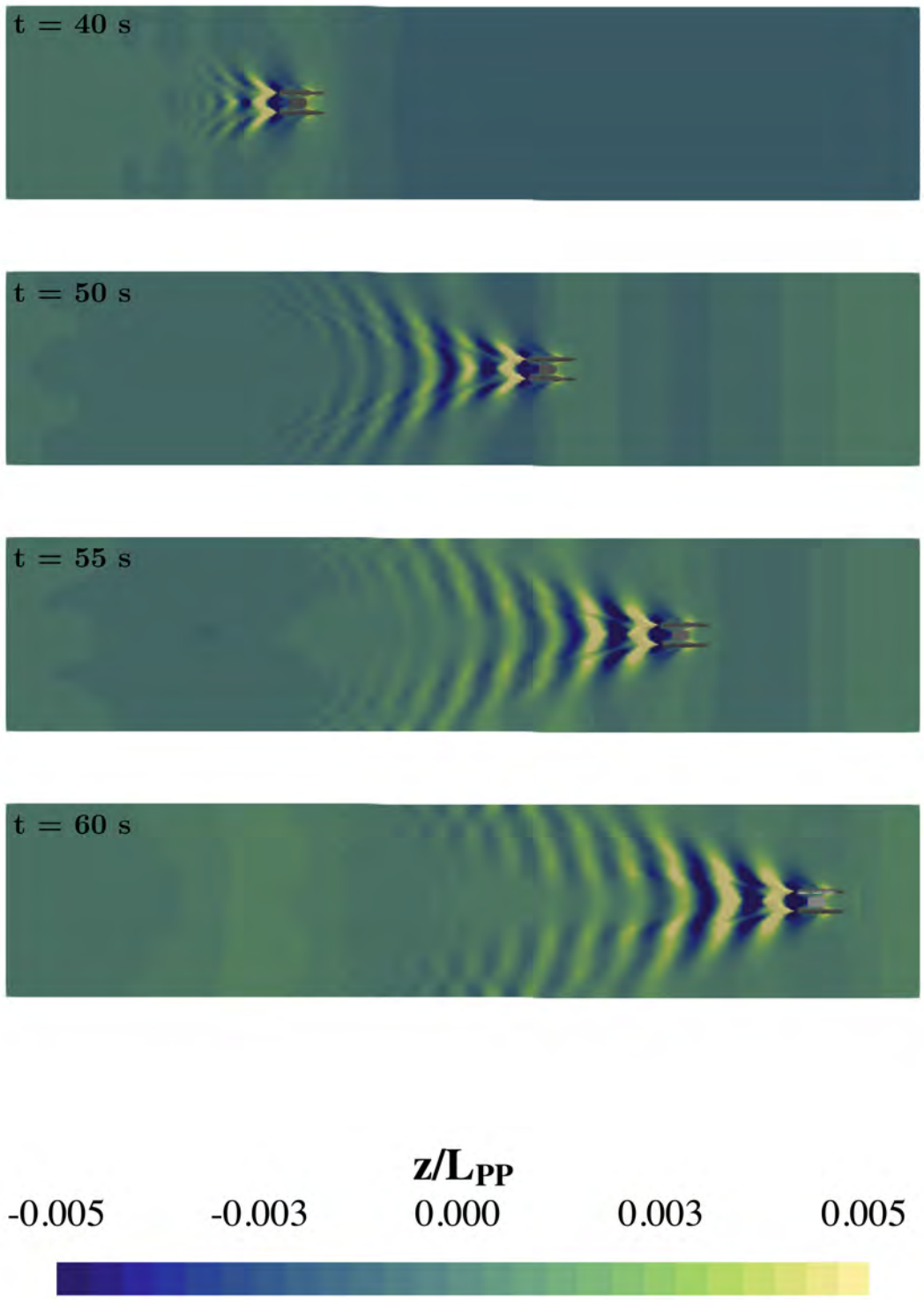

Figure 6.5: Instantaneous wave elevations while the catamaran is moving from shallow water zone to deep water zone.

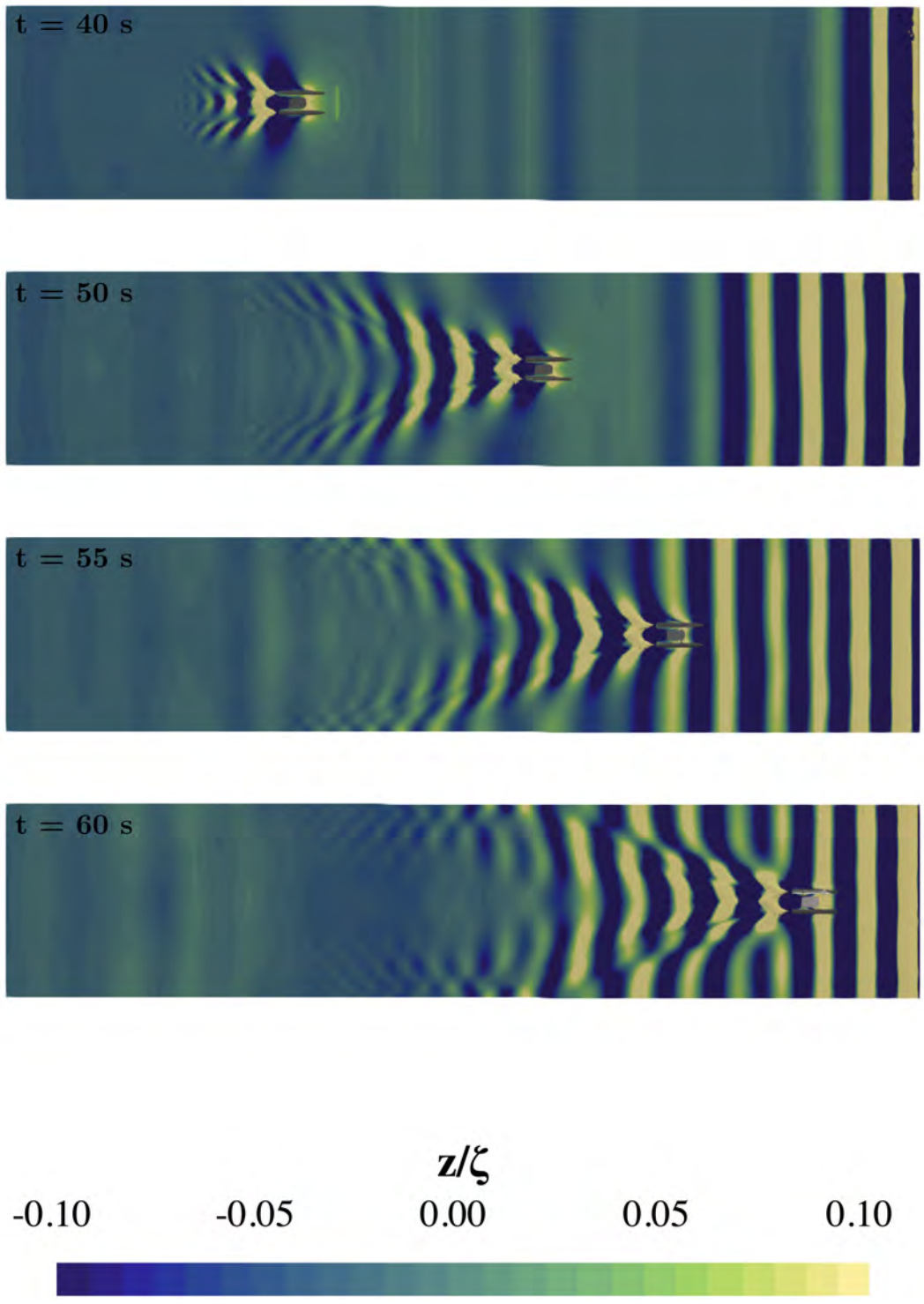

Figure 6.6: Instantaneous wave elevations while the catamaran is moving from shallow water zone to deep water zone under head waves.

Figure 6.7 illustrates the seakeeping characteristics of the catamaran moving from deep water to shallow water zone in following seas. In the first 30 seconds, the vehicle is at rest, but under the effect of following waves. When the vehicle begins accelerating, the divergent and transverse wave systems propagate towards offshore and boost the amplitude of the following waves by dissipating wave energy. When the catamaran approaches to shoreline from deep water zone, the Kelvin wave angle begins gradually increasing, due to the existence of an impermeable wall, as expected. Moreover, the amplitude of crests and troughs gradually rises, as the catamaran approaches to shallow water zone, and it keeps increasing in near-shore.

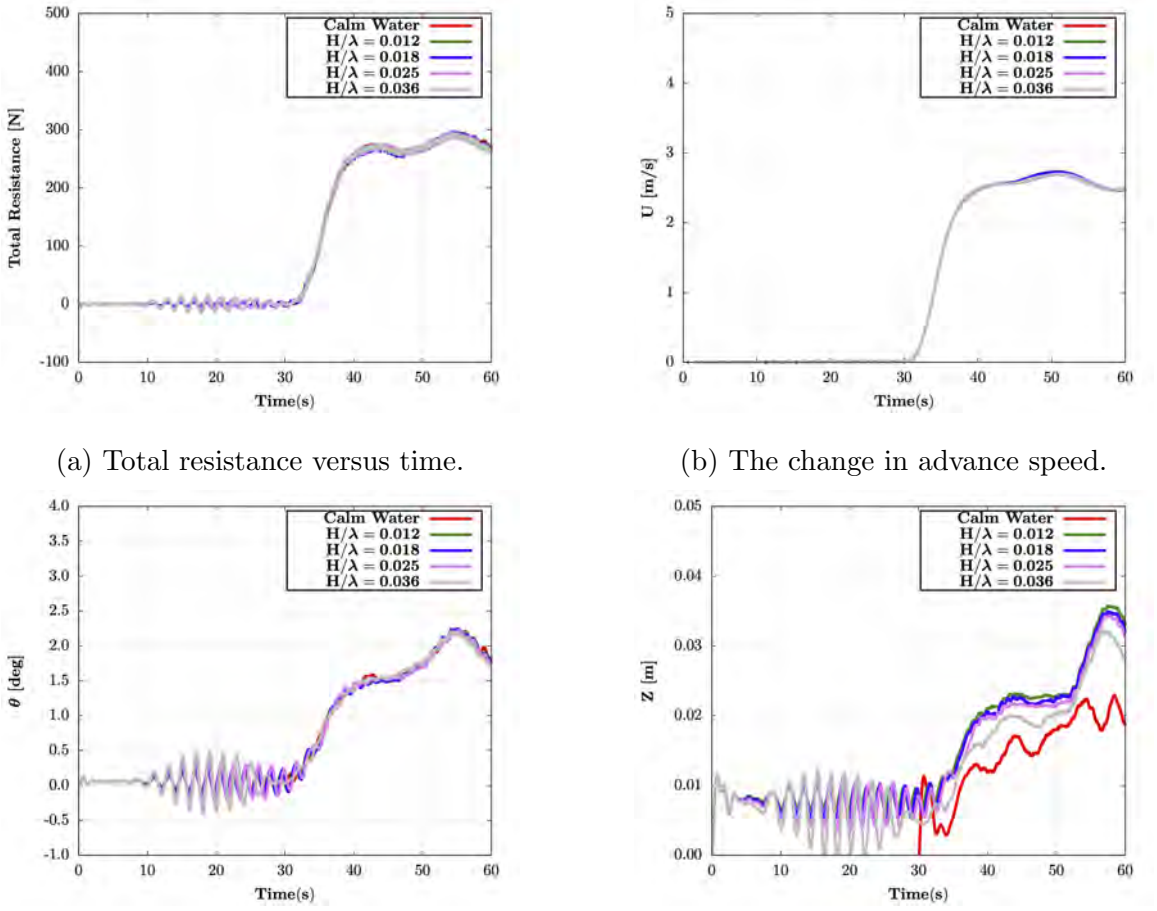

(a) Total resistance versus time.

(b) The change in advance speed.

(c) Pitch angle versus time.

(d) Heave motion versus time.

Figure 6.7: Seakeeping characteristics of the catamaran operating from deep water zone to shallow water zone.

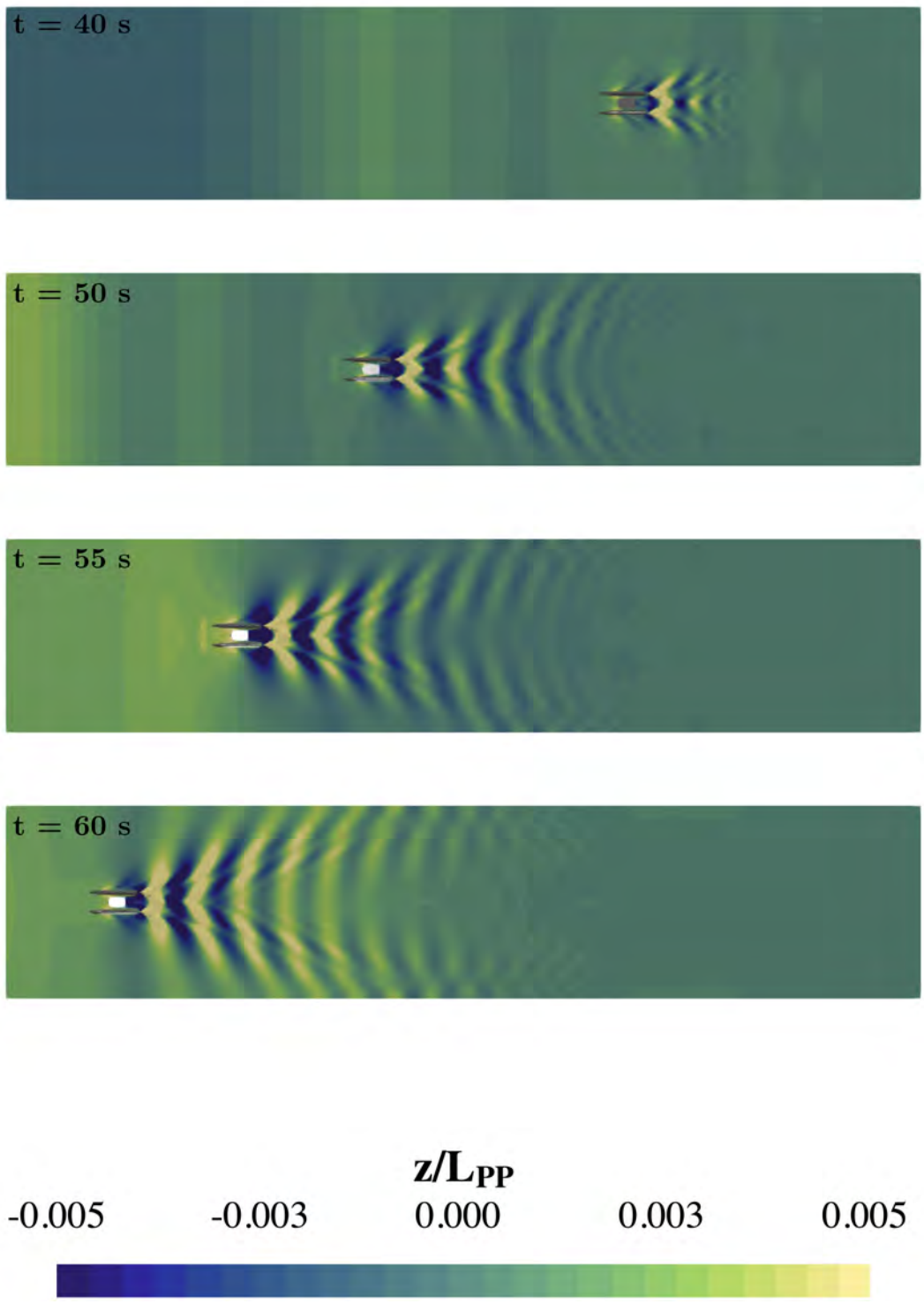

Figure 6.8: Instantaneous wave elevations while the catamaran is moving from deep water zone to shallow water zone.

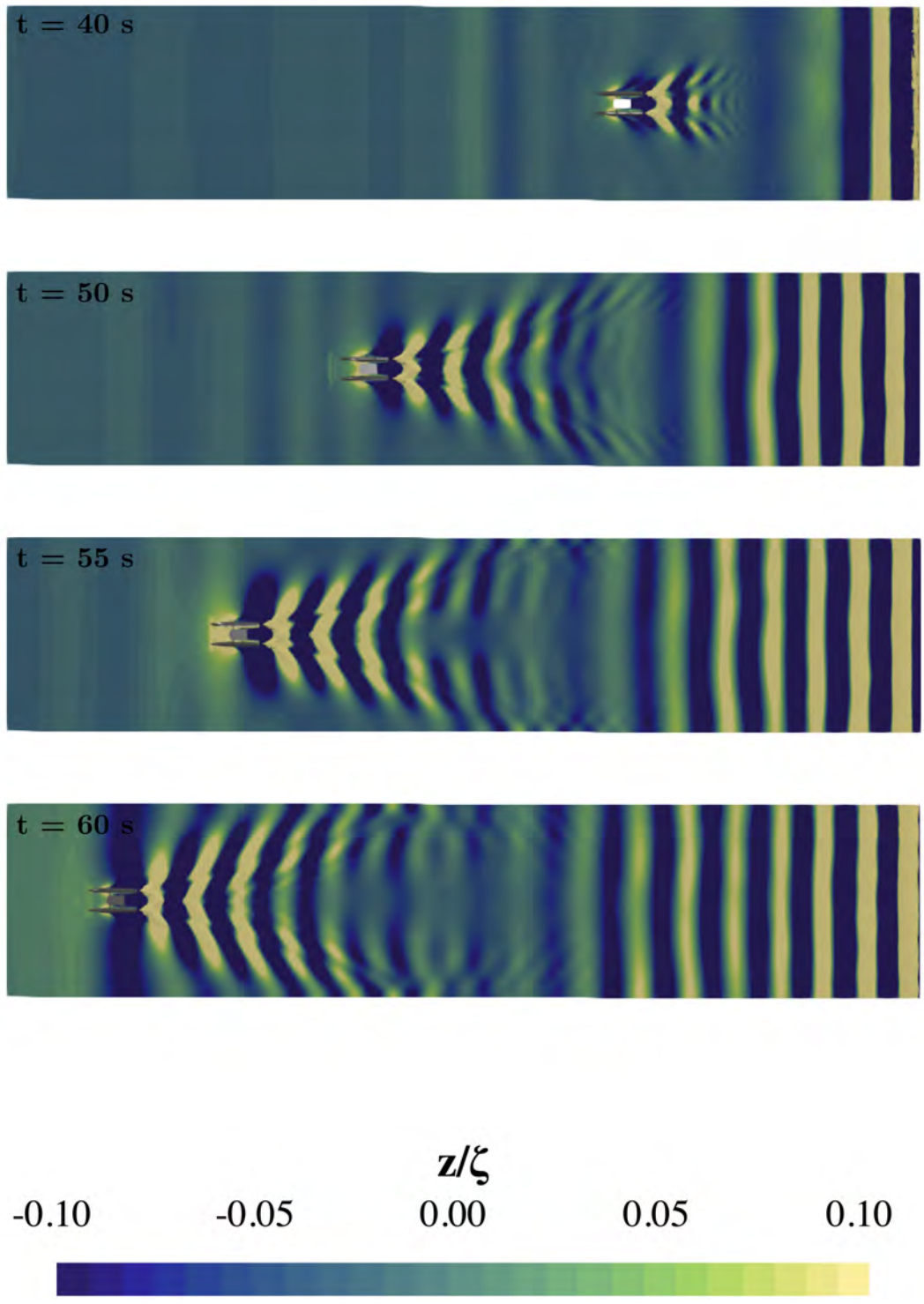

Figure 6.9: Instantaneous wave elevations while the catamaran is moving from deep water zone to shallow water zone under following waves.

Furthermore, when the catamaran approaches the near-shore, it attempts to increase its speed to meet the power requirements since the resistance increases. However, the resistance is more excellent than the thrust. It leads to a reduction in the speed of the catamaran.

CHAPTER 7

CONCLUSIONS AND FUTURE RESEARCH INTERESTS

The principal aim of this thesis is to characterize the hydrodynamic and seakeeping performance of a catamaran in transforming waters through numerical computations. In support of this goal, a series of parametric studies were conducted for a catamaran operating in calm waters as well as in the presence of waves in transforming seas. The numerical approach used in this study is described in Chapter 3.

OpenFOAM® framework was applied for the prediction of calm-water resistance and seakeeping performance of a ship in an extreme wave environment. A unique characteristic of the current approach is the mesh transformation due to dynamic motion, two degrees of freedom of motion, and wave generation are included in one solver algorithm. Specifically, it is shown that the equations of rigid body motions can be integrated into a solver for a fundamental problem of the motions of the KRISO container ship (KCS) in calm water and head-seas. The prediction of the total resistance and motions are shown to be in a good agreement with the experimental results over a wide range of case conditions.

The calm-water simulations show that for a catamaran operating in shallow waters, the total resistance, dynamic trim and sinkage characteristics are impacted by the local water depth. The impact varies as the vehicle moves from shallow waters to deep water and vice versa. In the calm water conditions, the total resistance, trim and sinkage of the catamaran were determined as functions of Fr for different water depths. It is observed that the total resistance increased gradually with increasing Fr in deep water, while it reaches a peak and decreases to a minimum at $Fr_h \approx 1.0$. Moreover, the total resistance at $(h = 0.25 \times L_{OA})$ is found to be larger than the

resistance in deep water for ($Fr < 0.400$) and smaller for larger values of Fr. The dynamic pressure distribution on the hull has the greatest contribution to the total resistance, while dynamic pressure gradients has significant impacts on the dynamic trim and sinkage. In particular, the dynamic sinkage decreases with increase in Fr in deep water, while a significant peak occurs at trans-critical speeds ($Fr_h = 1.154$). Furthermore, the wave systems are enhanced and move astern as the Froude number increases in all scenarios. The amplitudes of the wave crests and troughs achieved maximum values in the trans-critical depth range. In the presence of small-amplitude head and following seas, transforming due to decrease in water depth, interesting interactions are observed between the incident waves and those generated by the motion of the vehicle. The interactions have measurable impacts on the hydrodynamic and seakeeping performances of the vehicle. The impact is believed to be influenced by waves propagating through the water column, coupled with the change in the local bathymetry. The impacts are characterized for their dependence on Froude number and incident wave steepness. As the vehicle approaches the shoreline, it experiences an increase in wave resistance. Additionally, as the depth Froude number changes over the sloped bottom and exceeds or attains its critical value, solitary waves generated by the catamaran appear not to shed sufficiently quickly ahead of the vehicle. In this case, the catamaran appears to be moving against the wave.

The study can be extended to consider simulations of a maneuvering vehicle, including making allowances for appendages on the vehicle. Further, the wave generation can be performed using a HOS-Ocean® and OpenFOAM® coupling, which does not require memory allocation. Therefore, it can be a computationally efficient approach.

BIBLIOGRAPHY

[1] J. Guerrero and M. Bargiacchi, "Introductory openfoam course," *Università degli Studi di Genova*, 2014.

[2] T. Petra, "Description of the overset mesh approach in esi version of openfoam," *Proceedings of the CFD with OpenSource Software; Nilsson, H., Ed*, 2019.

[3] J. Tu, G. H. Yeoh, and C. Liu, *Computational fluid dynamics: a practical approach*. Butterworth-Heinemann, 2018.

[4] L. Larsson, "Ship resistance and flow," *Published by The Society of Naval Architects and Marine Engineers, SNAME, The Principles of Naval Architecture Series, ISBN: 978-0-939773-76-3*, 2010.

[5] F. Stern, J. Yang, Z. Wang, H. Sadat-Hosseini, M. Mousaviraad, S. Bhushan, and T. Xing, "Computational ship hydrodynamics: nowadays and way forward," *International Shipbuilding Progress*, vol. 60, no. 1-4, pp. 3–105, 2013.

[6] T. Hino, F. Stern, L. Larsson, M. Visonneau, N. Hirata, and J. Kim, *Numerical Ship Hydrodynamics: An Assessment of the Tokyo 2015 Workshop*, vol. 94. Springer Nature, 2020.

[7] H. Raven, "A computational study of shallow-water effects on ship viscous resistance," in *Proceedings of the 29th Symposium on Naval Hydrodynamics, Gothenburg, Sweden*, vol. 27, 2012.

[8] N. R. Ammar, M. M. Elgohary, A. Zeid, and A. G. Elkafas, "Prediction of shallow water resistance for a new ship model using cfd simulation: case study container

barge," *Journal of Ship Production and Design*, vol. 35, no. 02, pp. 198–206, 2019.

[9] M. Nakisa, A. Maimun, Y. Ahmed, F. Behrouzi, and A. Tarmizi, "Numerical estimation of shallow water effect on multipurpose amphibious vehicle resistance," *Journal of Naval Architecture and Marine Engineering*, vol. 14, no. 1, pp. 1–8, 2017.

[10] A. Molland, P. Wilson, D. Taunton, S. Chandraprabha, and P. Ghani, "Resistance and wash measurements on a series of high speed displacement monohull and catamaran forms in shallow water," *Transactions of The Royal Institution of Naval Architects Part A: International Journal of Maritime Engineering*, vol. 146, no. 2, pp. 19–38, 2004.

[11] P. K. Patel and M. Premchand, "Numerical investigation of the influence of water depth on ship resistance," *International Journal of Computer Applications*, vol. 116, no. 17, 2015.

[12] J. Carlton, *Marine propellers and propulsion*. Butterworth-Heinemann, 2018.

[13] J. L. Hess and A. O. Smith, "Calculation of potential flow about arbitrary bodies," *Progress in Aerospace Sciences*, vol. 8, pp. 1–138, 1967.

[14] G. Gadd, "A method of computing flow and surface wave pattern around full forms, trans," *Royal Institution of Naval Architects*, vol. 18, 1976.

[15] C. Dawson, "A practical computer method for solving ship-wave problems," in *Proceedings of Second International Conference on Numerical Ship Hydrodynamics*, pp. 30–38, 1977.

[16] G. Jensen, *Berechnung der stationären Potentialströmung um ein Schiff unter Berücksichtigung der nichtlinearen Randbedingung an der Wasseroberfläche*. 1988.

[17] H. C. Raven, "A solution method for the nonlinear ship wave resistance problem.," 1998.

[18] L. Larsson, "Shipflow user's manual and theoretical manual," *FLOWTECH Int. AB, Gothenburg*, 1997.

[19] H. Söding, A. von Graefe, O. el Moctar, and V. Shigunov, "Rankine source method for seakeeping predictions," in *International Conference on Offshore Mechanics and Arctic Engineering*, vol. 44915, pp. 449–460, American Society of Mechanical Engineers, 2012.

[20] V. Bertram and P. Gualeni, "An overview of seakeeping tools for maritime applications," *Sustainable Maritime Transportation and Exploitation of Sea Resources*, p. 181, 2011.

[21] S. Hirdaris, W. Bai, D. Dessi, A. Ergin, X. Gu, O. Hermundstad, R. Huijsmans, K. Iijima, U. D. Nielsen, J. Parunov, *et al.*, "Loads for use in the design of ships and offshore structures," *Ocean engineering*, vol. 78, pp. 131–174, 2014.

[22] R. T. Schmitke, "Ship sway, roll, and yaw motions in oblique seas," tech. rep., 1978.

[23] O. Reynolds, "Iv. on the dynamical theory of incompressible viscous fluids and the determination of the criterion," *Philosophical transactions of the royal society of london.(a.)*, no. 186, pp. 123–164, 1895.

[24] Y. Tahara, R. V. Wilson, P. M. Carrica, and F. Stern, "Rans simulation of a container ship using a single-phase level-set method with overset grids and the prognosis for extension to a self-propulsion simulator," *Journal of marine science and technology*, vol. 11, no. 4, pp. 209–228, 2006.

[25] P. M. Carrica, R. V. Wilson, R. W. Noack, and F. Stern, "Ship motions using single-phase level set with dynamic overset grids," *Computers & fluids*, vol. 36, no. 9, pp. 1415–1433, 2007.

[26] R. Wilson, L. Ji, S. Karman, D. Hyams, K. Sreenivas, L. Taylor, and D. Whitfield, "Simulation of large amplitude ship motions for prediction of fluid-structure interaction," in *Proceedings of the 27th Symposium on Naval Hydrodynamics, ONR, Seoul*, 2008.

[27] S. Park, S. W. Park, S. H. Rhee, S. B. Lee, J.-E. Choi, and S. H. Kang, "Investigation on the wall function implementation for the prediction of ship resistance," *International Journal of Naval Architecture and Ocean Engineering*, vol. 5, no. 1, pp. 33–46, 2013.

[28] J. Banks, A. Phillips, P. Bull, and S. Turnock, "Rans simulations of the multiphase flow around the kcs hullform," 2010.

[29] P. M. Carrica, F. Ismail, M. Hyman, S. Bhushan, and F. Stern, "Turn and zigzag maneuvers of a surface combatant using a urans approach with dynamic overset grids," *Journal of Marine Science and technology*, vol. 18, no. 2, pp. 166–181, 2013.

[30] H. Sadat-Hosseini, P.-C. Wu, P. M. Carrica, H. Kim, Y. Toda, and F. Stern, "Cfd verification and validation of added resistance and motions of kvlcc2 with fixed and free surge in short and long head waves," *Ocean Engineering*, vol. 59, pp. 240–273, 2013.

[31] C. D. Simonsen, J. F. Otzen, S. Joncquez, and F. Stern, "Efd and cfd for kcs heaving and pitching in regular head waves," *Journal of Marine Science and Technology*, vol. 18, no. 4, pp. 435–459, 2013.

[32] Z.-r. Shen, H.-x. Ye, and D.-c. Wan, "Urans simulations of ship motion responses in long-crest irregular waves," *Journal of Hydrodynamics*, vol. 26, no. 3, pp. 436–446, 2014.

[33] S. Bhushan, T. Xing, P. Carrica, and F. Stern, "Model-and full-scale urans simulations of athena resistance, powering, seakeeping, and 5415 maneuvering," *Journal of Ship Research*, vol. 53, no. 04, pp. 179–198, 2009.

[34] Z. Shen and D. Wan, "Computation of steady viscous flows around ship with free surface by overset grids techniques in openfoam," in *The Twenty-fourth International Ocean and Polar Engineering Conference*, OnePetro, 2014.

[35] T. Tezdogan, Y. K. Demirel, P. Kellett, M. Khorasanchi, A. Incecik, and O. Turan, "Full-scale unsteady rans cfd simulations of ship behaviour and performance in head seas due to slow steaming," *Ocean Engineering*, vol. 97, pp. 186–206, 2015.

[36] P. M. Carrica, A. Mofidi, K. Eloot, and G. Delefortrie, "Direct simulation and experimental study of zigzag maneuver of kcs in shallow water," *Ocean engineering*, vol. 112, pp. 117–133, 2016.

[37] H. Sadat-Hosseini, D.-H. Kim, P. M. Carrica, S. H. Rhee, and F. Stern, "Urans simulations for a flooded ship in calm water and regular beam waves," *Ocean Engineering*, vol. 120, pp. 318–330, 2016.

[38] T. Tezdogan, A. Incecik, and O. Turan, "Full-scale unsteady rans simulations of vertical ship motions in shallow water," *Ocean Engineering*, vol. 123, pp. 131–145, 2016.

[39] T. Castiglione, F. Stern, S. Bova, and M. Kandasamy, "Numerical investigation of the seakeeping behavior of a catamaran advancing in regular head waves," *Ocean Engineering*, vol. 38, no. 16, pp. 1806–1822, 2011.

[40] T. Castiglione, H. Sadat-Hosseini, F. Stern, and S. Bova, "Cfd simulation for sea keeping of delft catamaran in regular head and oblique waves," in *Proceedings of the 12th International Conference on Fast Sea Transportation (FAST 2013)*, vol. 30, p. 31, 2013.

[41] T. Castiglione, W. He, F. Stern, and S. Bova, "Urans simulations of catamaran interference in shallow water," *Journal of Marine Science and Technology*, vol. 19, no. 1, pp. 33–51, 2014.

[42] H. K. Versteeg and W. Malalasekera, *An introduction to computational fluid dynamics: the finite volume method*. Pearson education, 2007.

[43] J. H. Ferziger, M. Perić, and R. L. Street, *Computational methods for fluid dynamics*, vol. 3. Springer, 2002.

[44] M. Darwish and F. Moukalled, *The Finite Volume Method in Computational Fluid Dynamics: An Advanced Introduction with OpenFOAM® and Matlab®*. Springer, 2021.

[45] J. A. Fay, "Introduction to fluid mechanics, book," 1994.

[46] O. Reynolds, *Papers on Mechanical and Physical Subjects: 1881-1900*, vol. 2. The University Press, 1901.

[47] F. H. Harlow and J. E. Welch, "Numerical calculation of time-dependent viscous incompressible flow of fluid with free surface," *The physics of fluids*, vol. 8, no. 12, pp. 2182–2189, 1965.

[48] C. W. Hirt and B. D. Nichols, "Volume of fluid (vof) method for the dynamics of free boundaries," *Journal of computational physics*, vol. 39, no. 1, pp. 201–225, 1981.

[49] G. Tryggvason, R. Scardovelli, and S. Zaleski, *Direct numerical simulations of gas–liquid multiphase flows*. Cambridge university press, 2011.

[50] J. U. Brackbill, D. B. Kothe, and C. Zemach, "A continuum method for modeling surface tension," *Journal of computational physics*, vol. 100, no. 2, pp. 335–354, 1992.

[51] B. Leonard, "Bounded higher-order upwind multidimensional finite-volume convection-diffusion algorithms," *Advances in numerical heat transfer*, vol. 1, pp. 1–57, 1997.

[52] B. Lafaurie, C. Nardone, R. Scardovelli, S. Zaleski, and G. Zanetti, "Modelling merging and fragmentation in multiphase flows with surfer," *Journal of computational physics*, vol. 113, no. 1, pp. 134–147, 1994.

[53] O. Ubbink, "Numerical prediction of two fluid systems with sharp interfaces," 1997.

[54] S. Muzaferija and M. Peri´ c, "Computation of free-surface flows using the finite-volume method and moving grids," *Numerical Heat Transfer*, vol. 32, no. 4, pp. 369–384, 1997.

[55] H. G. Weller, "A new approach to vof-based interface capturing methods for incompressible and compressible flow," *OpenCFD Ltd., Report TR/HGW*, vol. 4, p. 35, 2008.

[56] P. Higuera, J. L. Lara, and I. J. Losada, "Realistic wave generation and active wave absorption for navier–stokes models: Application to openfoam®," *Coastal Engineering*, vol. 71, pp. 102–118, 2013.

[57] S. Osher and J. A. Sethian, "Fronts propagating with curvature-dependent speed: Algorithms based on hamilton-jacobi formulations," *Journal of computational physics*, vol. 79, no. 1, pp. 12–49, 1988.

[58] H. Zhang, L. Zheng, V. Prasad, and T. Hou, "A curvilinear level set formulation for highly deformable free surface problems with application to solidification," *Numerical Heat Transfer, Part B*, vol. 34, no. 1, pp. 1–30, 1998.

[59] T. Hino, "Computation of viscous flows with free surface around an advancing ship," in *Proc. of the 2nd Osaka International Colloquium on Viscous Fluid Dynamics in Ship and Ocean Technology (Osaka)*, 1992.

[60] J. Farmer, L. Martinelli, and A. Jameson, "Fast multigrid method for solving incompressible hydrodynamic problems with free surfaces," *AIAA journal*, vol. 32, no. 6, pp. 1175–1182, 1994.

[61] J. Thé, G. Raithby, and G. Stubley, "Surface-adaptive finite-volume method for solving free surface flows," *Numerical Heat Transfer*, vol. 26, no. 4, pp. 367–380, 1994.

[62] G. Raithby, "Prediction of incompressible free surface flows with an element-based finite volume method," *Computat Fluid Dyn J*, vol. 4, pp. 353–371, 1995.

[63] G. Tryggvason and S. O. Unverdi, "Computations of three-dimensional rayleigh–taylor instability," *Physics of Fluids A: Fluid Dynamics*, vol. 2, no. 5, pp. 656–659, 1990.

[64] O. Reynolds, "Xxix. an experimental investigation of the circumstances which determine whether the motion of water shall be direct or sinuous, and of the law of resistance in parallel channels," *Philosophical Transactions of the Royal society of London*, no. 174, pp. 935–982, 1883.

[65] A. N. Kolmogorov, "The local structure of turbulence in incompressible viscous fluid for very large reynolds numbers," *Proceedings of the Royal Society of London. Series A: Mathematical and Physical Sciences*, vol. 434, no. 1890, pp. 9–13, 1991.

[66] A. N. Kolmogorov, "Dissipation of energy in isotropic turbulence," in *Dokl. Akad. Nauk SSSR*, vol. 32, pp. 325–327, 1941.

[67] V. C. Patel, W. Rodi, and G. Scheuerer, "Turbulence models for near-wall and low reynolds number flows-a review," *AIAA journal*, vol. 23, no. 9, pp. 1308–1319, 1985.

[68] G. Medic and P. A. Durbin, "Toward improved prediction of heat transfer on turbine blades," 2002.

[69] A. N. Kolmogorov, "Equations of turbulent motion in an incompressible fluid," in *Dokl. Akad. Nauk SSSR*, vol. 30, pp. 299–303, 1941.

[70] D. C. Wilcox, "Reassessment of the scale-determining equation for advanced turbulence models," *AIAA journal*, vol. 26, no. 11, pp. 1299–1310, 1988.

[71] D. C. Wilcox *et al.*, *Turbulence modeling for CFD*, vol. 2. DCW industries La Canada, CA, 1998.

[72] F. R. Menter, "Two-equation eddy-viscosity turbulence models for engineering applications," *AIAA journal*, vol. 32, no. 8, pp. 1598–1605, 1994.

[73] F. R. Menter, "Review of the shear-stress transport turbulence model experience from an industrial perspective," *International journal of computational fluid dynamics*, vol. 23, no. 4, pp. 305–316, 2009.

[74] J. Zha, "Numerical model of wave generation and absorption based on openfoam and its applications," *Shanghai Jiao tong University, Shanghai*, 2011.

[75] S. V. Patankar and D. B. Spalding, "A calculation procedure for heat, mass and momentum transfer in three-dimensional parabolic flows," in *Numerical prediction of flow, heat transfer, turbulence and combustion*, pp. 54–73, Elsevier, 1983.

[76] R. Issa, B. Ahmadi-Befrui, K. Beshay, and A. Gosman, "Solution of the implicitly discretised reacting flow equations by operator-splitting," *Journal of computational physics*, vol. 93, no. 2, pp. 388–410, 1991.

[77] J.-h. Wang, W.-w. Zhao, and D.-c. Wan, "Development of naoe-foam-sjtu solver based on openfoam for marine hydrodynamics," *Journal of Hydrodynamics*, vol. 31, no. 1, pp. 1–20, 2019.

[78] F. Moukalled, L. Mangani, M. Darwish, *et al.*, *The finite volume method in computational fluid dynamics*, vol. 113. Springer, 2016.

[79] R. G. Dean and R. A. Dalrymple, *Water wave mechanics for engineers and scientists*, vol. 2. world scientific publishing company, 1991.

[80] L. Skjelbreia and J. Hendrickson, "Fifth order gravity wave theory," *Coastal Engineering Proceedings*, no. 7, pp. 10–10, 1960.

[81] M. Banner and D. Peregrine, "Wave breaking in deep water," *Annual Review of Fluid Mechanics*, vol. 25, no. 1, pp. 373–397, 1993.

[82] B. Van Leer, "Towards the ultimate conservative difference scheme. v. a second-order sequel to godunov's method," *Journal of computational Physics*, vol. 32, no. 1, pp. 101–136, 1979.

[83] V. Vukčević, H. Jasak, and Š. Malenica, "Decomposition model for naval hydrodynamic applications, part i: Computational method," *Ocean Engineering*, vol. 121, pp. 37–46, 2016.

[84] F. Menter, "Zonal two equation kw turbulence models for aerodynamic flows," in *23rd fluid dynamics, plasmadynamics, and lasers conference*, p. 2906, 1993.

[85] I. Procedures, "Guidelines: practical guidelines for ship cfd applications," *ITTC Rep*, vol. 7, pp. 2–18, 2014.

[86] G. Filip, W. Xu, and K. Maki, "Urans predictions of resistance and motions of the kcs in head waves," tech. rep., 2017.

[87] K. Sugalski, "Influence of the symmetry plane boundary condition on the planing multihull calm water resistance test. cfd to towing tank comparison," *New Trends in Production Engineering*, vol. 1, no. 1, pp. 385–391, 2018.

[88] I. B. Celik, U. Ghia, P. J. Roache, and C. J. Freitas, "Procedure for estimation and reporting of uncertainty due to discretization in cfd applications," *Journal of fluids Engineering-Transactions of the ASME*, vol. 130, no. 7, 2008.

[89] P. J. Roache, "Perspective: a method for uniform reporting of grid refinement studies," 1994.

[90] A. J. Sinisterra, T. Moscicki, and M. R. Dhanak, "Thrust response and polynomial drag characterization of a usv with electric motors," in *OCEANS 2021: San Diego–Porto*, pp. 1–10, IEEE, 2021.

[91] G. Benham, J.-P. Boucher, R. Labbé, M. Benzaquen, and C. Clanet, "Wave drag on asymmetric bodies," *Journal of Fluid Mechanics*, vol. 878, pp. 147–168, 2019.

[92] G. Benham, R. Bendimerad, M. Benzaquen, and C. Clanet, "Hysteretic wave drag in shallow water," *Physical Review Fluids*, vol. 5, no. 6, p. 064803, 2020.